University of South Florida
Scholar Commons

Graduate Theses and Dissertations
Graduate School

7-7-2008

Mechanical Properties of Particulate-Reinforced Boron Carbide Composites

Lorenzo W. Hankla
University of South Florida

Follow this and additional works at: https://scholarcommons.usf.edu/etd

Part of the American Studies Commons

Mechanical Properties of Particulate-Reinforced Boron Carbide Composites

by

Lorenzo W. Hankla

A thesis submitted in partial fulfillment
of the requirements for the degree of
Master of Science in Mechanical Engineering
Department of Mechanical Engineering
College of Engineering
University of South Florida

Major Professor: Ashok Kumar, Ph.D.
Nathan Crane, Ph.D.
Muhammad Rahman, Ph.D.
Makoto Hirai, Ph.D.
Ramachandran Radhakrishnan, Ph.D.

Date of Approval:
July 7, 2008

To Dad, Laura, Amanda, Beth, and, of course, my favorite Mom.

ACKNOWLEDGEMENTS

Earning a postgraduate is not an easy task and, as such, I would like to express my sincere gratitude to the large number of people who helped me along the way. First, I would like to extend my appreciation to my major professor, Dr. Ashok Kumar, for his aid and support throughout this investigation. I know few are given the chance to conduct research in an industrial environment and I am thankful for being given the chance to do just that. I would also like to thank my committee members Dr. Nathan Crane and Dr. Muhammad Rahman for taking the time to review this manuscript and provide me with their valuable feedback.

Special thanks goes out to Dr. Makoto Hirai for taking the time to sit on my committee and help me with all of the scanning electron microscope images seen in this manuscript.

I would also like to extend appreciation to everyone at Materials Modification Inc. in Fairfax, Virginia for the constant help and support provided to me throughout this research endeavor. Without the helpful guidance and support from Dr. Ramachandran Radhakrishnan, Mr. Jim Intrater, and Dr. T. S. Sudarshan, this research would have never been possible.

Finally, I would like to thank my family and close friends for their constant support, love, and encouragement throughout this research process: thank you all!

TABLE OF CONTENTS

LIST OF TABLES

LIST OF FIGURES

viii

Mechanical Properties of Particulate-Reinforced Boron Carbide Composites

Lorenzo W. Hankla

ABSTRACT

The mechanical properties of boron carbide (B_4C) with 10 and 20 vol% particulate inclusions of commercially available nano-sized alpha-phase silicon carbide (α-SiC) or micron-sized titanium diboride (TiB_2) were investigated so as to produce a fine-grained material with high hardness, toughness, and overall strength in order to increase the effectiveness of B_4C as a structural ceramic, whose use in the field has been limited because of the extreme brittle nature of the material.

Full density sintering of the ceramics ($\geq$99% theoretical) was completed using the novel Plasma Pressure Compaction ($P^2C^{®}$) technique, which limited grain growth due to a reduced processing temperature and a significantly reduced consolidation time.

The reinforced ceramic composites had particulate grains homogeneously distributed within the B_4C matrix. X-ray diffraction patterns confirmed that the constituents did not interdiffuse.

The four-point flexure strength for the monolithic B_4C ceramic was found to be significantly larger than any recorded value found in scientific literature, and was most likely attributed to the fine-grained microstructure resulting from the $P^2C^®$ processing.

The mechanical properties of the nano-sized α-SiC-B_4C ceramics showed a slight increase in the Chevron-notched four-point bend fracture toughness due to the crack deflection toughening mechanism. A slight decrease in the Vickers microhardness and the static elastic modulus values were also observed.

A significant increase in the fracture toughness as well as a slight increase in the microhardness and elastic modulus of the micron-sized TiB_2-B_4C materials was found. The toughening mechanism of this composite was attributed to the slight chemical bond between the B_4C matrix and the ultra-small, ultra-tough TiB_2 particulates, which forced a propagating crack to completely rip apart the TiB_2 reinforcing particles. This cleaving nature resulted in significant amounts of energy being absorbed by the micron-sized particulates.

It was concluded that the composite with 20 vol% TiB_2 allowed for the largest gain in toughness because it possessed the largest number of ultra small, ultra tough particulate-cracktip interactions.

CHAPTER 1: INTRODUCTION

Boron carbide (B_4C) is a nonoxide ceramic having a high melting point, outstanding hardness, relatively good mechanical properties, low specific weight, great resistance to chemical agents, and a low neutron absorption cross-section.[1] In fact, outside of diamond and cubic boron nitride, boron carbide is the third hardest known industrial material.[2] The use of B_4C in the structural ceramics field, however, has been severely limited because of the brittleness associated with the material.[3] With this in mind, the objective of this research was to develop a fine-grained, particulate-reinforced boron carbide-based advanced ceramic material having high hardness, high toughness, and high overall strength in hopes of increasing the effectiveness of B_4C as a structural ceramic.

The major industrial uses of boron carbide in the structural ceramic field are based on its extreme hardness and wear resistance characteristics, good mechanical strength at both low and high temperature, low specific gravity, thermal and chemical resistance, and nuclear properties.[3] One of the main uses of the material is as abrasive grit or powder in polishing, lapping, and grinding media, as well as cutting applications for hard materials such as cemented carbides, other technical ceramics, and cermets. Boron carbide is far less expensive than diamond when used as an abrasive.[3]

A second category of the industrial use of the ceramic is in wear-resistance components, such as sand-blasting nozzles that are characterized by minimum wear when subjected to harsh environments containing silicon carbide.[3] Boron carbide ceramic nozzles are also used for water-jet cutting, slurry pumping, and other grit blasting because of its excellent abrasion resistance.[2] Other wear applications include sintered B_4C wheel dressing sticks to produce new edges on cuttings disks, and mortars and pestles.[3]

The unique combination of low specific gravity, high elastic modulus, and high hardness in boron carbide has led to its development for use as ceramic armor for the protection against a variety of ballistic threats in helicopters or vests for personnel.[3]

Boron carbide is also an attractive material in the nuclear industry in such applications as control rod pellets, shut down balls, and shielding for high-density storage of spent nuclear fuel.[3] This attractiveness is because B_4C provides a high concentration of boron atoms, which is the principle neutron absorber in nuclear reactors because of the absence of long half-life decay products resulting from the nuclear reactions as well as a lack of production of high-energy secondary radioactive products.[2] B_4C is used as opposed to elemental boron because pure boron is extremely brittle, more so than boron carbide, and is more difficult to produce in shapes such as control rods when compared to the refractory form of B_4C.[2]

The main fundamental drawback of the use of boron carbide as a structural ceramic in the aforementioned industrial settings is the inherent brittle fracture nature of the material.[2] Therefore, the strengthening of the material through particulate reinforcement is of great importance because the strength and toughness of boron carbide

2

can be improved without much significant losses to the properties that make the material attractive as a potential structural ceramic.

Nano-sized, commercially available, alpha-phase silicon carbide (α-SiC) was chosen as a particulate reinforcement because of its high hardness, relatively low density, modest fracture toughness, relatively high wear resistance, excellent oxidation resistance, high thermal conductivity, and good thermal shock resistance.[2] Such a combination of properties is determined by the highly covalent chemical bonding between the silicon and carbon atoms.[2] Silicon carbide also exhibits the unusual behavior of having an increased flexural strength as the environmental temperature increases, which is generally attributed to short-term crack healing as a result of an oxide layer that occurs on the surface of the SiC specimen.[4]

Likewise, micron-sized commercially available titanium diboride (TiB$_2$) was also chosen as a separate particulate-reinforcement phase because of the material's relatively high strength and durability as characterized by the relatively high values of its melting point, hardness, strength-to-density ratio, and wear resistance.[5] TiB$_2$ also has a relatively high elastic modulus value, which would carry over into the composite material and ultimately result in the material having a relatively high stiffness.[2]

These two types of particulate reinforcement materials were also chosen because both silicon carbide and titanium diboride display good thermodynamic stability from room temperature up to elevated temperatures, which helps deter diffusion during the consolidation process.[4,6]

The volume percentages of the particulates were kept to 10 and 20 percent because the addition of material in greater amounts could result in a greater risk of the

3

particulates diffusing with the B_4C matrix and forming additional phases. Likewise, both SiC and TiB_2 have slightly higher density values than B_4C and, therefore, as the volume percentage of the particulates increases, so too does the overall densities of the bulk ceramics.[2] This increased bulk density is a deterrent when used in weight-sensitive structural ceramic applications.

The novel Plasma Pressure Compaction ($P^2C^®$) technique was chosen as the sintering method for the ceramics in order to decrease the overall grain-size of each respective material by reducing the processing temperature and significantly lowering the consolidation time.[7] Both of these properties had a profound affect on the final microstructure of the ceramics, which in turn greatly affected the hardness, fracture toughness, strength, and stiffness of the materials as well their effectiveness as structural ceramics.[8]

Very little past research has been conducted in the use of these types of particulates in the small volumetric additions that were used for this research. Although TiB_2 has been investigated and proven to increase the mechanical properties of B_4C, it has never been examined using the $P^2C^®$ sintering technique. The addition of SiC has mainly been conducted at weight percentages that are less than about five.

The use of SiC as a reinforcing phase has been investigated by other researchers, but no research has been completed using the $P^2C^®$ technique. Riu, et al. investigated the oxidation behavior and the effect of oxidation on the room-temperature flexural strength of 30 wt% SiC additions on B_4C.[9] Much research has been conducted on the boron-carbon-silicon system, but it has generally been used for B_4C to be applied as a sintering aid to SiC and, as such, the amount of SiC in B_4C have been around 95 wt%. The

4

mechanical properties of such composites really cannot be compared to those investigated for this research.

The use of TiB_2 as a reinforcing phase has been investigated by other researchers, but as with the SiC additions, no research has been completed using the $P^2C^{®}$ technique. Yamada, et al. hot-pressed B_4C with additions of TiO_2 and C for 1 hr at 2000 °C and an applied load of 50 MPa under an argon atmosphere and formed a fully dense, in-situ B_4C + 20 mol% TiB_2 composite having a measured fracture toughness of 2.49 MPa · $m^{1/2}$, a flexure strength of 659 MPa, and a average grain-size of 1.1 μm.[10] The toughening mechanism associated with the campsite materials was attributed to microcracking. Tuffe, et al. hot-pressed B_4C and TiB_2 powders at 1800 °C for 1 hr under a 50 MPa applied pressure in a flowing argon atmosphere and were able to produce a B_4C + 50 wt% TiB_2 composite having a Vickers microhardness of 2658, a fracture toughness of 5.7 MPa · $m^{1/2}$, a flexure strength of 625 MPa, and an average grain-size of 4 μm.[11]

CHAPTER 2: LITERATURE REVIEW

An advanced ceramic is a highly engineered, rigorously controlled, high performance, predominately non-metallic, mostly crystalline and inorganic material having specific functional attributes.[12] These attributes are directly related to the processing conditions in which the ceramic material is subjected to during its manufacture as well as the ultimate final microstructure of the material.[13] This chapter represents a literature review of the concepts concerning ceramics in general, including an overview of ceramic materials, the process in which they are most often produced, the resulting structure and mechanical properties of these materials, as well as ways in which their strength can be increased.

2.1. CERAMICS

Ceramics are solids that are neither metallic nor organic, which means they are not carbon-chain based, and include materials such as clay products like porcelain, china, and brick, as well as natural stone and concrete.[14] Ceramics used in more demanding, high stress applications, called advanced or technical engineered ceramics, are often composed of relatively simple compounds of metals or the metalloids of silicon or boron with nonmetals, such as oxygen, carbon, or nitrogen.[15] Carbon in its graphite or diamond form is also considered to be a ceramic. Ceramics are predominantly crystalline and are

produced by binding the particles of a fine ceramic powder into a solid object without melting the material, which is otherwise known as powder processing.[14]

Glasses are similar to ceramics, but are amorphous and generally produced by means of melting silica (SiO_2), which is ordinary sand, with other metal oxides, such as calcium oxide (CaO), sodium oxide (Na_2O), boric oxide (B_2O_3), and lead oxide (PbO).[12]

Advanced ceramics have a number of important advantages when compared to their metallic counterparts, such as a relatively high resistance to corrosion and wear and a relatively high melting temperature.[12] Ceramics are also relatively stiff and light in weight. These advantageous properties exist because of the strong covalent or ionic-covalent chemical bonding of the compounds.[13] Ionic and covalent bonds are extremely strong and, as a result, ceramic materials are intrinsically stronger than metals. However, because of their more complex structure, the ions or atoms cannot be easily displaced because of an applied force.[12] Rather than bending to accommodate such forces, ceramics tend to fracture in a brittle manner.[12] This brittleness generally limits their use as a structural material. Slip of the crystalline planes in ceramics does not occur as readily as in their metallic counterparts because of the strength and directional nature of the covalent bonding and the relatively complex crystal structures.[12] This principle results in an inherent brittle nature of ceramic materials and is further enhanced by the fact that grain boundaries in these crystalline compounds are relatively weaker than in metals. These weak grain boundaries are caused by disrupted chemical bonds where the lattice planes are discontinuous at the grain boundaries and from the existence of regions where ions of the same charge are in proximity.[16] In addition, there is often an

7

appreciable degree of porosity and microscopic cracks inherent to ceramics, which also contribute to the brittleness.[16]

2.1.1. HISTORY

The term ceramic is often assumed to imply classical ceramics, which are the clay-based ceramics and whitewares that have helped man progress since antiquity.[13] In order to improve the mechanical properties of these early materials, the manufacturing technology and applications of present-day ceramics has steadily increased and has resulted in ceramics being categorized as either traditional or advanced. Traditional ceramic materials are derived from common, naturally occurring raw materials, such as clay minerals and quartz sand, and are almost as old as the human race. Naturally occurring abrasives were undoubtedly used to sharpen primitive wood and stone tools, and fragments of useful clay vessels have been found dating from almost 10,000 years ago.[14] Early man also learned to make use of natural occurring ceramics, such as volcanic glass and rocks, as tools and weapons, which is a period in time known as the Stone Age.[14] However, the inherent brittleness of the materials did not allow ceramics to obtain widespread use because their low toughness permitted cracks to easily propagate all the way through the material and result in catastrophic failure.

Not long after the first crude clay vessels were made, man learned how to make ceramics stronger, harder, and less permeable to fluids by placing the materials in an elevated temperature furnace for a certain period of time.[13] Structural clay products, including brick and tile, followed these advances. Steps towards advanced ceramics were taken about 10,000 years ago in the Middle East, when sun-dried clay bricks were

8

reinforced with straw in order to increase their toughness. This material was one of the first composites ever made and the material is known as adobe.[17] Even though the strength of this straw-based composite material was much greater than that of either one of the monolithic components, the extreme inherent brittleness of the composite material again caused for its severely limited application.

Through the use of toughening mechanisms, such as the ones used in the adobe bricks, a new generation of ceramic materials began to be introduced. These tougher, less brittle materials allowed for ceramics to be used in more demanding applications where their advantageous properties could be better utilized, such as the materials high hardness, relatively good chemical inertness, relatively low density, and relatively good strength at elevated temperatures.[16] Ceramics that are used in these types of applications are advanced, or technical, engineered ceramics, and their enhancement is upon what the current research is based.

The definition of advanced ceramics has been vague for many years but several classifications have been made based on their chemical nature, such as if they are oxide or nonoxide materials, and functionality.[15] In terms of functionality, advanced ceramics are broadly classified as, electrical, optical, chemical, and structural. Because of B_4C's hardness, low specific gravity, and covalent bonding, the ceramic material is very desirable in the structural sect of advanced engineered materials and ceramics, in such applications involving neutron absorption, wear resistance, and impact resistance.[3]

2.1.2. STRUCTURAL CERAMICS

Structural ceramics are materials that demonstrate enhanced mechanical properties under demanding conditions.[18] Because these types of materials are often subjected to mechanical loading and, thus, serve as structural members, they are given the name structural ceramics. In some structural applications and circumstances, ceramics tend to be a more expensive replacement for other materials such as metals and polymers.[16] For especially erosive, corrosive, or high-temperature environments, however, structural ceramics are the material of choice. This is because of the strong chemical bonding in ceramics that makes them exceptionally robust in demanding situations. Most ceramics are compounds between metallic and nonmetallic elements for which the interatomic bonds are either totally ionic or predominantly ionic but have some covalent character.[12] Because of this bonding, some advanced ceramics display superior wear resistance, for example, which makes them ideal for tribological, or wear, applications such as mineral processing equipment, cutting tools, and grinding media.[19] Likewise, structural ceramics also resist cavitation and abrasive wear, which is ideal for high-velocity fluid nozzles used for cutting and rocket engines.[12] These materials are also relatively chemically inert, which is crucial in the bioceramics field of prosthetic hip joints, knees, and teeth.[16] High chemical bond strengths also make ceramics thermochemically inert, which is a property that shows great promise in the areas of application in engines for automobiles, aerospace vehicles, and power generators.[16] Likewise, the hardness of ceramic materials and the resistance to deformation remains high, even at elevated temperatures where metals would soften or melt, which is helpful in the automotive and aeronautical brake industry.[13]

10

2.2. POWDER PROCESSING

Powder processing is a process in which fine ceramic powders are compacted into complex shapes.[14] The powder processing method is attractive for the manufacturing of advanced ceramics because it permits the development of intricately shaped ceramic parts with extremely fine grain-size. It is not unusual for the grain-size of the final ceramic specimen to approach that of the original starting powder.[12] Therefore, the powder processing method permits the development of microstructures that cannot be achieved with any other processing technique.

The process consists of several steps, including the synthesis of ceramic powders, blending of multiple constituents, forming of the powders, sintering of the compact, and finishing of the fully dense specimen, all of which will be discussed in further detail in the following sections.

2.2.1. POWDER SYNTHESIS

Ceramic powders can be produced in a variety of techniques. In general, the processing methods can be divided into mechanical and chemical processes.[14] Mechanical methods are generally used to prepare powders of traditional ceramics from naturally occurring raw materials. Powders prepared by mechanical methods are a fairly old area of ceramic processing and, therefore, new developments are rather small.[14]

Chemical methods are generally used to prepare powders of advanced ceramics from synthetic materials or from naturally occurring raw materials that have undergone a considerable degree of chemical refinement.[12] Some of the methods categorized as chemical involve a mechanical milling step as part of the process and is usually necessary

11

for the breakdown of agglomerates and for the production of the desired physical characteristics of the powder, such as average particle size and particle size distribution.

2.2.1.1. Boron Carbide

Boron carbide is generally manufactured by combining boric acid (H_3BO_3) and some form of carbon, be it either petroleum coke or pure graphite.[3] B_4C is formed through the thermal conversion of boric acid to boric oxide (B_2O_3). The reaction is strongly endothermic and boron-to-carbon ratios of about 4.3:1 along with a few free percent graphite are obtained.[1,3] An electric arc furnace or a graphite-tube furnace can be used for the reaction. The central area of the electric arc furnace usually reaches a temperature range of about 1500 °C to 2500 °C (2732 °F to 4532 °F), while the tube furnace reaches 1700 °C to 1800 °C (3092 °F to 3272 °F).[3,20] A stoichiometric, fine-grained boron carbide powder is obtained with particle sizes ranging from about 0.5 μm to 5.0 μm (< 0.001 in), but the overall yield of powder is much lower for the tube furnace than the amount of material obtained when an arc furnace is used. Once the boron carbide is produced, the material is then crushed and milled to produce the particle size appropriate for the end user. Any contaminates introduced during milling are eliminated by acid leaching.[3]

Boron carbide is also produced directly by magnesiothermic reductions of boric oxide in the presence of magnesium and carbon at a temperature range of 1000 °C to 1800 °C (1832 °F to 3272 °F).[3] Magnesium oxide (MgO) and unreacted magnesium are removed from the boron carbide thru acid washing in sulfuric acid (H_2SO_4). This reaction is strongly exothermic and is carried out either directly by point ignition or in a

12

carbon tube furnace in a hydrogen atmosphere. Ultra-fine boron carbide particles on the order of 0.1 μm to 1.5 μm (< 0.001 in) are obtained because the magnesium oxide (MgO) acts as a particle growth inhibitor.[3]

2.2.1.2. Silicon Carbide

Because of the rarity of moissanite, the naturally occurring version of the material, SiC is almost entirely synthetically produced.[21] Although many reactions between silicon and carbon produce SiC, the vast majority of industrial SiC powders are manufactured using the Acheson method.[21] In this method, a form of silicon dioxide (SiO_2), usually sand, and carbon, usually petroleum coke, are placed around a core of graphite powder that connects two adjacent solid graphite electrodes housed in an electric furnace. The assembly is heated to a maximum temperature of about 2500 °C (4532 °F) using an electric current. Generally, α-SiC crystal blocks are formed in this reaction, which are subsequently ground, refined, and classified. The type, structure, and quality of the crystals are dependent on the distance from the center of the furnace. The SiC produced using this method is mostly used as abrasives, refractories, and as additives for iron.[21]

A similar method to the aforementioned one can be used to produce essentially pure β-SiC, except the reaction takes place at a lower temperature, ranging from about 1500 °C to 1800 °C (2732 °F to 3272 °F), and lasts a shorter period of time.[21]

The beta form of silicon carbide may also be produced using the vapor-phase method, in which a silicon source, usually silane (SiH_4) or tetrachlorosilane ($SiCl_4$), is reacted with a hydrocarbon, usually either methane (CH_4) or propane (C_3H_8).[22] β-SiC is

13

also produced by the thermal decomposition of methyltrichlorosilane (CH_3SiCl_3) or tetramethylsilane $Si(CH_3)_4$.[4] The size of the resulting SiC particles along with the chemical composition is controlled by varying the reaction temperature, the gas concentration, and the gas flow rate.

Silicon carbide is also created by the direct reaction of silicon and carbon.[22] The gas evaporation method is also used to create SiC powder. In this method, the raw material surface is heated and melted using an arc discharge in a mixed gas to form ultra-fine SiC particles.[21]

Silicon carbide also exists in a whisker form, in which near perfect single crystals are grown to be on the order of a few microns in diameter and tens to hundreds of microns in length.[23] The whiskers are produced in a number of ways, including sublimation of silicon carbide abrasive powders, by gas phase reaction of numerous gaseous silicon and carbon molecules, by the reaction of silicon monoxide and carbon monoxide vapors, and by the carbon reduction of silica and a number of silicates.[24] Dried rice hulls have been used as a precursor to SiC whiskers because they contain both carbon and silicon.[23]

2.2.1.3. Titanium Diboride

Titanium diboride is a material that does not occur in nature, but can be synthesized in a number of different ways. Most often than not, TiB_2 is produced by reacting titania (TiO_2) with carbon and a boron source that is usually either boron carbide (B_4C) or boric oxide (B_2O_3).[25] The use of boric oxide is much less expensive than boron

14

carbide, but the stoichiometric ratio of titanium to boron cannot be controlled as easily or as accurately.[25] Because of this fact, high purity TiB_2 powder is relatively expensive.[25]

Titanium diboride can also be produced by thin film deposition, such as the chemical vapor deposition (CVD) and the physical vapor deposition (PVD) methods. In CVD, films are deposited from gaseous mixtures of titanium tetrahalides ($TiCl_4$), boron halides (BCl_3), and pure hydrogen.[26] This method can be used to produce continuous filaments as well as coatings on other filaments. Physical deposition can be accomplished using the PVD and sputtering techniques from TiB_2 targets.[25]

2.2.2. POWDER BLENDING

Blending of powders is necessary to provide a uniform distribution of powder size and for mixing powders of two or more constituents.[12] Blending is usually done by some type of mechanical milling, and requires the breakage of agglomerates and the reduction of sizes of the individual crystals.

Milling, which is also referred to as comminution, is the process in which small particles are produced by reducing the size of large ones by mechanical forces, and may be used to reduce the average particle size, free impurities, reduce porosity, and modify particle size distribution.[13] Comminution may also be used to aid in mixing. Milling can be accomplished in either a wet or dry environment. Wet ball milling has an advantage over dry milling in that its energy utilization is somewhat higher and the ability to produce a higher fraction of finer particles is increased.[15] However, the use of wet milling requires that the powder be dried after milling, the contamination of the powder by the absorbed vehicle is increased, and the wear of the grinding media is increased.[12]

15

Common mill types for grinding of ceramics include attrition mills and ball-mills. Attrition milling stirs the milling media and the particles, generally at a frequency of 20 to 30 Hz. Attrition comes from friction or rubbing particles between two hard surfaces.[19]

A dry ball-mill, which was used for this research, is a hollow rotating cylinder that is partially filled with hard, wear-resistant balls or short cylinders. The cylinder itself can be made from plastic or porcelain or be a lined metal container. The effectiveness of ball milling is related to the size and angular velocity of the mill, the size of the milling media when compared to the size of the particles, the weight of the milling media compared to the weight of the substance to be milled, and the physical characteristics of the particles that are to be milled.[16]

The milling media reduces the granular particle sizes by impacting and shearing the particles.[14] Shear is produced when a particle is seized by two surfaces moving at different velocities. The milling process can affect the final microstructure obtained from milled ceramic powders because impurities can be acquired and inclusions or strain can be introduced into the particles.[14]

2.2.3. FORMING

The consolidation of ceramic powders is commonly referred to as forming. A formed ceramic body is generally known as a green body or powder compact, which is an unsintered, low density powder compact having very little mechanical strength.[14] The main forming methods include plastic forming, slip or tape casting, and mechanical compaction.[14] Plastic forming is the mixing of powders with water or some other organic polymer to produce a plastic mass that is shaped by pressing or deformation. Slip casting

16

and tape casting involve the casting of powders from a concentrated slurry into thin sheets. Mechanical compaction involves the pressing of dry or semi-dry powders into dies. The mechanical compaction method was the only technique used for this research, and hence will be the only method that is further expanded upon.

In mechanical compaction, ceramic powders are poured into a die and loaded until a given pressure is achieved using hydraulic or mechanically activated presses. The mass density of the compact within the die increases and good particle-to-particle contact is achieved in this step.[13] In general, the applied pressure is not transmitted uniformly because of friction between the particles and the die walls as well as between the particles themselves.[17] The stress variations correspond to density variations in the green body, which limit the degree of packing uniformity that can be achieved. The maximum pressure occurs near upper outer corners of the compact and diminishes toward the central axis. Pressing pressure decreases with increasing axial distance from the punch, as seen in Figure 2-1.[18] Non-uniform compaction of green bodies can leave large pores that are not entirely eliminated by sintering and ultimately reduce the mechanical properties of the specimen.

$$p_1 > p_2 > p_3 > p_4$$

Beginning of granule rearrangement stage

End of granule rearrangement stage
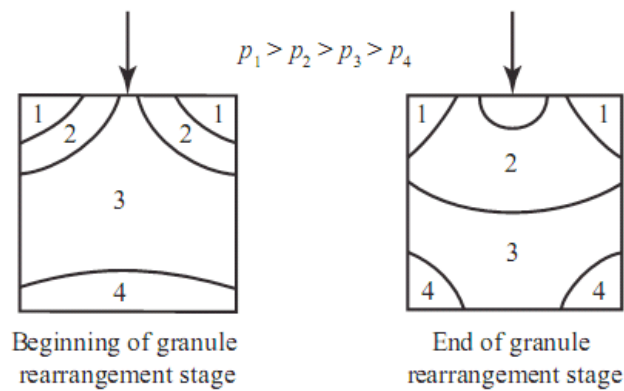
Figure 2-1: Pressure gradients of a powder compact subjected to pre- and post-uniaxial pressing.[18]

17

Green compacts may be subjected to additional compaction by the process known as cold isostatic pressing, in which the compact is placed in a mold made from rubber or some other type of elastomer. The assembly is then dropped into a chamber filled with fluid and pressurized to about 400 MPa to 1000 MPa (58 ksi to 145 ksi).[14]

Uniaxial dry pressing was the mechanical compaction method used for this research. This type of pressing is useful for pressing parts of relatively thin dimension in the pressing direction, which allows for the differential green densities throughout the part to be acceptably low.[14]

2.2.4. SINTERING

Sintering involves the heating of powder compacts to a certain temperature that causes the powder particles to fuse and form a solid object. The processing of the powder compact, as outlined in the above sections, plays a vital role in the development of the microstructure of the final fabricated ceramic.[14] The object formed will contain some degree of porosity, which is the volume percentage of voids. The driving force for sintering resides in the enormous surface energy stored in powders because of their high surface-area-to-volume ratio. This stored energy is so high that it could potentially lead to an explosion of some ceramic powders during storage.[16]

During sintering, the powder compacts are heated to a temperature between about 70% and 90% of their absolute melting points in order to get high diffusion rates along the grain, or powder, boundaries.[12] Since sintering is a diffusion-controlled process, the rate of densification, $d\rho/dt$, can be numerically calculated, as seen in Equation 2-1, where Q is the activation energy for grain boundary diffusion, R is the universal gas constant, T

18

is the absolute temperature, *d* is the average grain diameter, and *n* and *C* are material constants.[12]

$$\frac{d\rho}{dt} = \left(\frac{C}{d^n}\right)e^{-\frac{Q}{RT}} \qquad (2\text{-}1)$$

Sintering can be considered to proceed in initial, intermediate, and final stages.[14] During the initial stages of sintering, the surfaces of the individual particles in the powder compact are smoothed and grain boundaries are formed. Surface diffusion is a general transport mechanism that can produce surface smoothing, particle joining, and pore rounding, but it does not produce volume shrinkage. Neck growth proceeds rapidly when the interfacial tension of the boundary is somewhat less than the surface tension, but the particles remain mostly discrete. The interconnected pores become rounded and remain open, while the diffusion of active, segregated dopants occurs. The overall porosity of the powder compact is reduced by about 12%.[17]

During the intermediate stages of sintering, shrinkage of open pores that intersect grain boundaries occurs. The overall average porosity of the compact is decreased by a relatively significant amount and grain growth occurs slowly. During this stage, most of the densification of the compact occurs.[14] The structure recrystallizes and particles diffuse into each other. Recrystallization is a process by which deformed grains are replaced by a new set of undeformed grains that nucleate and grow until the original grains have been entirely consumed.[17]

19

During the third and final stage of sintering, isolated pores tend to become spherical and densification continues at a much slower rate.[17] The closed pores within the compact intersect grain boundaries. Pores are shrunk to a limited size or almost completely disappear. However, pores that are larger than grains shrink relatively slowly. As the final stage of sintering is prolonged, grains of much larger size appear rapidly while pores within larger grains shrink relatively slowly.[14] Figure 2-2 represents a schematic of the three aforementioned sintering stages, in which the powder particles are initially pressed together, represented in Figure 2-2-A, then grains begin to form and fill up the voids within the ceramic, Figure 2-2-B, and finally the reduction in area by the formation of a denser microstructure, Figure 2-2-C.[12]

| A. | B. | C. |
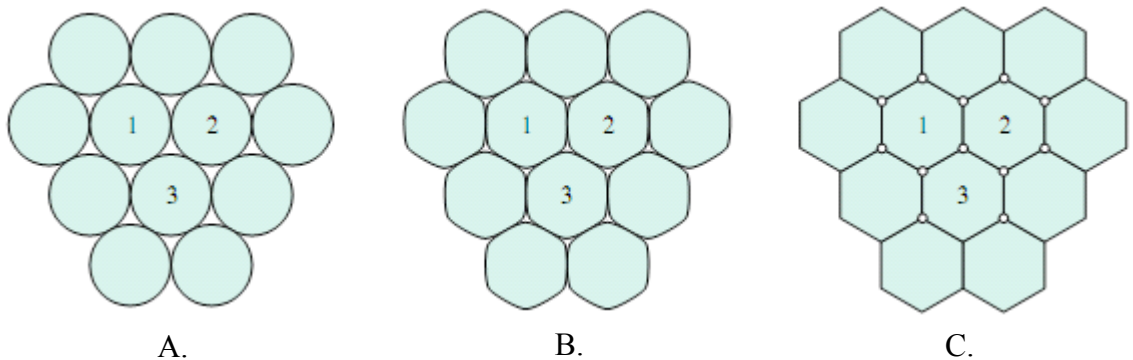
Figure 2-2: The sintering process: -A. Initial; -B. Intermediate; -C. Final.[12]

The theoretical density of a given powder compact, which is equivalent to the density associated with the perfect packing of individual atoms, may not be achieved during sintering because of residual closed pores.[13]

A wide variety of sintering techniques have been developed to obtain ceramics with the required density, microstructure, and composition for a given application.[16] The

methods involve the manipulation of some combination of the heating schedule, atmosphere, and applied pressure. In general, pressureless and pressure-assisted are the two main methods of sintering a ceramic powder compact.[14]

Pressureless sintering is where no external pressure is applied to the compact. This method is the preferred method of sintering because it is more economical and numerous compacts can be sintered at one time.[13] The use of pressureless sintering avoids density variations in the final component, which occurs with more traditional pressure-assisted methods. The powder compact can be created by slip casting into a plaster mold. The final green compact can then be machined, if necessary, into final shape before being sintered.[14]

Heating of the powder compact in pressureless sintering is commonly achieved with electrical resistance furnaces that allow for extremely high temperatures. The use of microwave energy for heating and sintering has attracted increased attention within the past few decades.[14] This method of heating is fundamentally different from that used in conventional furnaces in that the heat is generated internally by interaction of microwaves with the material. It is effective for rapidly heating ceramics, but the achievement of sufficiently uniform heating can be difficult.[14]

Pressure-assisted sintering is commonly used for the production of technical ceramics where high density must be guaranteed. The main types of pressure-assisted sintering are hot-pressing and hot-isostatic pressing.[14] Hot-pressing is where the pressure is applied uniaxially to the powder that is held within a die. Hot-isostatic-pressing is where the pressure is applied isostatically by means of a surrounding gas. The

21

application of pressure acts in conjunction with the elevated temperature to reduce the porosity and influence the density of ceramics.[16]

One of the major problems associated with pressureless and pressure-assisted sintering techniques is the amount of time required to achieve full densification of a given ceramic material. Such extended exposure to elevated temperatures leads to grain growth and results in deterioration in mechanical properties.[8] One of the easiest ways to increase the mechanical properties of a ceramic material is to control or minimize grain growth, which can be achieved by rapid consolidation. The Plasma Pressure Compaction sintering method, which was used for this research, allows for the consolidation time of ceramics to be severely decreased with the ability to have minimal or no grain growth.[27] This method will be further expanded upon in the following section.

2.2.4.1. Plasma Pressure Compaction

The Plasma Pressure Compaction technique ($P^2C^\circledR$) is a novel sintering technique developed by Material Modification Inc. (Fairfax, VA), which utilizes resistance heating and an externally applied pressure to sinter a given powder compact in minutes as opposed to the hours required with the use of other sintering techniques.[28] A direct current is applied to a graphite die that encompasses a powder compact and Joule heating causes the temperature of the compact to increase as the applied current is increased. The electrical current not only passes through the graphite die, but also through the powder compact itself.[28] This allows for the compact to be electrochemically active. An external uniaxial pressure is applied to the compact in order to accelerate the sintering process as well as to facilitate a sufficient current path through the powder compact. The entire

22

assembly is inside a rough vacuum chamber, which allows for the closing of pores on the ceramic samples and also minimizes oxidation levels that occur on both the sample and the graphite tooling. A schematic of the $P^2C^®$ apparatus may be seen below in Figure 2-3.[7]
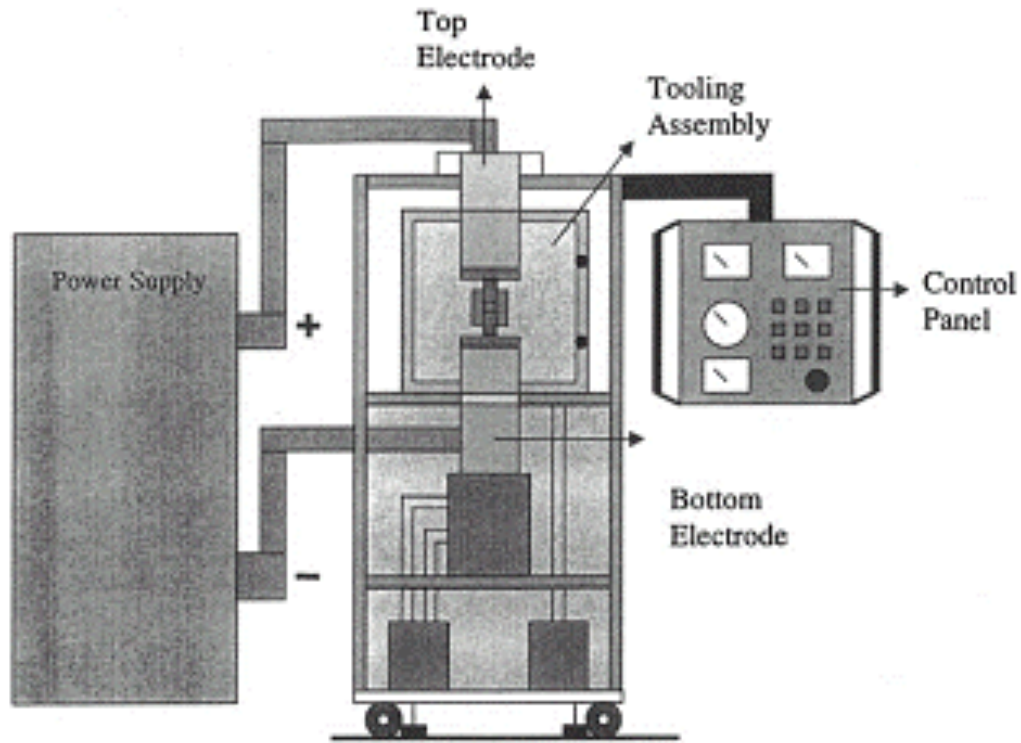
Figure 2-3: Plasma Pressure Compaction ($P^2C^®$) apparatus.[7]

When a pulsed DC electrical current is applied to the die setup, the current does not flow freely through the entire powder compact because an effective current path has not yet been established.[27] This lack of a current path is because of the voids within the powder compact as well as the inherent nature of the type of current being applied. Likewise, the oxide layer located on the surface of a powder particle acts as an insulator at the particle contact and causes a charge buildup at the interparticle gaps between the

23

powder particles.[28] This charge buildup then causes one particle to be charged negatively with respect to the other particles that are in contact with it. As the charge builds up, the voltage difference becomes sufficiently large to generate sparks that trigger an ionization process.[28] The resultant interparticle plasma serves to activate the surface of the powder particles by removing the oxide layer and other contaminants. At this stage, the powder compact is heated to higher temperatures so that any adsorbed gas and moisture is released.[27]

After a certain time at a given pulsed DC current, a constant DC current is applied in order to achieve the final sintering temperature. Direct application of the current and the external uniaxial pressure serve to accelerate densification of the material by inducing resistance heating and causing plastic deformation at the interparticle contact surfaces.[28] The amount of direct current and applied pressure to the die-powder compact setup is determined by various factors, such as the conductivity of the powder, the average particle size of the powder, and the dimensions of the graphite die being used.[27]

2.2.5. FINISHING

The finishing operation of ceramic parts is intended to give them special surface characteristics or to provide higher strength and higher dimensional accuracy, which is sometimes accomplished by additional pressing of the sintered part if it contains a fair amount of porosity. Generally, most dense ceramics are shaped in hard machining processes by the mechanism of chipping using tooling containing wear-resistant diamond particles. Lapping is used to remove near-surface damaged material and to improve surface smoothness.[14]

24

2.3. STRUCTURE OF CERAMICS

Ceramics by definition are composed of at least two elements, and as a result their structures are, in general, more complicated than those of metals.[12] The structure of ceramics can generally be classified as crystalline or noncrystalline, which is otherwise known as amorphous. A crystalline material is one in which the atoms are situated in a repeating or periodic array over large atomic distances.[12] In amorphous materials, however, this long-range order is absent. Some of the properties of crystalline solids depend on the crystal structure of the material, which is the manner in which atoms, ions, or molecules are spatially arranged.[13] Only crystalline solids were used for this research, and will thus be expanded upon further. The following sections discuss the chemical bonding of ceramics, the crystalline structure of ceramics, and an overview of the microstructure that is obtained from a fully sintered ceramic material.

2.3.1. CHEMICAL BONDING

The strong primary bonds that hold the atoms of a given ceramic together are the basis for many of the properties that are inherent to the material.[12] However, weaker secondary bonds, such as Van der Waal forces, also occur and have a major affect on the properties of some ceramic materials.[12] The primary chemical bonds found in ceramics are either totally ionic or a mixture of ionic and covalent.[17] Ionic bonding involves a transfer of bonding electrons from electropositive atoms, or cations, to electronegative atoms, or anions. Likewise, covalent bonding involves orbital sharing of electrons between the constituent atoms or ions. The larger the electronegativity differences between an anion and cation, the more nearly ionic the bonding. This can also be viewed

25

as the greater the difference in potential to accept or donate electrons, the more likely electrons are transferred and form positively charged cations and negatively charged anions. Conversely, small differences in electronegativity lead to a sharing of electrons, which is found in covalent bonding. Covalent bonds are highly directional in nature and often dictate the types of possible crystal structures.[12] Ionic bonds, on the other hand, are entirely nondirectional, which allows for hard-sphere packing arrangements of the ions into a variety of crystal structures. Because the atoms within ceramics are bonded in a much stronger fashion than that of metals, there are fewer ways for atoms to move, or slip, in relation to one another. Therefore, the ductility of ceramic materials is very low and failure is accomplished in a brittle manner.[13]

2.3.2. CRYSTALLINE STRUCTURE

The crystal structure of a material is described in terms of its unit cell, which is composed of one or more motifs, or spatial arrangements of atoms.[12] When a given unit cell is positioned in three-dimensional space, the bulk arrangement of atoms of the crystal is described by its lattice parameters, which are the length of the cell edges and the angles between them. The atoms contained within the call are described by the set of atomic position coordinates that are measured from a lattice point. The symmetrical properties of a given cell are determined by its space group. The Bravais lattice is a three-dimensional configuration of points that is used to describe the orderly arrangement of atoms within a given crystal. Each point represents one or more atoms in the actual crystal, and a crystal is formed if lines connect the points. There are only seven possible crystal systems that atoms can pack together to produce an infinite 3D space lattice in

26

such a way that each lattice point has an identical environment to that around every other lattice point.[12]

The crystalline structure of a ceramic material is generally defined by the relative sizes of the cations and anions as well as the magnitude of the electrical charge on each ion.[12] The radii of the atomic species within a ceramic material determines its structure because the cations and anions will tend to maximize and minimize their respective repulsions in order to achieve a state of lowest energy. Attractions are maximized when each cation surrounds itself with as many anions as possible without having any of the cations touch each other, which is also valid for the anions. Since cations are usually smaller than anions and occupy interstices, or spaces within the crystal lattice between the anions, the maximum number of anions that can be packed around the cation usually determines the crystal structure. Geometrically, this can be expressed in terms of the ratios of the radii of the cation and anion. As the size of the cation increases, the number of anions that can be accommodated around a given cation increases.[13]

The stoichiometric ratio of a given ceramic material likewise determines the structure of a ceramic because of the fact that a given crystal tends to be electrically neutral, which means that the sum of the positive charges are balanced and negated by an equal number of negative charges. This is a fact that is reflected in the chemical formula for a given ceramic, in which the number of positively-charged cations must be balanced by a strict number of negatively-charged anions. Therefore, the requirement of a crystalline structure to follow the law of electronegativity places a severe limitation on the type of structures the ions can assume because anions pack around cations, and

27

cations around anions, in order to eliminate a local charge imbalance, which is a phenomenon referred to as coordination.[16]

With these aforementioned facts regarding crystalline structures in mind, the rhombohedral and hexagonal crystal systems are just two of the possible lattice point groups that ceramics can form. Boron carbide is an example of the rhombohedral while certain polytypes of silicon carbide and titanium diboride are examples of hexagonal.[1,4,5]

The rhombohedral, or trigonal, crystal system is named after a two-dimensional rhombus and is described by three equal length vectors that are not mutually orthogonal. The rhombohedral system can be thought of as a cubic system that is stretched diagonally along a body, where the lengths of the crystal are equivalent but the resulting internal angles are not equal to 90°, as seen in Figure 2-4.[12] Only one Bravais lattice exists for the rhombohedral crystal system.
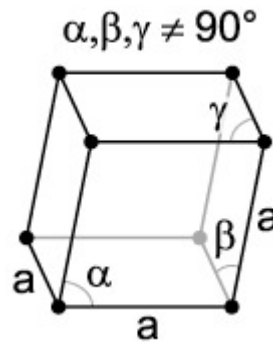
Figure 2-4: Wire model for a rhombohedral unit cell.[12]

The hexagonal crystal system has the same symmetry as a right prism with a hexagonal base, as seen in Figure 2-5.[12] Only a single Bravais Lattice and seven crystal classes exist for this system. Hexagonal structures have an atomic packing factor of 0.74

28

and a coordination number of 12.[13] The atomic packing factor is the volume fraction of atoms in a single crystalline structure, while the coordination number is the number of atoms neighboring the central atom of a single crystal. The structure also has very high planer and linear density values, which represent the number of atoms per unit area on a plane of interest and the number of equivalent lattice points per unit length along a direction, respectively.
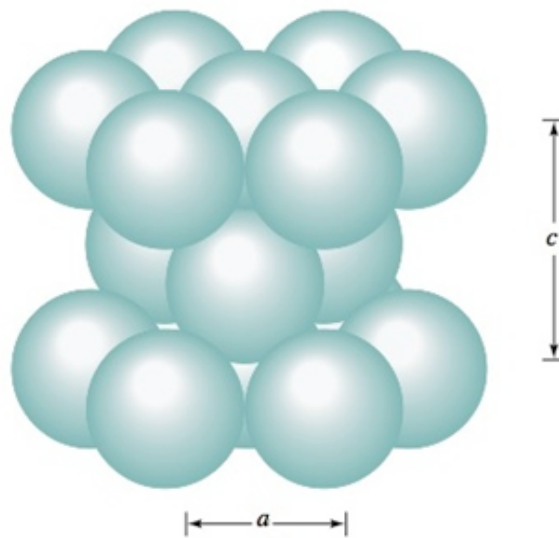
Figure 2-5: Full solid sphere model for a simple hexagonal structure.[12]

2.3.2.1. Boron Carbide

The fundamental crystalline structure of boron carbide is a rhombohedral unit cell having twelve icosahedral structures at the cell's eight corners.[1,3] The centers of these icosahedra are located on each of the corners of the rhombohedra cell and are joined by three-atom chains that extend through the center of the rhombohedra, as seen in Figure 2-6.[1] A rhombohedron is a geometrical pattern with axes of equal length and equal axial

29

angles, while an icosahedron is a polyhedron having twenty faces, twelve equivalent vertices, and various planes of symmetry, as seen in Figure 2-7.[2] The twelve atoms of the icosahedra and the three interconnecting atoms form a fifteen-atom cell, and the lattice belongs to the D_{3d}-R3m space group.[3]

Boron carbide is known to exist as a single phase with a fairly large variation in carbon concentrations, which is made possible by the substitution of boron and carbon atoms for one another within both the icosahedra and inter-icosahedral chains.[20] The number of carbon atoms that are able to be incorporated into the icosahedra is limited to a maximum number of two atoms because of bonding constraints.[3]
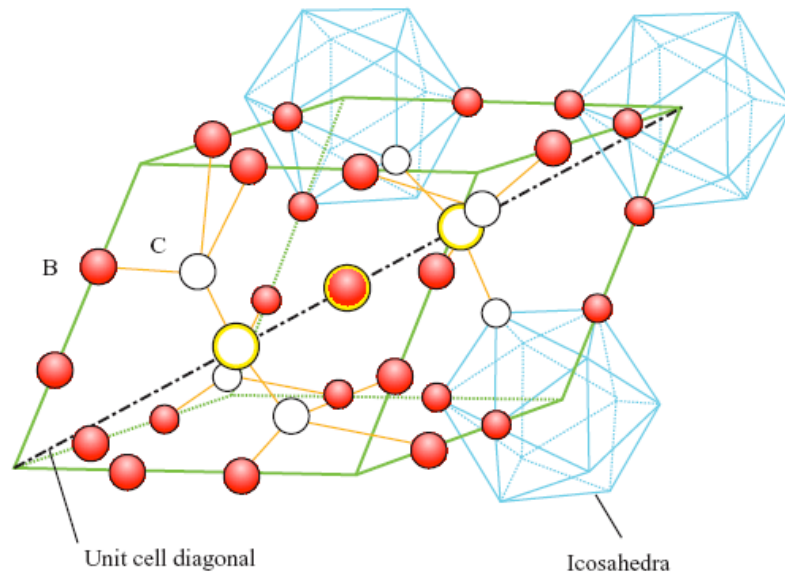
Figure 2-6: Schematic representation of the boron carbide crystalline structure.[1]
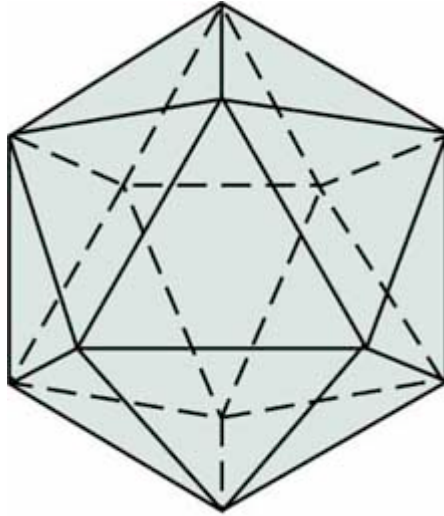
Figure 2-7: Wire model for an icosahedra structure.[2]

Because of the ability of carbon atoms to hybridize into the sp^3 orbital, a carbon atom can occupy both ends of the three-atom inter-icosahedra chain, while the center atom is boron, thus making a C-B-C chain.[2] However, singly ionized carbon atoms have occasionally been detected in the center position.[3] With decreasing carbon concentration, however, boron preferentially substitutes for carbon in the three-atom inter-icosahedra chains, and allows for a conversion from C-B-C chains to C-B-B chains. The most widely accepted structural model for boron carbide has $B_{11}C$ icosahedra with C-B-C inter-icosahedral chains.[29]

The boron icosahedron is deficient in electrons and requires the addition of two more to be present in order for the crystal to acquire a thermodynamically favorable closed-shell structure.[3] These additional electrons are provided by substitution of carbon atoms.[3]

31

The bonds between the boron and carbon atoms in B_4C are essentially covalent in nature.[1] However, because of the differences in electronegativity for boron and carbon, a partial ionic bond also occurs.[2]

The crystal lattice parameters of B_4C are dependent on the amount of carbon present within the material.[30] Because of the wide homogeneity range of boron carbide, the hexagonal lattice parameters, a_H and c_H (in Å), and the total volume of the rhombohedral cell, V_R, are found to vary slightly.[3] For the boron-rich phases, the values for the a_H and c_H parameters remain fairly constant up to an atomic carbon percentage of about 8.8, at which the a_H parameter and volume cell begin to decrease in a fairly linear manner. The c_H parameter, however, remains at a fairly constant value, as seen in Figure 2-8.[3]

For the carbon-rich phases, the values for the a_H and c_H parameters as well the volume of the rhombohedral cell all decrease in a linear manner up to an atomic carbon percentage of about 20.0. At this composition, however, these values then remain at a fairly constant value, as seen in Figure 2-9.[3] The ratio of c_H/a_H therefore varies as a function of carbon content.[3]

The theoretical density of boron carbide is dependent upon the amount of carbon present within the material. The density increases linearly with increasing atomic amount of carbon within the homogeneity range 8.8% to 20.0%, as seen numerically in Equation 2-2, where C is the atomic percentage of carbon present within the powder.[3]

$$\rho = 2.422_4 + 0.0048C \qquad \text{(2-2)}$$

32

The density measured for stoichiometric B_4C is 2.52 g/cm^3. This value, however, can vary slightly for various boron carbide powders because the carbon content in each is slightly different.[2]

The crystalline structure of boron carbide is valid within the aforementioned homogeneity range of 8.8 to 20.0 mol% C, as seen in the boron-carbon phase diagram in Figure 2-10.[31] These compositional percentages of carbon therefore correspond to stoichiometric value of $B_{10:4}C$ to B_4C, respectively.[31]
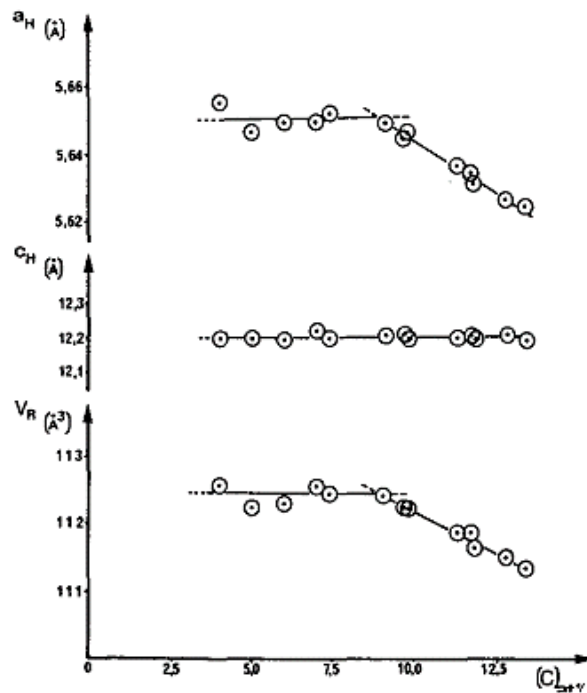
Figure 2-8: Hexagonal lattice parameters and cell volume of boron-rich B_4C.[3]
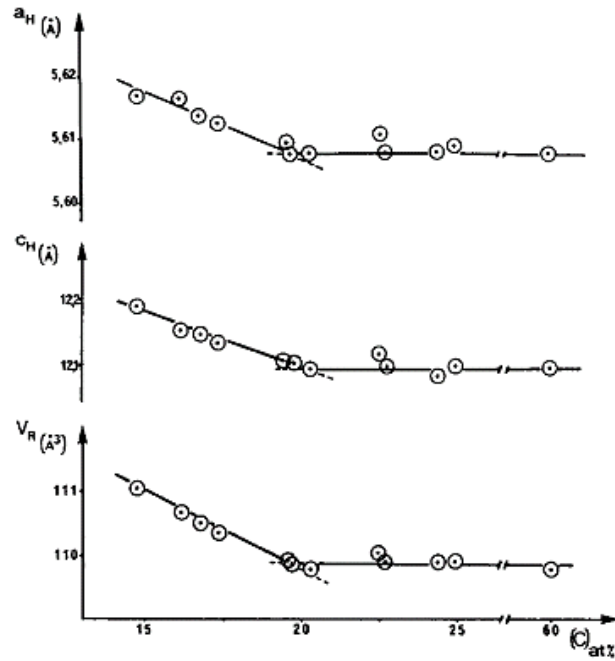
Figure 2-9: Hexagonal lattice parameters and cell volume of carbon-rich B$_4$C.[3]
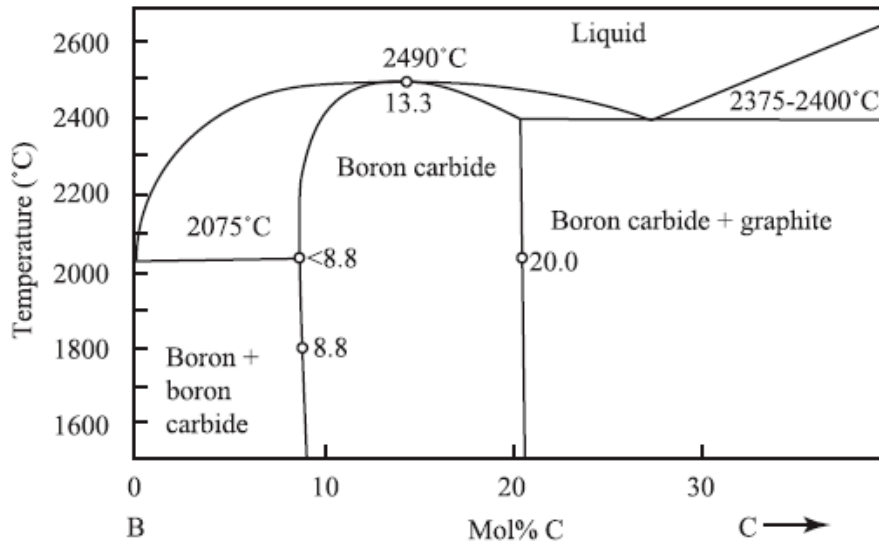
Figure 2-10: Boron-carbon phase diagram.[31]

www.manaraa.com

A carbon-saturated boron carbide and graphite mixture melts eutectically at 2375 °C to 2400 °C (4307 °F to 4352 °F) at a carbon concentration of about 29 mol%. Likewise, a boron-saturated boron carbide and β-rhombohedral boron melt peritectically at about 2075 °C (3767 °F). Between these two limits, a maximum melting temperature of about 2490 °C (4514 °F) for the solid solution is reached. Although this maximum melting temperature is placed at a composition of 13.3 mol% C in Figure 2-10, the actual composition of this point is not well known, and is sometimes placed at compositions as high as 18.5 mol% C in some phase diagrams.[3]

2.3.2.2. Silicon Carbide

Generally speaking, silicon carbide maintains a primary coordinated tetrahedral crystalline structure.[4] The crystalline structure of the material, however, varies because of the material's polytypism, which is the formation of unique one-dimensional ordering sequences that do not vary in stoichiometric ratio.[4] Around 200 polytypes have been found, and some have a stacking period of several hundred layers.[4] It has become standard practice to refer to the cubic polytype as β-SiC and to collectively refer all other non-cubic structures as α-SiC.[24]

The tetrahedral structure of all of the polytypes have a hexagonal frame with a carbon atom located both above the center of three triangularly positioned silicon atoms and underneath a silicon atom that belongs to the next layer, as seen in Figure 2-11-A.[32] The structure can be simplistically viewed as a planar sheet of silicon atoms linked with a planar sheet of carbon atoms.[33] The alternating layers of silicon and carbon form what is known as a bilayer. The bilayer plane is known as the basal plane while the direction

35

normal to this plane is known as the stacking direction. The distance from a plane of carbon atoms and silicon atoms is equivalent to a one-to-three ratio in relation to carbon-carbon interplanar distance.[32] The carbon atom is positioned at structure's center of mass for each tetrahedral.[32] Figure 2-11-B represents the projection of one hexagonal fundamental tetrahedral layer. As seen in this figure, the tetrahedral structures are arranged so that all atoms lie in parallel planes located on the nodes of regular hexagonal networks.[32]

Position or projection of
○ 1° Silicon layer
● 1° Carbon "
□ 2° Silicon "
■ 2° Carbon "
△ 3° Silicon "
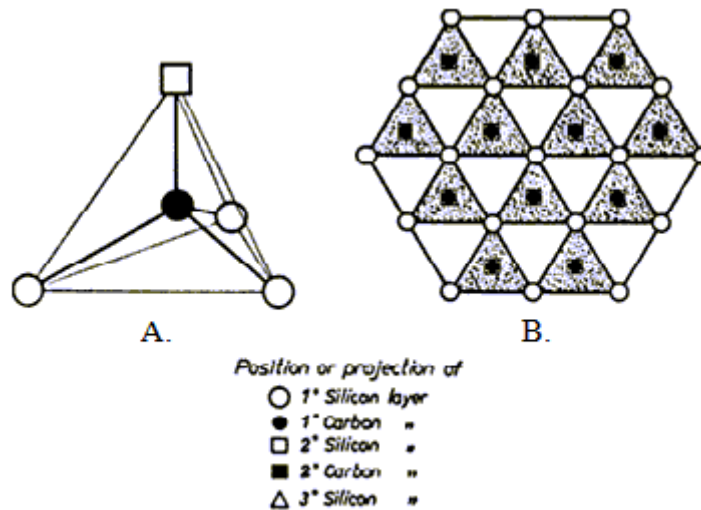
Figure 2-11: Position/projection of carbon and silicon atoms in SiC: -A. Basic tetragonal bonding of a first-layer carbon atom with three first-layer silicon atoms and one second-layer silicon atom; -B. Projection of one fundamental tetrahedral layer.[32]

Even tough a large number of SiC polytypes are known, only a handful are considered to be thermodynamically stable.[34] The cubic β-SiC polytype 3C, the rhombohedra polytype 15R, along with the hexagonal polytypes 2H, 4H, and 6H are the most frequently occurring polytypes and are considered to be the basic SiC structures.[33]

36

The nomenclature for these and all polytypes is based on their respective structure and stacking sequence. It is these stacking sequences of silicon-carbon double layers that are the main fundamental differences between each polytype.[34]

The 6H-SiC polytype is the most common polytype of SiC used in industry, and therefore it will be the only one discussed further. This form of silicon carbide belongs to the P6$_3$mc space group.[35] This polytype is hexagonal requiring six Si-C bilayers to define the unit cell repeat distance. The stacking sequence of the polytype can be seen in Figure 2-12, where the [1100] direction is the a-axis direction.[35] The silicon atoms labeled with a "h" or a "k" represent Si-C bilayers that reside in "quasi-hexagonal" or "quasi-cubic" environments with respect to their immediately neighboring above and below bilayers.[35]
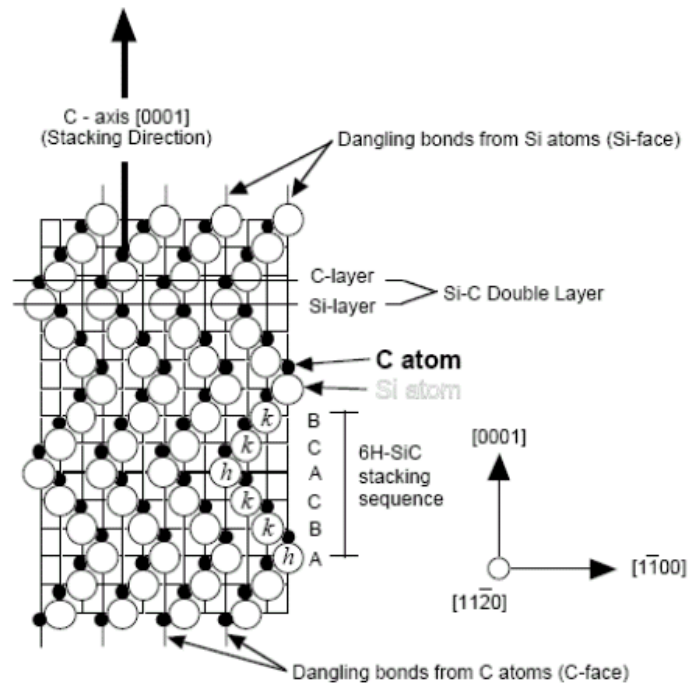
Figure 2-12: Cross-section view of the stacking sequence of 6H-SiC.[35]

Silicon carbide is almost entirely covalently bonded but also has an ionic bond contribution of about 12%, as estimated from Pauling's formula, resulting from the electronegativity difference between the silicon and carbon atoms.[33] Densification of SiC is very difficult because of these factors along with the material's extremely low selfdiffusion rate.[33]

The crystal lattice parameters of SiC are dependent upon the exposed environmental temperature. Within the temperature range of 0 °C to 1000 °C (32 °F to 1832 °F), the lattice parameters, *a* and *c* (in Å), may be numerically calculated, as seen in Equation 2-3 and Equation 2-4, respectively, where *T* represents the temperature in °C.[36] The ratio of *c*/*a* is therefore equivalent to 4.906 ± 0.001 at room temperature and 4.904 ± 0.001 at 1100 °C (2732 °F).[36]

$$a = 3.0813 + 1.0816 \cdot 10^{-5} T + 2.8833 \cdot 10^{-9} T^2 \qquad \textbf{(2-3)}$$

$$c = 15.116 + 5.104 \cdot 10^{-5} T + 1.153 \cdot 10^{-8} T^2 \qquad \textbf{(2-4)}$$

The theoretical density of silicon carbide, ρ_{TH}, can be calculated using the molecular mass of the material, *M* (40.097 g/mol), the number of formula units per unit cell, *n* (6), and the theoretical volume of the unit cell as it relates to the lattice parameters, *a* and *c*. This relationship may be seen in Equation 2-5, where N_A is Avogadro's number.[36]

38

$$\rho_{TH} = \frac{M \cdot n}{N_A \sqrt{\frac{3}{4}a^2 c}} \qquad \text{(2-5)}$$

Using Equation 2-5, the theoretical density of SiC at room temperature is 3.214 ± 0.001 g/cm^3, where the numerical error is derived from the error propagation resulting from the measured values of a and c.[36] This density value, however, is slightly higher than that of single phase polycrystalline SiC used in practice.[36]

Silicon carbide is the only solid compound in the carbon-silicon system and occurs in the narrow range of 30 wt% carbon, as seen in Figure 2-13.[37] The material does, however, form in two different aforementioned forms, α-SiC and β-SiC. The α to β transition temperature is not very well known.[38]
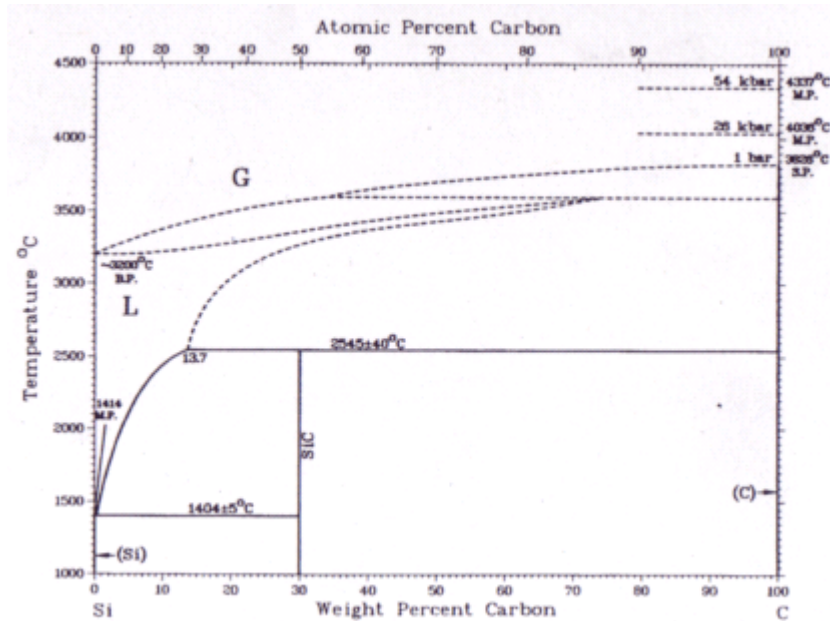
Figure 2-13: Carbon-silicon phase diagram.[37]

39

As seen in Figure 2-13, SiC melts incongruently to form a silicon-rich liquid phase of graphite above the peritectic temperature of 2545 ± 40 °C (4613 ± 104 °F).[37] The eutectic temperature between silicon and SiC is 1404 ± 5 °C (2559 ± 41 °F).[38] A gaseous phase is formed at temperatures above about 3200 °C (5792 °F). β-SiC is thought to be more stable than α-SiC at any temperature below the peritectic temperature.[38]

2.3.2.3. Titanium Diboride

Single crystal titanium diboride maintains a hexagonal crystalline structure. As seen in Figure 2-14, a titanium atom is located at the (0,0,0) coordinate while boron atoms fill the (1/3,2/3,1/2) and (2/3,1/3,1/2) locations.[39] TiB_2 belongs to the dihexagonal bipyramidal crystal class, which is also known as P6/mmm in international notation and D_{6H} in Schoenflies notation.[12]
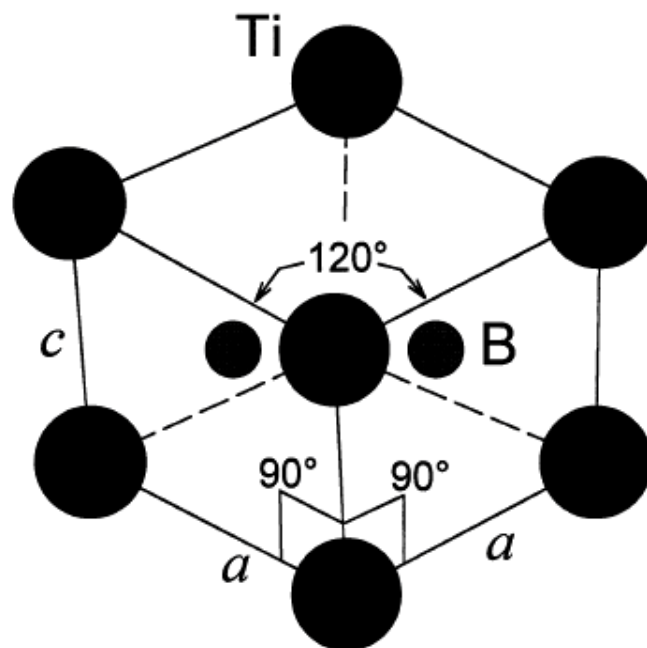
Figure 2-14: Single crystal TiB_2 hexagonal crystalline structure.[39]

40

The hexagonal lattices of TiB_2 are held together by both covalent and ionic bonds and the material has a low crystalline boundary diffusion coefficient.[40] Because of these characteristics, TiB_2 requires a very high sintering temperature, a very long sintering time, and a slow densification speed.[40]

The lattice parameters of TiB_2 vary slightly with temperature.[41] The parameters, a and c (in Å), can be numerically calculated, as seen in Equation 2-6 and Equation 2-7, respectively, where T represents the temperature (in K) within the range of about room temperature to 2000 °C (3632 °F).[41] The ratio of c/a is equivalent to 1.066 ± 0.001 at room temperature and 1.070 ± 0.001 at 1500 °C (2732 °F).[39]

$$a = 3.0236 + 1.73 \cdot 10^{-5} T + 3.76 \cdot 10^{-9} T^2 \qquad \text{(2-6)}$$

$$c = 3.2204 + 2.73 \cdot 10^{-5} T + 3.95 \cdot 10^{-9} T^2 \qquad \text{(2-7)}$$

The theoretical density of titanium diboride, ρ_{TH}, can be calculated using the theoretical volume of the hexagonal unit cell as it relates to the lattice parameters, a and c, along with the molar mass of the material (69.522 g/mol), and the number of formula units per unit cell, n (1), as seen in Equation 2-5. Using this equation, the theoretical density of TiB_2 at room temperature is 4.500 ± 0.0032 g/cm^3, where the numerical error is derived from the error propagating from the measured values of a and c.[39]

As stated earlier, numerous titanium-boron phases, such as TiB, Ti_2B, Ti_2B_5, and Ti_3B_4, have been identified along with TiB_2.[42,43] Some of these phases, however, only

41

exist in the presence of excess free carbon.[43] Three of these aforementioned compounds, Ti_3B_4, TiB, and TiB_2 are shown in the titanium-boron phase diagram seen in Figure 15.[43]
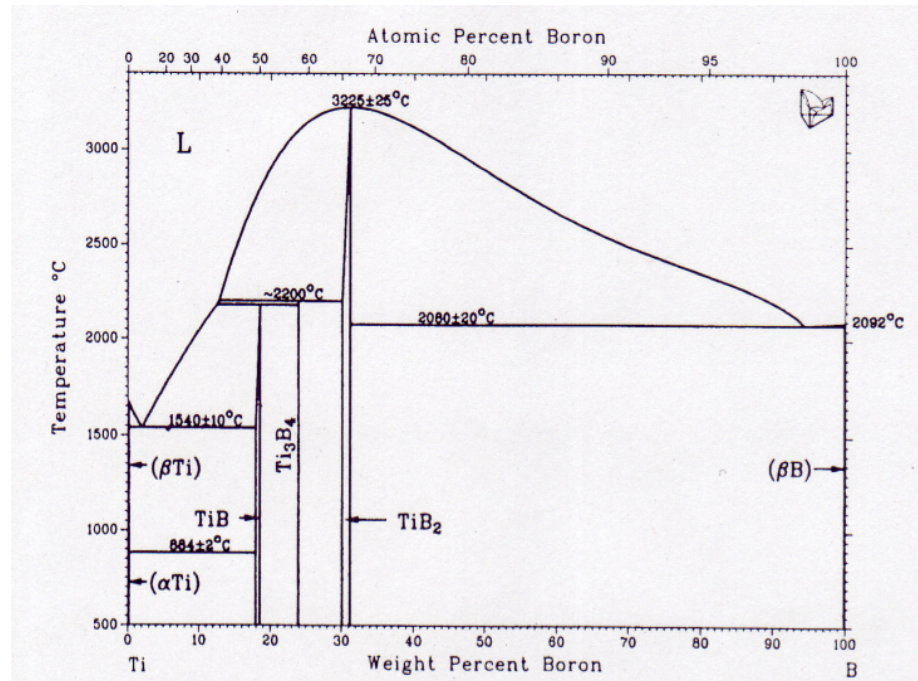
Figure 2-15: Boron-titanium phase diagram.[43]

As seen in Figure 2-15, the alpha- and beta-phase of titanium form with 0.0 to less than 0.05 wt% boron content at temperatures up to 884 ± 2 °C (1623 ± 36 °F) and 1540 ± 10 °C (2804 ± 50 °F), respectively. TiB forms with boron content from 18.0 to 18.4 wt% at a temperature up to almost 2200 °C (3992 °F), while Ti_3B_4 forms with boron content at 22.4 wt% and at a temperature around 2200 °C (3992 °F). Solid TiB_2 forms with boron content from 30.1 to 31.1 wt% at temperatures up to 3225 ± 25 °C (5837 ± 77 °F). At this temperature, a eutectic point exists with liquid TiB_2 and two other solid titanium-

42

boron phases. Above this temperature, however, and the material forms a complete liquid phase.

2.3.3. MICROSTRUCTURE

The microstructure of a ceramic is a result of all the steps the material has undergone before and during the sintering process.[14] In order to control the mechanical properties of a material, processing variables must be understood and all known potential impurities that could be introduced to the system need must be minimized. Each processing step, from the initial reactions incurred during powder manufacturing to the final sintering process, has the capability of introducing microstructural flaws that can limit the mechanical properties and reliability of a given ceramic material.[13]

In general, properties are controlled by the microstructure, but failure-dependent properties such as the mechanical strength and the fracture toughness of ceramics are regulated by flaws within the dense shapes produced after consolidation.[14] Grain boundary phases, porosity, grain-size, or chemical composition have all been shown to have an effect on the final mechanical properties of a ceramic.[44]

2.3.3.1. Grain-Size Reduction

A decrease in grain-size can be achieved by a reduction in densification time, temperature, and the minimization of porosity within a given ceramic material.[14] One way to decrease the sintering temperature is to sinter under pressure. This temperature reduction is because the driving force for sintering is increased due to the free energy of the matter in the highly stressed regions where particles make contact is locally increased.

43

It has been established that the energy available for densification is increased by more than 20% by the application of pressure during sintering. The simultaneous application of heat and pressure eliminates internal voids and microporosity through a combination of plastic deformation, creep, and diffusion bonding.[14]

Although it is possible to reduce the final sintering temperature by prolonging the sintering time at a lower temperature, the resultant risk of over-firing, excessive grain growth and possible higher production cost can prohibit this method.[14] Therefore, the most effective ways of decreasing the overall microstructure of a ceramic material is to decrease the consolidation time and temperature so as to decrease the grain growth, and to increase the consolidation pressure so as to increase the densification energy.[12]

2.4. MECHANICAL PROPERTIES OF CERAMICS

For structural advanced ceramics, adequate mechanical properties are of prime importance.[13] In advanced engineered ceramics, a strong emphasis on understanding the mechanical properties that affect their brittleness has been undertaken in recent years.[15] The following sections provide an overview of the most important of these mechanical properties, and includes information regarding contact-damage resistance, toughness, strength, and elasticity. Likewise, an overview is also given of the mechanical properties associated with boron carbide, silicon carbide, and titanium diboride.

2.4.1. MICROHARDNESS

The microhardness, or hardness based on a microscopic level, of a ceramic is a measure of the resistance of the material to the formation of a permanent surface

impression by an indenter.[45] This mechanical property can also be viewed as the resistance of a material to deformation, densification, and fracture, and is measured in terms of stress [Pa, psi].

2.4.1.1. Mechanical Theory

The hardness of a ceramic material is defined as the resistance of a material to indentation, which is the pressing of a hard ball or point against the material sample with a known force so that a depression is made. This depression, or indentation, results from plastic deformation beneath the indenter. Some specific measurement of the indentation, such as its size or depth, is then taken as a measure of hardness.[45]

The deformation process is inelastic and is inherently related to the resistance of a material to indentation.[45] The hardness of a material is an important mechanical property because it relates how much the material will inelasticly deform when a surface load is applied. An increased hardness value will result in a material being more resistant to indentation at a given load, which will mean the material will be able to plastically deform. Therefore, the greater the hardness of a ceramic, the greater resistance it has to deformation.[45]

Hardness measurement can be defined on a macro-, micro- or nano- scale according to the forces applied and the indentation sizes obtained. When materials have a fine microstructure, are multi-phase, non-homogeneous, or prone to cracking, such as ceramics, macrohardness measurements are highly variable and cannot fully identify individual surface features.[46] Therefore, microhardness measurements are used because

45

of the small area that comes into contact with the indenter. Microhardness is the hardness of a material as determined by pressing a Vickers or Knoop indenter into the surface of the material under 15 to 2000 g_f load (0.033 lb_f to 4.409 lb_f). Usually, the resulting indentations are so small that they must be measured using a microscope.[46]

The microhardness of ceramics is greatly influenced by several parameters associated with the testing procedure, such as the indentation load, dwell time, testing environment, and the specimen thickness, flatness, preparation.[47] In general, the microhardness of a ceramic material decreases with increasing indention size or indentation force. This trend is known as the indentation size effect. Microhardness approaches a plateau at a sufficiently large indentation force, which varies for different ceramic materials.[47]

In general, the accuracy of the test will depend on the smoothness of the surface.[47] As long as the specimen is over ten times as thick as the indentation depth, the test will not be affected. Likewise, if a test specimen is at least 0.50 mm (0.020 in) thick, the microhardness will not be affected by variations in the thickness.[47]

Cracking from the indentation tips can interfere with the determination of the location of the tip impression, which could lead to an inaccurate measurement of the indentation diagonal lengths.[47] Cracking or spalling around the Vickers impression may occur and alter the shape and clarity of the indentation, and the cracking may occur in minutes or hours after the impression is made.[12] Porosity, either on or just below the surface, may interfere with measuring microhardness, especially if the indentation falls directly onto a large pore or if the indentation tip falls in a pore. At higher magnifications

in the optical microscope, it may be difficult to obtain a sharp contrast between the indentation tip and the polished surface of some advanced ceramics.[47]

Because the porosity of a ceramic is highly correlated with its mechanical properties, reducing the number of defects in a ceramic is a common way of increasing its microhardness.[46] Methods of decreasing the total number of flaws and pores in ceramic materials, such as controlling the grain-size and morphology of the material through careful processing parameters, can be found in Section 2.3.3 of this manuscript.

The microhardness of a monolithic material has also been found to be increased with the addition of very hard dopants.[46] These additives, however, also tend to increase the final bulk density of the composite when compared to their monolithic counterpart.

The largest source of error in the measured microhardness values usually arises from the error and uncertainties associated with the measurement of the diagonal length, and include inaccurate calibration of the measuring device, inadequate resolving power of the objective, insufficient magnification, operator bias in sizing the indents, and poor image quality.[47] Microhardness uncertainties are usually greater for harder materials because the harder the material, the smaller the indent size is.[47]

The microhardness of a ceramic could also vary slightly if individual samples were machined from different bulk samples having slightly different properties, such as density, grain-size, or other flaws or cracks.

2.4.1.2. Testing Methods

The microhardness of a material can be found using either a Vickers or a Knoop indenter. The Vickers indenter creates a square impression from which two surface-

47

projected diagonal lengths are measured. Vickers microhardness is calculated from the ratio of the applied load to the area of contact of the four faces of the undeformed indenter. In contrast, Knoop indenters are also used to measure hardness, but Knoop hardness is calculated from the ratio of the applied load to the projected area on the specimen surface. Vickers indentation diagonal lengths are approximately 2.8 times shorter than the long diagonal of Knoop indentations, and the indentation depth is approximately 1.5 times deeper than Knoop indentations made at the same load.[45]

Vickers indentations are influenced less by specimen surface flatness, parallelism, and surface finish than Knoop indentations, but these parameters must be considered nonetheless. Likewise, Vickers indentations are much more likely to cause cracks in advanced ceramics than Knoop indentations. The cracks may influence the measured microhardness by fundamentally altering the deformation processes that contribute to the formation of an impression, and they may impair or preclude measurement of the diagonal lengths due to excessive damage at the indentation tips or sides. Vickers indentation tests were the only method used during this research, and will thusly be discussed in further detail below.[48]

The indenter used for a Vickers microhardness test is a diamond point in the shape of a pyramid with a square base. The angle between the faces of the pyramid, α, is 136° 00', as shown in .[45] This shape results in the depth of penetration, h, being one-seventh the length of the diagonal indentation size, d.[45]

48
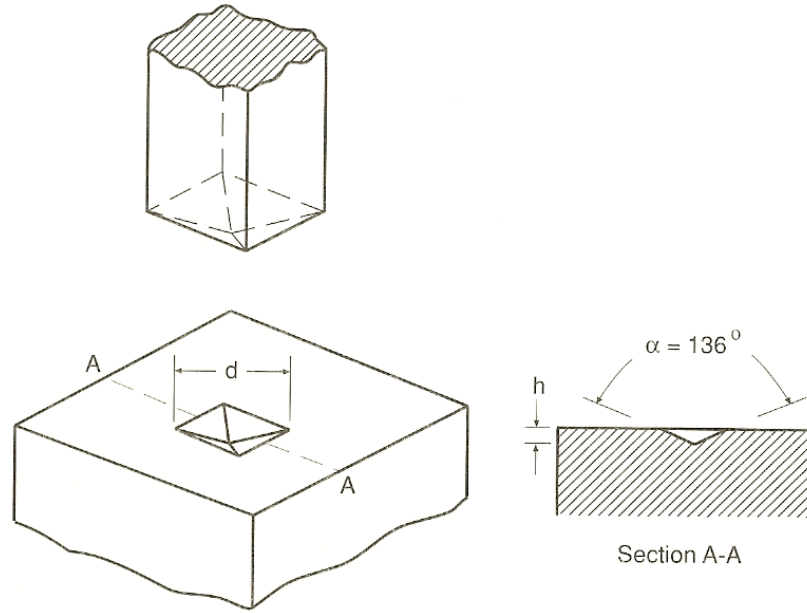
Figure 2-16: Vickers microhardness indentation technique.[45]

The Vickers microhardness number, HV, is calculated by dividing the applied load, *P* in kg$_f$, by the surface area of the pyramidal depression, as shown in Equation 2-8.[47]

$$HV = \frac{2P}{d^2}\sin\left(\frac{\alpha}{2}\right) = 1.8544\frac{P}{d^2} \qquad \textbf{(2-8)}$$

The exact same theory and procedure as outlined above can also be used for determining the Vickers microhardness of ceramics at elevated temperature and ambient environmental conditions.[47] The microhardness under these conditions may or may not necessarily be the inherent microhardness, because the mechanical property at elevated temperatures may be strongly dependent on testing rate, which is a result of creep, stress corrosion, or slow crack growth.[47] Therefore, extra precautions are required and faster

testing rates may be necessary if the inert hardness is intended to be found at elevated temperatures.[47]

2.4.2. FRACTURE TOUGHNESS

The fracture toughness of a material, K_{Ic}, is an indication of the amount of stress that is required to propagate a preexisting flaw or crack.[46] This property can also be viewed as the measure of a materials' resistance to crack propagation that will ultimately lead to failure. The fracture toughness of a material is also known simply as toughness and is expressed in units of stress-length$^{1/2}$ [MPa $\cdot$ m$^{1/2}$, psi $\cdot$ in$^{1/2}$].

2.4.2.1. Mechanical Theory

Because ceramics inherently possess multiple flaws, such as voids, inclusions, and/or small cracks, the fracture toughness of a material is important because it allows for an understanding of the extent to which these flaws govern the overall toughness of the material.[46] If the applied load to a given ceramic is too great, these inherently present flaws may suddenly grow and cause the material to fail in a brittle manner. Therefore, if the fracture toughness of a material is increased, then the material will be able to withstand a higher stress before a preexisting flaw is propagated and, thusly, the brittleness of the ceramic will be decreased.[45]

In terms of fracture mechanics, three different modes of fracture are present in materials, as seen in Figure 2-17.[49] However, Mode I, sometimes called the opening mode, is generally the most important when dealing with engineering materials because the crack faces move apart from one another, as opposed to the faces sliding relative to

50

one another in a direction normal to the leading crack edge (Mode II) or parallel to the leading edge (Mode III).[48] Because Mode I is caused by tension loading, whereas the other two modes are caused by shear, the majority of material cracking problems are concerned with this mode.[45]
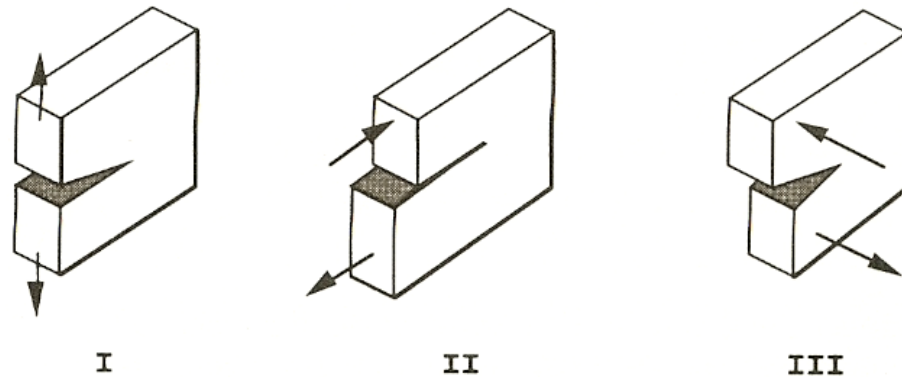
Figure 2-17: Basic modes of crack surface displacement.[49]

The fracture toughness of a material is directly derived from a quantity called the stress intensity factor, K.[50] This value characterizes the severity of a crack as a function of crack size, stress, and geometry. In general terms, the stress intensity factor characterizes the magnitude or intensity of the stresses in the vicinity of an ideally sharp cracktip in a linear-elastic and isotropic material. It can also be viewed as the magnitude of the ideal-crack-tip stress field for a particular mode in a homogeneous body.[49] The mathematical theory behind this value describes the stress field near the cracktip and, likewise, predicts that the stresses will rapidly increase near the tip of a crack, as seen empirically in Equation 2-9, where S is the remotely applied stress and a is the crack length.[50]

51

$$K = S\sqrt{\pi a} \qquad\qquad \textbf{(2-9)}$$

As with some physical properties, the stress intensity factor for a given material composition varies for specimens with the same dimensional proportions but varying absolute sizes.[46] This concept results because the stress states adjacent to the flaw changes with the changing fundamental specimen dimension based on the fracture mode, such as the thickness for Mode I, the length for Mode II, and the width for Mode III, until some critical dimension is reached. Once this dimension has been exceeded, the stress intensity factor becomes relatively constant and becomes an inherent property of the material, known as the fracture toughness, K_c. For Mode I fracture, the property is known as the plain-strain fracture toughness, K_{Ic}, and is the subject of the remainder of this section.[50]

The relationship between the stress intensity factor, K_I, and the fracture toughness, K_{Ic}, is similar to the relationship between stress and tensile stress in that the stress intensity represents the level of stress at the tip of a crack, while the fracture toughness represents the largest value of stress intensity that a given material can withstand without fracture.[45] Where as the stress is a measure of the intensity of the total internal forces acting within a body, while the tensile stress is measure of the intensity of the internal forces acting to expand the material in the tensile direction.[45]

The values obtained during the testing of the fracture toughness are greatly influenced by several parameters associated with the physical dimension of the bend bar specimen and the testing procedure.[50] When a crack or notch is not created within the

outlined specifications of ASTM standard C 1421-01b (2007), the resulting fracture toughness value could become invalid because machining damages or residual stresses could be incurred.

The fracture toughness for a ceramic material is dependent on the testing procedure, such as the testing rate, because of the effects of temperature and/or the environment.[50] Static forces applied for a long duration can cause crack extensions throughout the material at a stress intensity factor that is less than the measured values obtained through testing. The rate and severity of such a crack extension can be changed by the presence of an aggressive environment, and this time-dependent phenomenon is known as slow crack growth. This phenomenon can be meaningful even for the relatively short time intervals involved during testing of the ceramic and can lead to measured fracture toughness values that are less than the inherent resistance in the absence of environmental effects. The effect of slow crack growth may be significant even at ambient conditions and can often be minimized by selecting a different testing rate or by changing the environmental conditions.[50]

The stiffness of the four-point bend fixture can also affect the measured fracture toughness values.[50] Depending on the type of sharp-cracked bend bar specimen that is chosen, the fracture toughness is measured in either unstable or stable conditions. A stiff testing setup will promote stable crack extension, and thusly a stably-extending crack may give somewhat lower fracture toughness values.[50]

The fracture toughness of a ceramic is not a quantity that fluctuates greatly, but it will vary slightly from one specimen to another. As a result, experimental errors must be taken into consideration. Time-dependent phenomena, such as stress corrosion and slow

53

crack growth, can interfere with the determination of the fracture toughness at room and elevated temperatures.[50] At elevated temperatures, creep phenomena become significant and can cause stress relaxation in a bend bar specimen during a strength test. The fracture toughness of a ceramic could also vary slightly if individual bend bars were machined from different bulk samples having slightly different properties, such as density, grain-size, or other flaws or cracks.

The surface preparation of the test specimens can introduce machining damage, such as microcracks, machining damages, and/or residual stresses that may have a pronounced effect on fracture toughness.[50] The machining damage introduced during specimen preparation can be either a random interfering factor or an inherent part of the toughness characteristic and can also lead to residual stresses. Likewise, slow crack growth can lead to a rate-dependency of fracture toughness.[50]

2.4.2.2. Testing Methods

The fracture toughness of a ceramic can be determined in a number of ways, such as the Precracked Beam Method (pb), the Surface Crack in Flexure Method (sc), and the Chevron-Notched Beam Method (vb).[50] The pb and the vb fracture toughness values provide information on the fracture resistance of advanced ceramics containing large sharp cracks, while the sc fracture toughness value provides this information for small cracks comparable in size to natural fracture sources. The fracture toughness of each method is obtained based on the elastic stress analysis of the test specimen configuration.[50]

54

The pb method involves a straight-through precrack being created in a beam test specimen using the bridge-flexure technique, which is where the precrack is extended from median cracks associated with one or more Vickers indents or a shallow sawed notch. The fracture force of the precracked test specimen as a function of displacement, time, back-face strain, or actuator displacement is recorded in three- or four-point flexure tests. The fracture toughness, K_{Ic-pb}, is calculated from the fracture force, test specimen size, and measured precrack size. This stress intensity factor corresponds to the extension resistance of a straight-through crack formed via bridge flexure of a sawn notch or Vickers or Knoop indentation.[50]

In the sc method, a beam test specimen is indented with a Knoop indenter and polished until the indent and associated residual stress fields are removed. The fracture force of the test specimen is determined in four-point flexure tests, and the fracture toughness, K_{Ic-sc}, is calculated from the fracture force, the test specimen size, and the measured precrack size.[50]

The vb method involves the machining of a small divot, called a Chevron Notch, into a beam test specimen. The beam is then loaded into a three- or four-point flexure. The applied force versus displacement, time, back-face strain, or actuator displacement is recorded in order to detect unstable, or invalid, fracture. The fracture toughness, K_{Ic-vb}, is calculated from the maximum force applied to the test specimen after extension of the crack in a stable manner.[50] The Chevron-Notched Beam method was used for this research, and hence will be the only method discussed in further detail.

The microstructural features of advanced ceramics can give rise to R-curve behavior, which is a graphical relation of the crack-extension resistance of a material as a

55

function of the extension of a crack.[50,46] As such, the three aforementioned test methods are expected to result in different fracture toughness values because of the amount of crack extension prior to the relevant maximum test force, P_{max}, or because of the details of the precracking methods. With that being said, the fracture toughness values of ceramics generally increase in the following order: $K_{Ic\text{-}sc}$, $K_{Ic\text{-}pb}$, $K_{Ic\text{-}vb}$.[50] However, there is insufficient experience to extend this statement to all materials.

The fracture toughness of a ceramic material can be found using either three-point or four-point bend tests. Four-point bend tests are generally preferred because the entire gage section of the specimen, or the length of bend bar that lies between the two inner supports, is exposed to the highest bending moment, as opposed to a single point in three-point bend configurations. Four-point bend tests were the only method used during this research, and will thusly be discussed in further detail below.

For a Chevron-Notched bend bar specimen loaded into a four-point bend fixture, as seen below in Figure 2-18, the fracture toughness of a ceramic may be calculated using Equation 2-10, where Y_{min}^* is the minimum stress intensity factor coefficient, P_{max} is the relevant maximum force, S_o, is the outer span of the fixture, S_i is the inner span of the fixture, b is width of the bend bar specimen, and w is the thickness of the bend bar specimen.[46,50]

$$K_{lc-vb} = Y_{min}^* \left[\frac{P_{max}[S_o - S_i]10^{-6}}{bw^{3/2}} \right] \qquad \textbf{(2-10)}$$
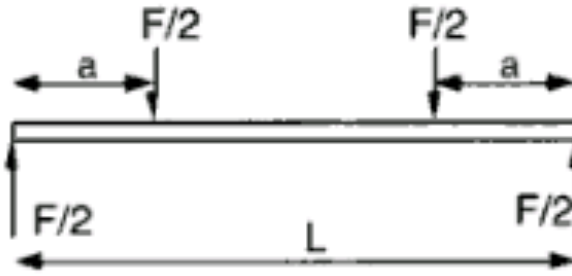
Figure 2-18: Four-point loading schematic.[46]

The minimum stress intensity factor coefficient, Y_{min}^{*}, is a dimensionless value that is derived using a straight through crack assumption and a subsequent curve fit of its relation to the notch length on each side of the bar, a_0 and a_1, and the bend bar height, as seen in Equation 2-11.

$$Y_{min}^{*} = \frac{0.5256 - 3.4872(a_o/w) + 3.9861(a_1/w) - 2.0038(a_1/w)^2 + 0.5489(a_1/w)^3}{1.0000 - 2.9050(a_o/w) + 2.7174(a_o/w)^2 - 0.8963(a_o/w)^3 + 0.0361(a_1/w)} \quad \textbf{(2-11)}$$

The fracture toughness of a material may depend on the material anisotropy, which depends on the principle pressing directions applied to during green body forming or during sintering. Thermal gradients during firing can also lead to microstructure anisotropy.[50]

The exact same theory and procedure as outlined above can also be used for determining the fracture toughness of ceramics at elevated temperature and ambient environmental conditions at a nominal, moderately fast testing rate.[50] The fracture

57

toughness under these conditions may or may not necessarily be the inherent fracture toughness because the mechanical property at elevated temperatures may be strongly dependent on testing rate, which is a result of creep, stress corrosion, or slow crack growth.[50]   Therefore, extra precautions are required and faster testing rates may be necessary if the inert fracture toughness is intended to be found at elevated temperatures.

2.4.3. FLEXURE STRENGTH

The flexure strength of a ceramic, σ_{fb}, is a measure of the ultimate strength of a specified beam undergoing bending. This mechanical property can also be viewed as the maximum surface stress present in a bent beam at the instant of failure.[45]   The flexure strength of a material is also known as the modulus of rupture and bend strength and is measured in terms of stress [Pa, psi].

2.4.3.1. Mechanical Theory

The flexure strength only applies to brittle materials such as ceramics.[46]   For ductile materials, the approximate equivalent mechanical property is the ultimate strength.[45]   The flexure strength of a material is important because it is a direct measure of the tensile strength of a ceramic material.   An increase in the flexure strength of the ceramic translates into the material being able to withstand a higher stress, and therefore a higher load, before failing.[48]

A bend bar test is used as opposed to a normal tension test specimen, such as a dog-bone test specimen, because the bend bar tests does not have to worry about the

material possibly failing or cracking from the stresses introduced by the grips used to hold the sample in place in a pure tension testing machine.[49]

The flexural strength of ceramics is greatly influenced by several parameters associated with the testing procedure, such as the testing rate, testing environment, specimen size, specimen preparation, and testing fixtures.[51] Likewise, the flexural strength is dependent on both its inherent resistance to fracture and the size and severity of flaws existing within the ceramic. Variations in these cause a natural scatter in test results for a given sample of test specimens.[46]

Because the porosity of a ceramic is highly correlated with its mechanical properties, reducing the number of defects in a ceramic is a common way of increasing its flexure strength.[45] Methods of decreasing the total number of flaws and pores in ceramic materials, such as controlling the grain-size and morphology of the material through careful processing parameters, can be found in Section 2.3.3 of this manuscript.

The flexural strength of a monolithic material has also been found to be increased with the addition of dopants to a matrix material in the form of whiskers and/or particulates, such as what has been done for this research. These additives, however, also tend to increase the final bulk density of the composite when compared to their monolithic counterpart.[45]

The flexural strength of a ceramic is not a quantity that fluctuates greatly, but it will vary slightly from one specimen to another. As a result, experimental errors must be taken into consideration. Time-dependent phenomena, such as stress corrosion and slow crack growth, can interfere with the determination of the flexural strength at room and elevated temperatures.[51] At elevated temperatures, creep phenomena become significant

59

and can cause stress relaxation in a flexure specimen during a strength test. The flexure strength of a ceramic could also vary slightly if individual bend bars were machined from different bulk samples having slightly different properties, such as density, grain-size, or other flaws or cracks.[49]

The surface preparation of the test specimens can introduce machining damage, such as microcracks, that may have a pronounced effect on flexural strength. The machining damage introduced during specimen preparation can be either a random interfering factor or an inherent part of the strength characteristic and can also lead to residual stresses. Likewise, slow crack growth can lead to a rate-dependency of flexural strength.[51]

2.4.3.2. Testing Methods

The flexure strength of a material can be found using either three-point or four-point bend tests because these methods eliminate the problem of specimen gripping and can be preformed on either machined or as-pressed specimens.[51] Four-point bend tests are generally preferred because the entire gage section of the specimen is exposed to the highest bending moment, as opposed to a single point in three-point bend configurations. Likewise, the three-point bend configuration also tends to over estimate the flexure strength of a material because of the stress concentrations produced at this point. Four-point bend tests were the only method used during this research, and will thusly be discussed in further detail below.[51]

For a specimen loaded into a four-point fixture, which may be seen above in Figure 2-18, the flexure strength may be calculated using simple beam theory, as seen in

Equation 2-12, where P is the force at which the bend bar specimen breaks, L is the outer support span of the testing fixture, b is the bend bar specimen width, and d is the bend bar specimen thickness.[46]

$$\sigma_{fb} = \frac{3Pa}{bd^2} \qquad \qquad \textbf{(2-12)}$$

This equation assumes that the material is isotropic and homogeneous, the modulus of elasticity in tension and compression are identical, and the material is linearly inelastic.[51]

In order for these calculations to be correct, the average grain-size of the material should be no greater than one-fiftieth of the beam thickness.[51] Because homogeneity and isotropy were assumed, the equations cannot be used for fiber-reinforced composites.[51]

The exact same theory and procedure as outlined above can also be used for determining the flexural strength of ceramics at elevated temperature and ambient environmental conditions at a nominal, moderately fast testing rate. The flexural strength under these conditions may or may not necessarily be the inherent flexural strength, because the mechanical property at elevated temperatures may be strongly dependent on testing rate, which is a result of creep, stress corrosion, or slow crack growth.[51] Therefore, extra precautions are required and faster testing rates may be necessary if the inert flexural strength is intended to be found at elevated temperatures.

61

2.4.4. ELASTIC MODULUS

The elastic modulus of a ceramic is a measurement of the stiffness of the material. This mechanical property can also be viewed as a measure of the interatomic bonding forces within the material.[46] The elastic modulus is also known as the Young's modulus or the modulus of elasticity, and is measured in terms of stress [Pa, psi].

2.4.4.1. Mechanical Theory

The elastic modulus of a material is an important mechanical property because it is a measure of the resistance of the material to relative atomic separation, which is inherently known as its stiffness.[12] Elastic properties of a material are a measure of the force required to displace atoms relative to one another. An increase in the elastic modulus of a ceramic material translates into a greater force that is required to move the atoms from their equilibrium position within a given ceramic body.[48] Therefore, materials with high elastic modulus values are stiff because they are better able to resist changes in dimension under an applied load.[49]

The elastic modulus of a material can be measured in a number of ways, including the sonic resonance method and the impulse excitation of vibration technique, which are both considered to be dynamic measurements, and the stress-strain method, which is considered to be static.[46] Both of the dynamics methods determine the elastic modulus of a ceramic material by analyzing its resonant frequency in the flexural mode of vibration.[45] The static method, which was used for this research and will further expanded upon, measures the elastic modulus by equating the linear elastic region of a stress-strain curve found from a three- or four-point bend test.

62

A strain gage is a transducer whose electrical resistance varies in proportion to the amount of strain in the device.[16] The most widely used gage is a metallic strain gauge that consists of a very fine wire or, more commonly, metallic foil arranged in a grid pattern, which maximizes the amount of metallic wire or foil subject to strain in the parallel direction.[16] The cross-sectional area of the grid is minimized in order to reduce the effect of shear strain. The grid is bonded to a thin backing, called the carrier, which is attached directly to the test specimen. Therefore, the strain experienced by the test specimen is transferred directly to the strain gauge, which responds with a linear change in electrical resistance. A fundamental parameter of the strain gauge is its sensitivity to strain, which is expressed quantitatively as the gauge factor, and is defined as the ratio of fractional change in electrical resistance to the fractional change in length.[16]

The elastic modulus of ceramics is greatly influenced by several parameters associated with the testing procedure, such as the testing rate and environment, specimen size and preparation, and the testing fixtures for bend tests. Likewise, the elastic modulus is heavily dependent on the size and severity of flaws existing within the ceramic because of the fact that plastic deformation mainly involves the dislocation movements along slide planes.[46] A high stress is required to surpass the elastic zone and enter the plastic deformation region. Sliding along certain crystallographic planes will result in entanglement of grain boundary, which will then grow in to microcracks that will eventually result in catastrophic failure of the ceramic.[46] Therefore, it is imperative that the number of defects within given ceramic be kept to a minimum in order to keep the elastic modulus at a maximum.

63

As such, reducing the number of defects in a ceramic is a common way of increasing its elastic modulus. Methods of decreasing the total number of flaws and pores in ceramic materials, such as controlling the grain-size and morphology of the material through careful processing parameters, can be found in Section 2.3.3 of this manuscript.

Dopants to a given matrix material in the form of whiskers and/or particulates, such as what has been done for this research, has also been found to increase the elastic modulus.[46] These additives, however, also tend to increase the final bulk density of the composite when compared to their monolithic counterpart.

The elastic modulus of a ceramic does not fluctuate greatly from sample to sample, but it will vary slightly. As a result, experimental errors must be taken into consideration. For static tests using a three- or four-point bend machine, time-dependent phenomena, such as stress corrosion and slow crack growth, can interfere with the determination of the flexural strength at room and elevated temperatures. At elevated temperatures, creep phenomena become significant and can cause stress relaxation in a flexure specimen during a strength test.[51]

The strain gage itself could also cause an error in the elastic modulus measurements. An ideal strain gage would change resistance only due to the deformations of the surface of the test specimen. However, in real applications, temperature, material properties, the adhesive that bonds the gage to the surface, and the stability of the specimen material all affect the detected resistance.[16]

64

The elastic modulus of a ceramic could also vary slightly if individual specimens were machined from different bulk samples having slightly different properties, such as density, grain-size, porosity, or other flaws or cracks.

The surface preparation of the test specimens can introduce machining damage, such as microcracks, that may have a pronounced effect on the measured elastic modulus. The machining damage introduced during specimen preparation can be either a random interfering factor or an inherent part of the strength characteristic and can also lead to residual stresses.[51]

2.4.4.2. Testing Methods

As previously mentioned, static, rather than dynamic, tests were used to measure the elastic modulus of ceramic samples that were manufactured for this research. In static testing, a three- or four-point bend fixture is used in order to determine the stress of the sample. For a specimen loaded into a four-point fixture, which was used for this research, the flexure strength, or stress, may be calculated using Equation 2-12 from Section 2.4.3.2.

The strain of the sample may be determined by the use of a strain gage that is positioned on the center of the tensile face within the gage section of the bar in a direction that is parallel with its length.[48]

The influences on the elastic modulus and its accuracy using this type of testing are similar to that of bend testing, which was discussed in Section 2.4.3.1 of this manuscript. Delayed elastic and creep effects would invalidate elastic modulus measurements using the static technique at elevated temperatures.[46]

65

2.4.5. BORON CARBIDE

Table 2-1 below represents a summary of the mechanical properties for 99 wt% or greater B_4C having a relative density, ρ, of 2.5 ± 0.1 g/cm^3 and an average carbon content, *wt% C*, of close to 20.[3,52,53]

Table 2-1: Mechanical properties of ≥ 99 wt% B_4C, ρ = 2.5 ± 0.1 g/cm^3, *%C* = 20.0.[3,52,53]

Mechanical Property	Temperature 20 °C
Density [g · cm^{-3}]	2.52
Bulk Modulus [GPa]	245
Elastic Modulus [GPa]	360 – 460
Flexural Strength [MPa]	300 – 500
Fracture Toughness [MPa · m$^{1/2}$]	2.9 – 3.7
Poisson's Ratio [ ]	0.18
Shear Modulus [GPa]	158 – 188
Vickers Hardness (1000 g$_f$ load) [GPa]	30 – 38
Thermal Expansion Coefficient [10^{-6} · K^{-1}]	3.1

Because of the chemical bonding associated with the material, B_4C has an extremely high melting temperature of 2490 °C (4514 °F) and thusly requires an extremely high sintering temperature.[3]

66

2.4.6. SILICON CARBIDE

Table 2-2 below represents a summary of the mechanical properties at respective testing temperatures of 20 °C, 500 °C, 1000 °C, and 1200 °C for 99 wt% or greater SiC having a relative density, ρ, of 3.1 ± 0.1 g/cm^3 and an average grain-size, g, of 6 ± 2 µm.[36]

Table 2-2: Mechanical properties of ≥ 99 wt% SiC, ρ = 3.1 ± 0.1 g/cm^3, g = 6 ± 2 µm.[36]

Mechanical Property	Temperature [°C]			
	20	500	1000	1200
Density [g · cm^{-3}]	3.16	3.14	3.11	3.10
Bulk Modulus [GPa]	203	197	191	188
Elastic Modulus [GPa]	415	404	392	387
Flexural Strength [MPa]	359	359	397	437
Fracture Toughness [MPa · m$^{1/2}$]	3.1	3.1	3.1	3.1
Poisson's Ratio [ ]	0.160	0.159	0.157	0.157
Shear Modulus [GPa]	179	174	169	167
Vickers Hardness (1000 g$_f$ load) [GPa]	32.0	17.0	8.9	-
Thermal Conductivity [W · m^{-1} · K^{-1}]	114.0	55.1	35.7	31.3
Thermal Expansion Coefficient [10^{-6} · K^{-1}]	1.1	4.4	5.0	5.2

Because of the mostly covalent bonds, SiC has an extremely high melting temperature of 2730 °C (4946 °F) and thusly requires an extremely high sintering temperature. Silicon carbide does not oxidize very readily at any temperature.

67

2.4.7. TITANIUM DIBORIDE

Table 2-3 below represents a summary of the mechanical properties at respective testing temperatures of 20 °C, 500 °C, 1000 °C, and 1200 °C for 98 wt% or greater TiB_2 having a relative density, ρ, of 4.5 ± 0.1 g/cm^3 and an average grain-size, g, of 9 ± 1 μm.[39]

Table 2-3: Mechanical properties of ≥ 98 wt% TiB_2, ρ = 4.5 ± 0.1 g/cm^3, g = 9 ± 1 μm.[39]

Mechanical Property	Temperature [°C]			
	20	**500**	**1000**	**1200**
Density [g · cm^{-3}]	4.500	4.449	4.389	4.363
Bulk Modulus [GPa]	240	234	228	-
Elastic Modulus [GPa]	565	550	534	-
Flexural Strength [MPa]	400	429	459	471
Fracture Toughness [MPa · m$^{1/2}$]	6.2	-	-	-
Poisson's Ratio [ ]	0.108	0.108	0.108	-
Shear Modulus [GPa]	255	248	241	-
Vickers Hardness (500 g$_f$ load) [GPa]	25.0	11.0	4.6	-
Thermal Conductivity [W · m^{-1} · K^{-1}]	96.0	81.0	78.1	77.8
Thermal Expansion Coefficient [10^{-6} · K^{-1}]	7.4	7.9	8.6	8.8

Because of the covalent and ionic bonds associated with the material, TiB_2 has an extremely high melting point of 3225 ± 25 °C (5837 ± 77 °F) and thusly requires a high sintering temperature. Oxidation of TiB_2 becomes severe at 1373 °C to 1673 °C (2503 °F to 3043 °F).

2.5. TOUGHENING MECHANISMS

In order to have a full understanding of the toughness of a ceramic material, it is essential to understand the mechanisms that can occur during fracture. Some of these mechanisms can involve the microstructure of a material, and thus, its manipulation can be used to enhance its mechanical properties.[46] Toughening mechanisms can broadly be classified into three groups that deal with cracktip interaction, cracktip shielding, and crack bridging.

2.5.1. GRAIN BOUNDARY STRENGTHENING

Grain boundary strengthening, also known as Hall-Petch strengthening, is a method of strengthening a ceramic material by changing the average grain-size.[12] The method is based on the on the observation that grain boundaries impede dislocation movement and that the number of dislocations within a grain have an effect on how easily dislocations can traverse grain boundaries and travel from grain to grain.[54] Like point and line defects, the presence of grain boundaries impedes the motion of dislocations and, therefore increases the stress necessary to promote dislocation motion, which is also known as plastic deformation.[46] The overall strength of a ceramic material, σ_{ys}, increases with decreasing grain-size because grain boundaries are an effective obstacle to dislocation motion and because small-grained materials have a higher density of grain boundaries per unit volume. This relationship of grain-size and material strength may be seen analytically in Equation 2-13, where σ_o is a constant stress value related the resistance of the lattice to dislocation motion for a given material, k_y is the material-

69

unique constant strengthening coefficient that describes the strength of the boundary interaction, and d is the average grain-size.[16]

$$\sigma_{ys} = \sigma_o + \frac{k_y}{\sqrt{d}} \qquad\qquad \textbf{(2-13)}$$

Therefore, by decreasing the grain-size of a ceramic, the dislocation movement can be influenced.

2.5.2. CRACKTIP INTERACTION

The ultimate goal of the cracktip interaction fracture toughening mechanism is to essentially place obstacles, such as second-phase particles, fibers, whiskers, or even regions that are simply difficult to cleave, in the crack path to impede crack motion.[46] Crack bowing and crack deflection are the two major ways of implementing cracktip interaction toughness mechanisms. Crack bowing produces a nonlinear crack, while crack deflection produces a nonplanar. In a real situation, a combination of bowing and deflection may occur. Likewise, it is expected that stress concentrations or residual stresses associated with the obstacles would play a role in this process as well.[46]

2.5.2.1. Crack Bowing

In crack bowing, a crack front becomes pinned by the obstacles and bypasses them by bending, or bowing, around them. The cracks remain on virtually the same plane in this process, as seen in Figure 2-19.[46] Crack bowing originates from resistant second-phase components in the path of a propagating crack. It has been suggested that

70

the interaction of a crack front with two or more inhomogeneities in a brittle matrix can increase its length and therefore the fracture energy along with the strength.
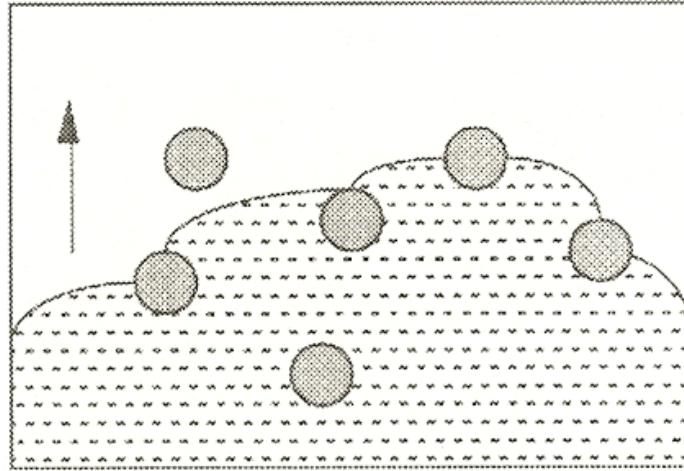
Figure 2-19: Crack bowing caused by interaction with tough obstacles.[46]

This toughening mechanism has been analyzed and theoretically shown to relate the crack resistance force to the matrix fracture surface energy, obstacle spacing, and the line tension of the crack front.[46] The obstacles are theoretically impenetrable, but it is known in reality that the strength and toughness of such obstacles are a key issue. For example, the obstacle could fail before the bowing process is complete or the obstacles would be left behind as unbroken ligaments behind the cracktip, which would result in the crack bowing becoming a precursor to crack bridging (Section 2.5.3). The crack bowing theory is not fully developed nor is it fully understood. Experimental studies related to this theory are rare and a detailed theoretical model encompassing all details associated with the mechanism does not exist. Instead, empirical models are used.[46]

71

2.5.2.2. Crack Deflection

An alternative way to by-pass obstacles is by crack deflection, which is the deflection of a cracktip by tilting of the crack path about an axis parallel to the crack front or twisting of the crack front about an axis normal to the crack front, as seen in Figure 2-20-A and B, respectively.[46]

<div style="text-align:center">A.   B.</div>
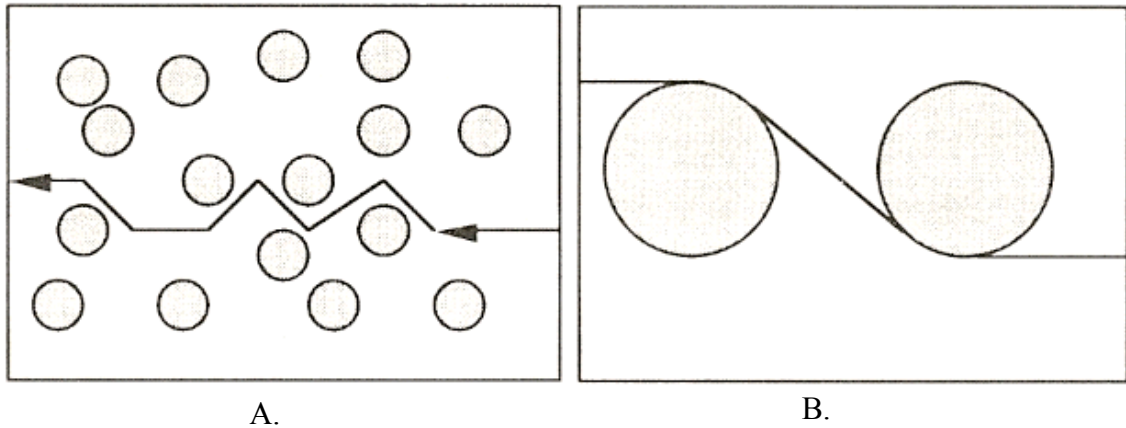
Figure 2-20: Schematic representation of crack deflection: -A. the crack path tilts to avoid obstacles; -B. the crack front twists to bypass obstacles.[46]

This overall deflection process results in a jagged fracture surface on the specimen because the change in orientation of the crack plane during deflection leads to a reduction of the crack extension force.[54] If a crack is deflected out of the plane that is normal to an applied unixaial tensile stress, the crack is no longer loaded in a simple Mode I and is therefore not subjected to the maximum tensile stress.[46]

It has been shown through fracture mechanism analysis that the twist component in deflection contributes most to the fracture toughness.[46] Likewise, for a random array of objects within a ceramic material, it has been shown that the amount of increased

toughness that is achieved is dependent on the volume fraction and shape of the particles. Figure 2-21 represents a schematic representation of the predicted differences between rod, disk, and sphere-shaped obstacles, where G_c represents the crack resistance force of a ceramic material and G_m represents its crack resistance.[46] As seen in the figure, the majority of the toughening from crack deflection appears to develop from volume fractions of obstacles less than about 20% for rods and disks, and less than about 40% for spheres.
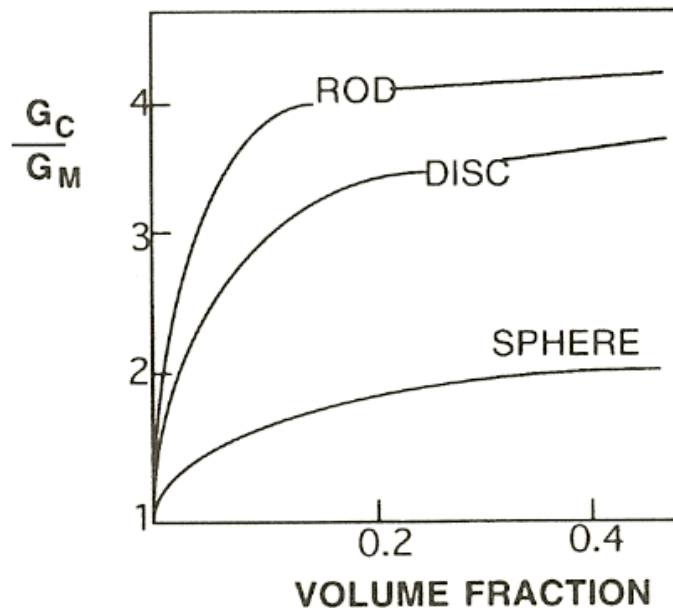
Figure 2-21: Obstacle shape dependence of crack deflection toughening.[46]

Because the crack deflection analysis does not consider the process by which the crack deflection occurs, it cannot be assumed that an increase in crack deflection implies an increase in fracture toughness.[46] This is because the theoretical analysis does not include the local stress fields at a given obstacle, which more than likely plays a large

73

role in the deflection process, and it does include the idea that deflection could be the result of the presence of a low-toughness interface or cleavage plane.

2.5.2.3. Ultra-Tough Particulate Reinforcement

A ceramic material can be toughened through the use of ultra small, ultra tough particulate reinforcements.[46] These particulates are so small that they begin to approach their theoretical cleavage stress, σ_{TH}, which is known as the maximum strength expected from a material based on the strength of the atomic bonding within, and is found to be a material property.[12] This value is related to the elastic modulus of the material, E, the specific surface energy, γ, and the equilibrium interplannar spacing between the lattice planes under zero stress, d_0, as seen in Equation 2-14.[45]

$$\sigma_{TH} = \sqrt{\frac{2E\gamma}{d_0}} \qquad \textbf{(2-14)}$$

This theoretical cleavage stress has been found to be approximately equal to one-tenth the magnitude of the elastic modulus of the material, which is on the order of one hundred or more times greater than that of actual observed values for a given material.[45] The disparity between the theoretical and actual values, however, can be attributed to the presence of defects within the crystal structure of the material.

In 1920, A. A. Griffith postulated that materials inherently contain flaws, or cracks, and it is the stress concentrations associated with these flaws that result in strength values being less than the aforementioned theoretical values. Thus, fracture is

74

dependent on the extension of pre-existing cracks, rather than on the theoretical separation of two perfect atomically bonded crystal planes.[45]

Griffith hypothesized that the free energy of a cracked body under stress should decrease during crack extension. Energy exchange occurs as a given crack extends, which implies that cracks cannot grow unless the process is energetically favored. In other words, energy is required to form new surfaces as a given crack extends through a material.[45] This energy must be supplied either by a corresponding reduction in the internal strain energy of the cracked body, or the work done by the external forces, or by a combination of the two. This theory may be observed when a crack of length a has grown into a material having a depth of unity and being subjected to a stress, σ, as seen in Figure 2-22.[46]
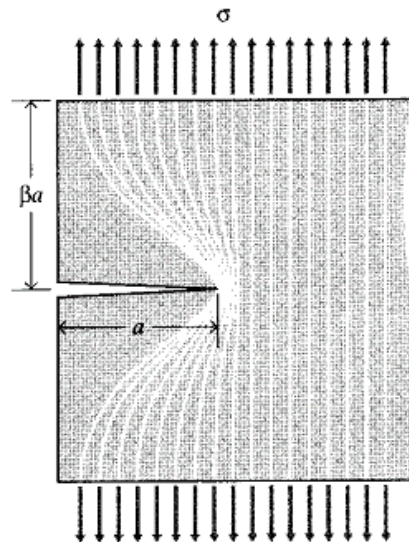
Figure 2-22: Idealization of unloaded regions near the flanks of an extending crack.[46]

The regions adjacent to the free surfaces of the crack in this figure are unloaded and their strain energies are released. A simple way of visualizing this energy release is to view

75

two somewhat triangular regions near the flank of the crack and having a width of a and a height of βa as being completely unloaded, while the remaining material continues to feel the full stress.[45] The parameter β is dependent on the type of loading present, and is equivalent to π for plane strain loading. The total strain energy released, U, is then equivalent to the product of the strain energy per unit volume of the stressed material and the volume in both of these triangular regions, as seen in Equation 2-15.[46] The overall value of the strain energy is negative because it is being released from the material and is liberated by crack growth.

$$U = -\frac{\sigma^2}{2E} \pi a^2 \qquad (2\text{-}15)$$

In forming this crack, however, bonds must be broken, and the required bond energy is in effect absorbed by the material.[45] The surface energy, S, associated with the crack length is related to the surface energy of the material, γ, and the number of surfaces that are formed, which is equal to 2 in this case, as seen in Equation 2-16.[46] This value is positive because it is being absorbed by the material.

$$S = 2\gamma a \qquad (2\text{-}16)$$

The total energy of the system in Figure 2-22 is then equal to the sum of the strain energy released by the material and the surface energy absorbed by the material in order to create the new surfaces.[46]

www.manaraa.com

As seen in Figure 2-23, as the crack grows longer and the value of the crack

length is increased, the overall energy of the system will eventually begin to decrease.[46]

This is because the crack length follows a quadratic relationship for the strain energy,

which is negative for the overall system, and follows a linear relationship for the surface

energy, which is positive overall. The crack length at which the overall energy of the

system begins to decrease is known as the critical crack length, a_c, and any crack that is

larger than this critical value can grow in a spontaneous and catastrophic manner.[12] Up to

this critical crack length value, however, and the crack will grow only if the stress in

increased.[46]
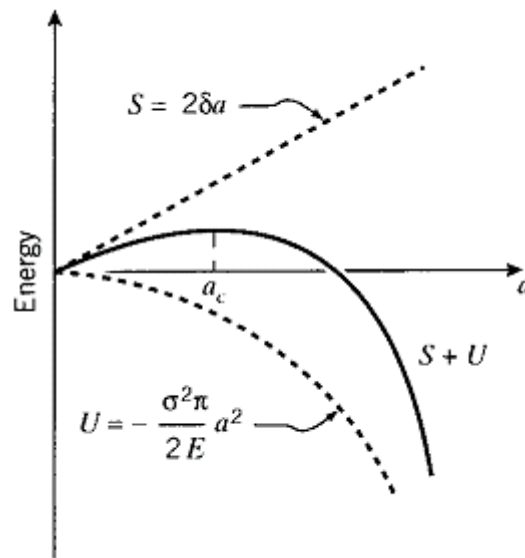
Figure 2-23: Fracture energy of a material as a function of crack length.[46]

Each time a given crack extends through the material, an additional quantity of

strain energy is released from the newly-unloaded material flanking the cracktip. Using

the simplistic view that these zero-stress areas of the material are triangular-shaped and that the rest of the material continues to experience the overall applied stress, as seen in Figure 2-24, it is easy to understand the concept that much more energy is released as a crack propagates from location 1 to location 2 because the resultant triangular areas are significantly increased.[48]
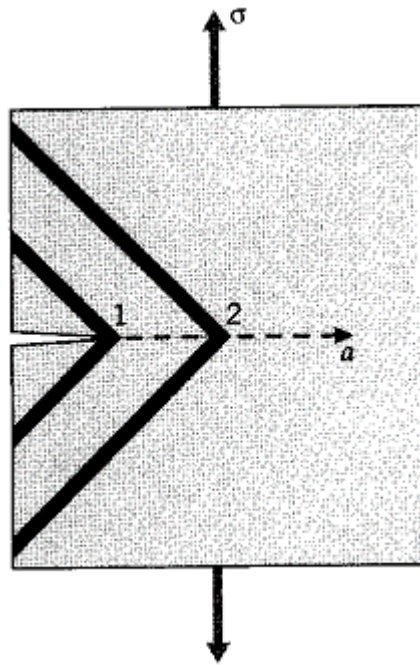
Figure 2-24: Energy released during an increment of crack growth.[48]

It is important to realize that the critical crack length is an absolute number, and is not dependent on the overall size of the material that contains it.[45] With this in mind, some particles are so small that they simply do not have a critical crack length at all. The strength of these materials approaches that of the theoretical cleavage stress as the diameter, and thus the overall size of the particle, decreases.[45] This is because the

78

theoretical cleavage strength of a material is based upon the energy required to pull apart a material specimen that is as small as only two planes of atoms. In other words, small particulates are not large enough to contain a critical-length crack. Therefore, these types of small particles do not fully follow the normal critical crack length failure that was presented previously.[48]

2.5.3. CRACKTIP SHIELDING

The stresses near a cracktip in a given linear elastic material are directly related to the applied stress intensity factor. In some materials, non-linear deformation behavior may occur in the high-stress zone at the cracktip, which will effectively change the stresses at the cracktip and can often be described by a local stress intensity factor.[46] The stresses are reduced and the process zone is said to shield the cracktip from the applied loads. The cracktip shielding toughening mechanism occurs if the applied stress intensity factor becomes greater than the local stress intensity factor.[46] The two most common toughening mechanisms that deal with cracktip shielding are transformation toughening and stress-induced microcracking. In transformation toughening, the primary toughening factor is the effects caused by a change in volume of the material in the process zone, while the primary factor of microcracking is associated with residual stress fields.[46]

2.5.3.1. Transformation Toughening

During sintering, some ceramic materials may experience a stress-induced materialistic phase transformation that results in shear deformation and a volume change.[46] Ceramics that contain second-phase particles that transform often have

79

improved toughens. At a critical stress, the secondary-phase material transforms and results in both shear strains and dilatational strains, which is a transition in which the crystal structure is compressed along one or more crystallographic directions.[45] This transformation lowers the local crack driving force and thus toughens the material. The transformed second-phase particles are retained within the matrix material because of the constraint on the particles that is produced by the surrounding matrix material and, as such, the retention level is dependent on the matrix material. During the transformation process, large amounts of strain energy are produced by the surrounding material, which acts to oppose the transformation.[46]

An example of such a transformation within a ceramic material may be seen in Figure 2-25-A and -B.[46] Figure 2-25-A shows a cracktip process zone where second phase particles have been transformed and Figure 2-25-B represents a plot of the stress distribution ahead of the cracktip. The stress field in this process zone is lower because of the dilatational effects, which are the effects caused by a change in volume of the material. The stress field outside of this zone, however, is higher and completely dependent on the global stress intensity.[46]

The toughening of a ceramic material, like the one pictured in Figure 2-25, is caused by more work being required for a crack to extend when the local stresses are reduced.[46] The vast majority of toughening occurs at the area behind the cracktip because the area is in a state of residual compression due to the zone dilation being constrained by the surrounding non-transformed material.

A.   B.
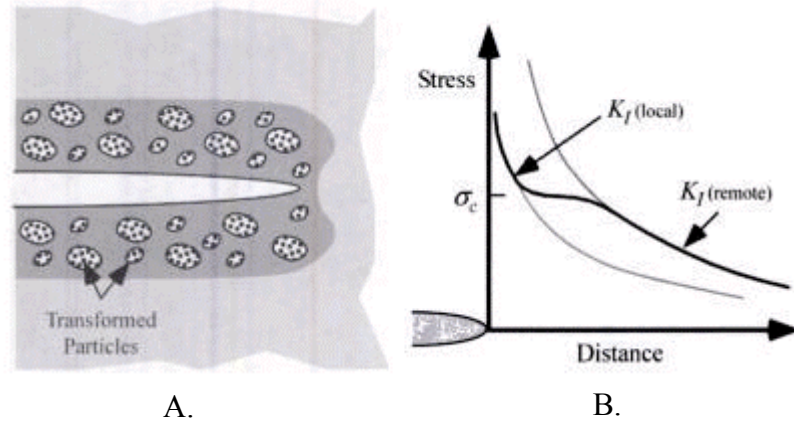
Figure 2-25: Transformation toughening mechanism: -A. Cracktip approaching a portion of a ceramic that has undergone transformation toughening; -B. Plot of the stress distribution in front of the cracktip.[46]

Zirconium dioxide (ZrO_2) is often the most widely used and studied material that exhibits one of these stress-induced materialistic transformations because of its well-known phase transformation from tetragonal to monoclinic.[45]

2.5.3.2. Microcracking

Stress-induced microcracking has also been shown to increase the fracture toughness of a ceramic by giving rise to cracktip shielding.[46] Ceramics that contain localized residual stresses are known to be capable of microcracking, and these residual stresses form because of phase transformations, thermal expansion anisotropy in single-phase materials, and mismatches in thermal expansion and/or elastic modulus in multiphase materials.[46]

If the microstructure of a given ceramic can be altered so that it contains microscopic voids or cracks, as seen in Figure 2-26, then the cracktip radius of an advancing crack entering one of these voids is increased, which thusly decreases the

81

stress concentrations.[12,46] Although the crack length also increases upon entering the microvoid, the tip radius increases by a much larger factor. Therefore, a decrease in the driving force for crack extension is achieved.
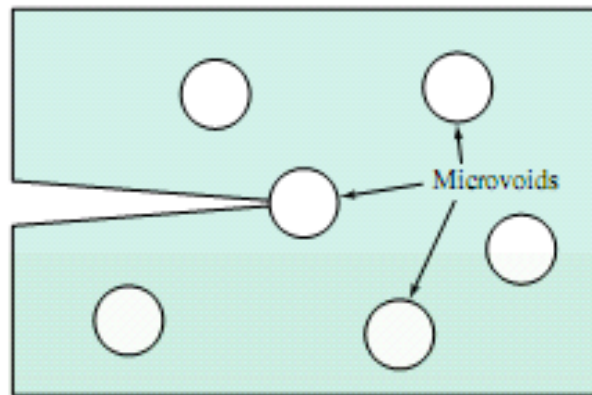
Figure 2-26: Schematic of microcracking toughening in which an approaching crack enters a microvoid.[12]

Microcracks can form spontaneously during the fabrication process if the grain or particle site is above some specific critical value and are expected to form in a zone around larger cracks, which would allow for a reduction in the stress concentrations near the cracktip.[46] The formation of microcracks releases the strain energy from the ceramic material, which results in an increase in compliance. If this change in compliance is gradual, as existing microcracks grow and as new cracks form, a non-linear stress-strain curve results.[46]

In general, the mechanism is relatively ineffective because stable crack growth does not usually occur in ceramic materials. With that in mind, materials undergoing

microcracking are expected to have relatively low strengths, because the microcracks are likely failure origins.[46]

2.5.4. Crack Bridging

When a cracktip bypasses a reinforcing object, it is possible that the object is left intact as a ligament behind the cracktip. These left-behind ligaments give rise to crack bridging toughening, which will make it more difficult to open a crack at a given applied stress and will therefore increase the fracture toughness of a ceramic material.[46] It is expected that the bridging zone will reach a limiting size and will then move in conjunction with the cracktip. Crack bridging has been observed in frictionally bonded fiber composites, in large-grained polycrystals, in whisker-reinforced ceramics, and in cermets, which are ceramic-metal composites. In a portion of the current research, the reinforcing material is frictionally bonded to the matrix. This means that the reinforcement phase and the matrix are purely, or nearly purely, mechanically bonded, which results in the mechanical interlocking of grains.[46] Figure 2-27 represents an example of bridging, in which unbroken ligaments are left behind the cracktip within the bridging zone.[46] Behind the bridging zone, however, and the left-behind ligaments begin to pullout, which is the physical removal of the object because of an applied load.
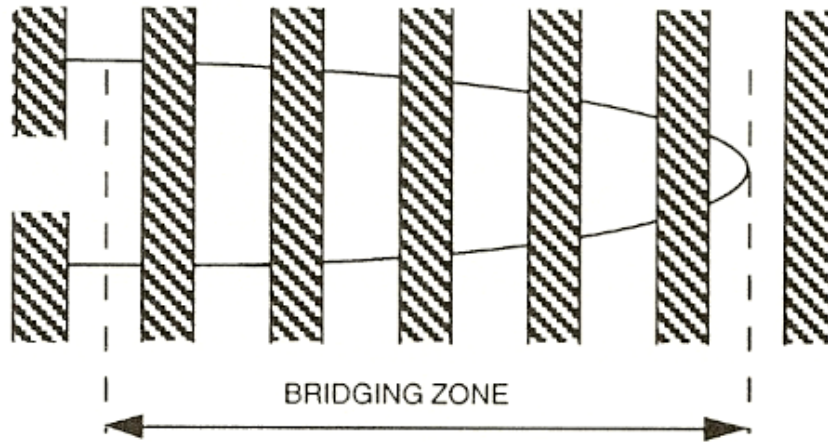
Figure 2-27: Crack bridging, in which unbroken ligaments are left behind the tip.[46]

The ultimate type of crack bridging is the fully bridged crack, which is mostly observed in fiber-reinforced ceramic composites.[46] In this case, a crack passes through the matrix and leaves the fibers fully intact. This process can be repeated many times over without the composite failing. The tensile loading behavior of this type of material is initially elastic until a crack passes through the matrix at a particular stress.[46] This crack then by-passes, or bridges, the fibers and leaves them available for load carrying. The by-pass process usually involves debonding of the fiber. Further loading causes the formation of regularly spaced matrix cracks until the fibers fail at the peak load. The ensuing failure, however, is not necessarily catastrophic as the fibers can continue to pull out of the matrix as the applied stress is increased. Figure 2-28 represents a plot of the stress and strain of a fully bridged crack material, where σ_{mc} denotes the onset of matrix cracking.[46] In these materials, the final failure is not the result of the propagation of a single crack and, thus, a fracture toughness value cannot be defined.

84
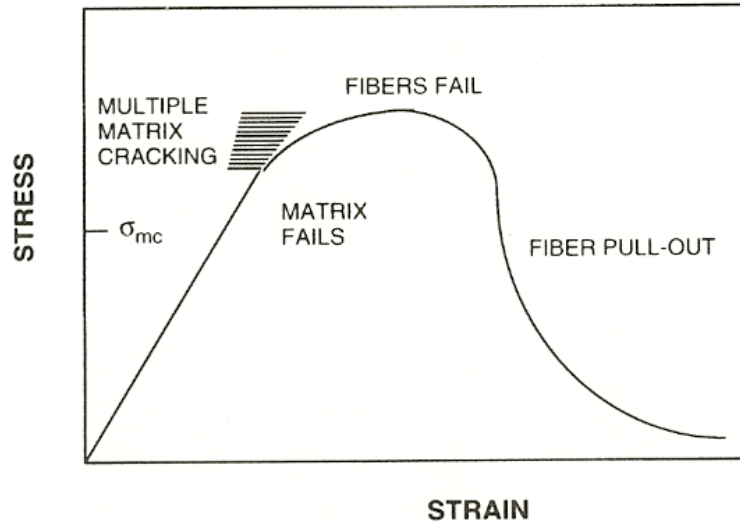
Figure 2-28: Stress versus strain curve for a material undergoing a fully bridged crack.[46]

With this concept of crack bridging in mind, the fiber-reinforced composites do not undergo catastrophic failure in uniaxial tensile loading even though the matrix and fibers are composed of brittle materials. Therefore, this ductile type of behavior for a material composed of two brittle components is particularly attractive for structural applications.[46]

85

CHAPTER 3: EXPERIMENTAL METHODOLOGY

The methodology that was followed to process, characterize, and mechanically test the boron carbide-based ceramics used in this investigation is outlined in the following sections.

3.1. POWDER PROCESSING

The following sections deal with the procedures that were taken to process the ceramic samples of the various powder compositions, and includes a summary of the obtained raw powders, as well as the steps taken during blending, forming, and sintering along with the final finishing steps that were performed on the materials.

3.1.1. RAW CERAMIC POWDERS

Three different types of powders were used in this investigation, submicron-sized boron carbide (Grade HS; H.C. Starck, Berlin, Germany), nano-sized alpha silicon carbide (Grade GC #30000; Fujimi Corporation, Kiyosu, Japan), and micron-sized titanium diboride (Grade HCT-30; GE Advanced Ceramics, Cleveland, Ohio). A summary of the manufacturer supplied data for the B_4C, SiC, and TiB_2 powders may be seen below in Table 3-1, Table 3-2, and Table 3-3 respectively. The tables include an

overview of the size distribution of the powder particles and an analysis of the amounts

and types of chemical constituents within each.

Table 3-1: Material data of B_4C powder (Grade HS; H.C. Starck, Berlin, Germany).

Surface Area	18.0 m^2/g
Particle Size	90 % of particles $\leq$ 3.41 μm
	50 % of particles $\leq$ 0.89 μm
	25 % of particles $\leq$ 0.24 μm
Chemical Analysis	75.40 wt % B
	22.40 wt % C
	1.40 wt % O
	0.30 wt % N
	0.09 wt % Si
	0.04 wt % Fe
	0.01 wt % Al
	0.30 wt % Other
B : C Ratio	3.74 : 1

Table 3-2: Material data of α-SiC powder (Grade GC #30000; Fujimi Corporation, Kiyosu, Japan).

Surface Area	24.90 m^2/g
Particle Size	95 % of particles $\leq$ 0.58 μm
	50 % of particles $\leq$ 0.29 μm
	25 % of particles $\leq$ 0.20 μm
Chemical Analysis	0.04 wt % SiO_2
	0.02 wt % free C
	0.02 wt % free Si

87

Table 3-3: Material data of TiB$_2$ powder (Grade HCT-30; GE Advanced Ceramics, Cleveland, Ohio).

Surface Area	0.25 m^2/g
Particle Size	90 % of particles $\leq$ 30.5 μm
	50 % of particles $\leq$ 16.4 μm
	25 % of particles $\leq$ 11.2 μm
Chemical Analysis	67.000 – 69.000 wt % Ti
	29.000 – 32.000 wt % B
	0.467 wt % C
	0.366 wt % O
	0.055 wt % N
	0.020 wt % Fe
	0.015 wt % Zr
B : C Ratio	1.917 : 1 – 2.054 : 1

3.1.2. POWDER BLENDING

In order to ensure the homogeneous distribution of constituents within the final sintered composite specimens, the raw powders were first carefully weighed into the given percentages for each composition and then blended. The weighing of powder was measured using a scale (Adventurer AR3130; Ohaus Corporation, Pine Brook, NJ) having a resolution of 0.0005 g$_f$ (2E^{-5} oz$_f$). The volume and equivalent mass percentages, theoretical densities, and average starting powder sizes for each of the constituents used for the B$_4$C-based compositions may be seen below in Table 3-4.

88

Table 3-4: Volume and mass percentages, theoretical densities, and relation to the average powder size for each of the B_4C-based compositions.

Material	Material vol% [%]	Equivalent Material wt% [%]	Theoretical Density [g/cm^3]	Average Starting Powder Size [μm]
B_4C	100.00	100.00	2.520	0.89
B_4C / SiC	90.00 / 10.00	87.60 / 12.40	2.589	0.89 / 0.29
	80.00 / 20.00	75.85 / 24.15	2.658	0.89 / 0.29
B_4C / TiB$_2$	90.00 / 10.00	83.41 / 16.59	2.719	0.89 / 16.4
	80.00 / 20.00	69.09 / 30.91	2.918	0.89 / 16.4

Once the powders for the composite materials were measured into the appropriate weight proportions for each respective composition, the powders were then poured into polyethylene bottles (Nalge Nunc International, Rochester, NY) and three rough handfuls of cylindrical zirconium dioxide milling media were added so that about 90% of the total bottle weight was made up of mixing media. Before the bottles and milling media were first used, they were cleaned with labware cleaner, rinsed with acetone, and subsequently dried at about 125 °C (257 °F) for 1 hour. Two separate bottles and sets of milling media were used for this investigation, one for the SiC powders and one for the TiB$_2$ powders. In order to limit the amount of contamination from the polyethylene bottles and the milling media, pure boron carbide powder was first milled for 12 hours and then discarded in order to coat the insides of the bottles as well as the media themselves.

Once the powder was added, the bottles were then placed on a mixing machine for 6+ hours at a rotation speed of about 200 rpm. A 325 mesh sift was then used to

89

separate then mixed powder from the milling media and break apart any conglomerates of powder that had accumulated during the blending process.

3.1.3. FORMING

Mixed powders were poured into graphite die-plunger assemblies (Grade ISO-63; Graphite Products Corporation, Madison Heights, MI) and subjected to a uniaxial pressing force in order to create green compacts having about 35% theoretical density. The dies had an inside diameter of 50.8 mm (2 in), an outside diameter of 88.9 mm (3.5 in), and a thickness of 50.8 mm (2 in). Graphite plungers having a diameter of 50.8 mm (2 in) and a thickness of 25.4 mm (1 in) were used to secure the bottom and the top of the die assembly. Graphite foil (Grade GTB; GrafTech International Ltd, Cleveland, OH) was used to encompass the powder in order to protect the die assembly and aid in the removal of the sintered compact. Foil was placed around the inside diameter of the die as well as above and below the powder. A small ring of 11 mm (0.4375 in) thick graphite felt (Weaver Industries Inc., Denver, PA) was used to surround the graphite die assembly in order to lower the amount of convective heart transfer to the surrounding vacuum chamber. Once the powders were loaded into dies, they were subjected to a uniaxial pressing force of about 69 MPa (10 ksi) through the use of a mechanical hydraulic press. An exploded view schematic of the die-plunger setup may be seen in Figure 3-1.
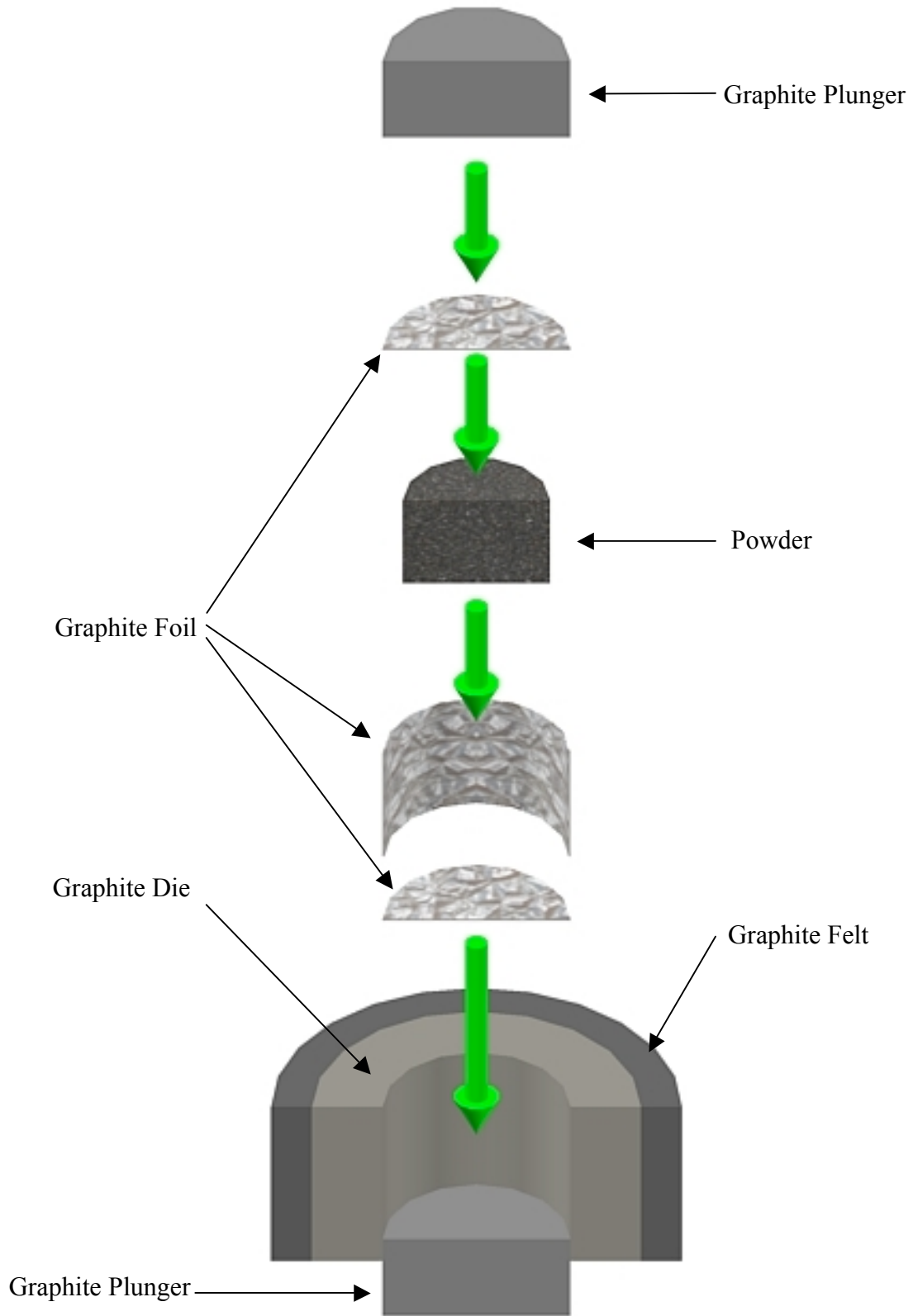
90

Figure 3-1: Exploded view of the die-plunger setup.

91

3.1.4. SINTERING

The die assembly was placed in between the two graphite-capped 6" diameter water-cooled copper electrodes of the $P^2C^®$ apparatus. The bottom electrode was then carefully raised towards the top stationary electrode using a mechanical hydraulic press and a uniaxial pressure of about 15 MPa (2175 ksi) was applied. This pressing force held the entire die assembly together in compression and provided an initial path for current flow, which also ensured that sufficient inter-particle contact was established. The chamber door to the apparatus was sealed and a vacuum pump was powered. When the vacuum level within the chamber reached a value of about 10^{-3} torr (10^{-5} psi), a pulsed DC current of about 2000 A at a constant voltage was applied through the powder compact using a full-wave-rectified power supply in order to heat the powder compact to a temperature of 650 °C to 750 °C (1202 °F to 1382 °F). At this temperature, adsorbed gases, moisture, and contaminates were eliminated, which was confirmed by a marginal drop in the vacuum level. The pulsed current was applied until the vacuum level reached a plateau and again attained its initial value, which took about 30 minutes. After pulsing, a direct current was applied through the powder compact resulting in Joule heating.

Consolidation was carried out in a vacuum at maximum temperatures between 1750 °C and 1850 °C (3182 °F to 3362 °F) for 10 to 20 minutes at an applied pressure of 30 MPa (4350 ksi). Heating rates from the final pulsing temperature up to 1000 °C (1832 °F) was held constant at a rate of about 15 to 20 °C/min (59 to 68 °F/min), and was subsequently reduced to 5 to 10 °C/min (41 to 50 °F/min) at temperatures above 1000 °C in order to decrease the chances of density gradients within the fully sintered material.

92

Cooling rates were held constant at about 10 °C/min (50 °F/min). A total of five specimens were sintered for each of the five different compositions.

3.1.5. FINISHING

The fully sintered samples were removed from the graphite die using a mechanical press and all graphite foil was stripped using a razorblade. The samples were then sent to PremaTech Advanced Ceramics (Worcester, MA), where four-point bend bars were machined. Resultant scraps from the machining process were ground flat using subsequently finer diamond grinding disks (Platinum Disk 0 through 4; Leco Corporation, St. Joseph, Michigan) for about 3 to 5 minutes per step at a disk rotation speed of 200 rpm. A mirror finish was then lapped using subsequently finer diamond pastes (Grade HS; Sun Diamond Marketing Group, Berkeley, California) at a disk rotation speed of 400 rpm on red felt polishing pads for the intermediate polishing steps of 30 μm and 15 μm (Leco Corporation, St. Joseph, Michigan) or nylon pads (Leco Corporation, St. Joseph, Michigan) for the fine polishing steps of 9 μm, 6 μm, 3 μm, 1 μm, ½ μm, and ¼ μm. A summary of the steps used for the grinding and lapping process, including the respective abrasive type and size, pad type, times held, and disk rotation speeds at each step may be seen in Table 3-5.

93

Table 3-5: Grinding and lapping processing steps.

| Abrasive Type | Abrasive Size | | Polishing Cloth | Time [min] | Disk Rotation Speed [rpm] |
	American Standard Grit	[μm]			
Platinum 0 Disk	60 – 120	250 – 130	—	3 to 5	200
Platinum 1 Disk	120 – 180	130 – 90		3 to 5	
Platinum 2 Disk	220 – 320	75 – 50		3 to 5	
Platinum 3 Disk	600	30		3 to 5	
Platinum 4 Disk	1,200	15		3 to 5	
Diamond Paste	600	30	Red Felt	5 to 15	400
	1,200	15		5 to 15	
	1,800	9	Nylon	5 to 15	
	3,250	6		5 to 15	
	8,000	3		5 to 15	
	14,000	1		5 to 15	
	60,000	½		5 to 15	
	100,000	¼		5 to 15	

3.2. MATERIAL CHARACTERIZATION

The steps that were taken in order to characterize each of the sintered ceramic specimens are listed in the sections below. These characterization techniques included density and porosity measurements, phase and contaminate analysis on pre- and post-sintered ceramic powders using x-ray diffraction analysis, and microstructural and fractography characterization using a scanning electron microscope.

94

3.2.1. DENSITY MEASUREMENTS

The densities of the fully sintered compacts were measured using Archimedes method. Standard geometrical density calculations were also calculated in order to have an estimated, ballpark figure, which could be used to roughly verify the results that were obtained from the Archimedes measurements. Percent relative densities, ρ_{th}, were found using the calculated theoretical densities of each composition, based on the amount and type of the respective particulate additions, as seen in Table 3-4.

The geometrical density calculations were completed by dividing the mass of each sample by the measured volume made with 0.01 mm (<0.001 in) resolution micrometers. This method was only used as an estimated figure because it has the potential for error based on specimen irregularities.

Archimedes method is a more accurate measurement of the specimen density, in which the density of the measuring fluid, ρ_{fluid}, is related to the ratio of the dry weight of the sample, W_{dry}, to the difference of the saturated weight, W_{sat}, and suspended weight in water, W_{sus}, as seen in Equation 3-1. It was assumed that the density of water was equivalent to 1 gm/cm^3 (0.036 lb$_m$/in^3). Five density measurements were made for each composition and the values were then averaged.

$$\rho = \frac{\rho_{fluid} \cdot W_{dry}}{W_{sat} - W_{sus}} \tag{3-1}$$

95

3.2.2. POROSITY

The total porosity present in each of the sintered samples was also calculated. The total porosity, P, can be found by relating the theoretical density, ρ_{th}, to the calculated density, ρ, as seen in Equation 3-2.

$$P = 100 \cdot \frac{\rho_{th} - \rho}{\rho_{th}} \qquad \textbf{(3-2)}$$

3.2.3. PHASE IDENTIFICATION

Phase identification of the fully sintered samples ceramic samples as well as the starting powders was conducted using x-ray diffraction (XRD) analysis in order to quantitatively identify the compounds.

All analysis was performed using a Co-Kα diffractometer (MiniFlex+ X-Ray Diffractometer; Rigaku/MSC Inc., The Woodlands, TX). Data was collected from 10° to 80°, at a scan speed of 1 s/step, and a step width of 0.01°/step. The resultant data was then characterized using computer software (Jade; Materials Data Inc., Livermore, CA).

XRD diffraction patterns were taken of the as-received boron carbide, silicon carbide, and titanium diboride powders as well as all of the ball-milled powders.

Analysis of the sintered samples was completed by grinding clean, non-graphite-coated samples into fine powder and then examining them in the XRD. Corn starch was used as a base layer if not enough ground powder was present, and was found to have little, or no affect on the final XRD pattern of the sample. One sintered sample per

96

composition was analyzed using this powder-XRD technique in order to verify that no new phases appeared in the sintered ceramic specimens.

3.2.4. MICROSTRUCTURAL CHARACTERIZATION

Characterization of the microstructures and fractured surfaces of each composition were examined using a scanning electron microscope (Hitachi S800; Hitachi High-Technologies Corporation, Pleasanton, CA) with backscatter detection.

3.2.4.1. Grain-Size

The average grain-size of the ceramic samples was found by observing the SEM images of the fractured specimens. A modified version of the line intercept method was used, and the grain-size, g, was determined by counting the number of times grain boundaries were intercepted with an arbitrary line, which is mathematically depicted in Equation 3-3, where L_T is the total length of the test line, P is the total number of grain boundary intersections, and M is the magnification level.

$$g = \frac{L_T}{PM} \tag{3-3}$$

Only rough estimations could be calculated because clear micrographs of the grain structure could not be obtained from the lapped specimens.

3.2.4.2. Fractography

Fractography analysis was completed on the fractured surfaces of the Chevron-Notched four-point bend bars. These bars were chosen over the flexure strength bend bars because the sharp cracktip that was machined into the bars before testing allows for a crack to easily and very clearly propagate all the way through the material. Therefore, the analysis of the failure modes and any given toughening mechanisms for each composition can be accurately visually determined. Fractured surfaces are often described as to whether a crack passes through or between grains, which is known as transgranular and intergranular, respectively.

In transgranular fracture, the fracture travels through the grain of the material and changes direction because of the lattice orientations within each grain. The crack will follow the edges of the lattices, rather than the actual grains themselves. In other words, when a crack reaches a new grain, it may have to find a new path or plane of atoms to travel along because it is less energy is required to change the crack direction than it is to rip through the entire grain. This principle can be summarized in terms of cracks choosing the path of least resistance.

In contrast, intergranular fracture involves a propagating crack that travels along the grain boundaries of the material, and not through the actual grains. Intergranular fracture usually occurs when the phase in the grain boundary is weak and brittle. The fracture changes direction in order to follow the path made by the ending of one grain and the beginning of another.

98

3.3. MECHANICAL PROPERTIES

The following sections provide an overview of the methods used to determine the various mechanical properties studied in this investigation, including the microhardness using Vickers microhardness indentation, the fracture toughness and flexure strength using four-point bend experiments, as well as the elastic modulus using the static technique.

3.3.1. VICKERS MICROHARDNESS

Vickers microhardness values were measured using a commercially available microindenter (Buehler MicroMet 2103; Buehler Ltd., Lake Bluff, IL) on scrap pieces of material that were left over from the machining of the four-point bend specimens. Each scrap specimen was ground and lapped in accordance to the procedure outlined in Section 3.1.5 of this manuscript in order to ensure that the surface was flat enough to guarantee that the indentation mark could be easily viewed. The specimen surfaces were cleaned before testing in order to ensure that they were free of any grease or film. Likewise, the indenter was cleaned prior to conducting each test by using a cotton swab soaked in methanol.

The specimens were fixed on the machine so that they could not rock or shift during testing. The surface of the specimen was situated in a plane normal to the axis of the indenter, and the angle of the indenter and specimen surface was within 2° of perpendicular. Greater amounts of tilting would produce nonuniform indentations and invalid test results. The indentation was rejected if there was excessive cracking from the

99

indentation tips and sides or the indentation was asymmetric. Likewise, the indentation was rejected if the indentation tip was placed in or on a large pore.

A testing load of 1 kg$_f$ (2.2 lb$_f$), or 9.81 N, was used for this research in accordance to ASTM Standard C 1327-03.[47] The rate of indenter motion prior to contact with the specimen was about 0.070 mm/s (0.003 in/s). The time of application of the full test load, or dwell time, was 15 s. After the indention was completed for this set amount of time, the indenter was raised carefully off the specimen to avoid any vibrational impact. A distance of at least five diagonal lengths between the centers of each of the indentations was allowed between each indent.

A total of two or five indentations were performed on a randomly selected portion of each ceramic composition. The Vickers hardness number, *HV*, was calculated from the resulting indentation size data using Equation 2-8.

3.3.2. FOUR-POINT BEND TESTS

All four-point bend testing was preformed on a MTS 810 Material Testing System (MTS Systems Corporation, Eden Prairie, MN). For these sets of experiments, a custom-made fully-articulating four-point bend fixture was used, as seen in Figure 3-2, having an outer span, *L*, of 19.00 ± 0.10 mm (0.748 ± 0.004 in) and an inner span of 10.00 ± 0.10mm (0.394 in ± 0.004). The fixture allows for full independent articulation, or pivoting, of all rollers about the specimen long axis to match the specimen surface. Cylindrical bearings were used to support and load the test specimens and were free to move. The bearings have a diameter of 2.00 mm (0.079 in). The inner bearings were successfully positioned to within 0.10 mm (0.004 in) with respect to the outer bearings.

The inner and outer bearings were parallel to each other to within 0.015 mm (0.006 in) over their entire respective length. The fixture and all bearings were manufactured from silicon carbide.
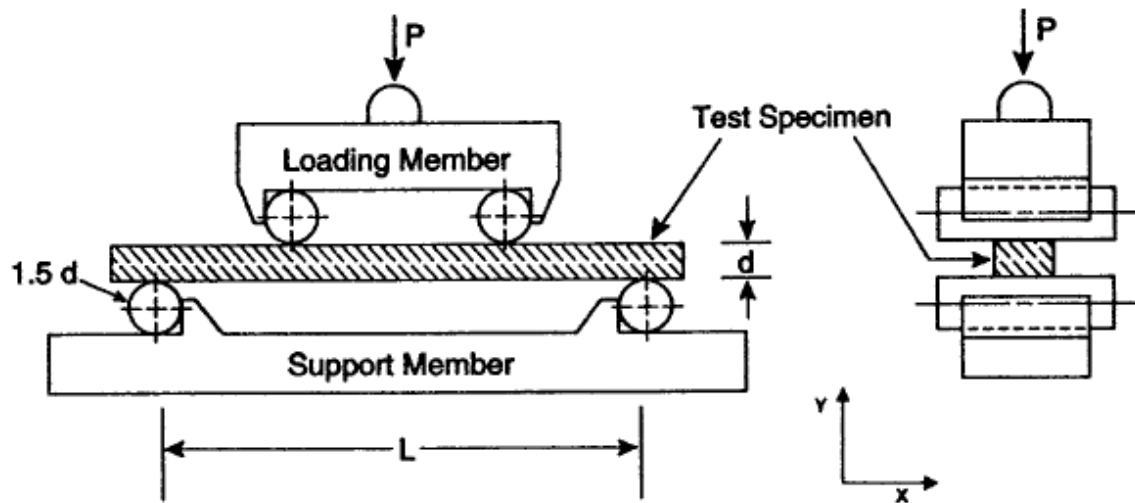

Figure 3-2: Schematic of a semiarticulated four-point fixture suitable for flat and parallel specimens.

The samples were cold-loaded into the four-point bend fixture using double-sided tape. The top piece of the fixture was aligned and centered with the bottom using a jig, and the bend bar samples where centered both vertically and horizontally. The fixture was then loaded into the bottom portion of the machine and the top actuator was lowered to where it was almost touching the fixture. From there, the four-point bend testing software (TestStar II Station Manager; MTS Systems Corporation, Eden Prairie, MN) was used to load each bar until failure and record apparent load and crosshead displacement measurements.

101

3.3.2.1. Fracture Toughness

Chevron-Notched fracture toughness four-point bend specimens were machined from the 51 mm (2 in) diameter specimens to 3.00 mm x 4.00 mm x ≥ 25.0 mm (0.118 in x 0.157 in x ≥ 0.984 in) rectangular bars having a 60° 2.6 mm (0.102 in) deep notch machined into the middle of the bar, in accordance to a modified version of Type D bars of ASTM Standard C 1421-01b (2007).[50] A schematic view of the bars may be seen in Figure 3-3. Machining was completed by PremaTech Advanced Ceramics (Worcester, Massachusetts). Cross-sectional dimensional tolerances were ± 0.13 mm (0.005 in) for the bars and the two end faces were not precision machined. No edge treatments of the longitudinal edges were completed on the compression face.

All grinding was parallel to the long axis of the specimens and in the presence of an ample supply of filtered coolant. No Blanchard or rotary grinding was used. The four long faces where machined according to the previously mentioned ASTM Standard using 150-grit, 240- to 320-grit, and 400- to 600-grit diamond wheels, successively, at a wheel speed of at least 25 m/s (~1000 in/s).

The chevron notch was cut using a 320-grit diamond wheel. The notch thickness, *t*, was cut so that it was V-shaped and positioned so that it was less than 0.25 mm (0.010 in) away from any point of intersection with the surface. The notch was less than 0.15 mm (0.006 in) thick at its root radius. The planes of notches cut from each side of the test specimen met within 1.2 mm (0.047 in), while the tip of the notch was on center within 0.06 mm (0.002 in).

After machining, all bars were examined for cracks under a 30-50 X stereo binocular microscope, and the dimensions of each bar was measured using micrometers

having a resolution of 0.01 mm (<0.001 in). The tip of the notch was examined in order to ensure that it was on center. Any bars found to not meet any of the outlined specifications were discarded. A total of three to four of these types of bend bars per material composition were tested.
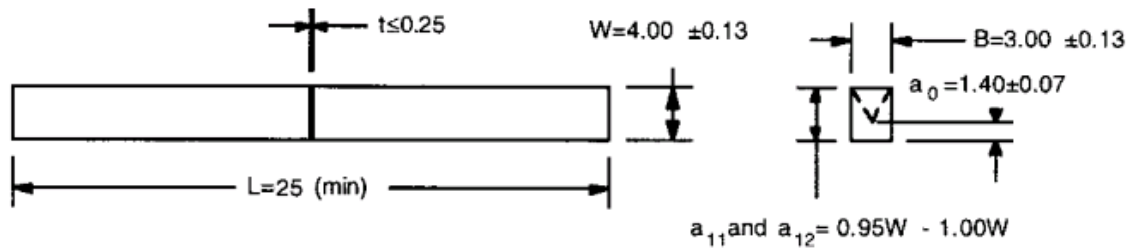

Figure 3-3: ASTM Standard C 1421-01b (2007) modified Type D four-point bend Chevron-Notched specimen bar.

Fracture toughness four-point bend tests were completed at crosshead a crosshead speed of 0.20 mm/min, which corresponds to an approximate strain rate of about $5E^{-4}$ s^{-1}. The apparent time to fracture was measured to be about 30 s. All testing was done in air at ambient temperatures, and the fracture toughness, K_{Ic}, was computed from the load data using Equation 2-10 and Equation 2-11.

3.3.2.2. Flexure Strength

Flexure strength four-point bend specimens were machined from the 51 mm (2 in) diameter specimens to 1.5 mm x 2.0 mm x ≥ 25.0 mm (0.059 in x 0.079 in x ≥ 0.984 in) rectangular bars, in accordance to Type A bars of ASTM Standard C 1211-02 (2008).[51] A schematic view of the bars may be seen in Figure 3-4. Machining was completed by PremaTech Advanced Ceramics (Worcester, Massachusetts). Cross-sectional

103

dimensional tolerances were within ± 0.05 mm (0.002 in) for the bars, while the parallelism tolerances on the four longitudinal faces are ± 0.03 mm (0.001 in). The two end faces were not precision machined. All grinding was parallel to the long axis of the specimens and no Blanchard or rotary grinding was used. The four long faces where machined according to the previously mentioned ASTM Standard using 150 grit, 240 to 320 grit, and 400 to 600 grit diamond wheels successively at a wheel speed of no less than 25 m/s (~1000 in/s). The four long edges where chamfered at 45° a distance of 0.12 ± 0.03 mm (0.005 in ± 0.001 mm) from each side. The edge finish was completed using the same steps as the long surfaces. After machining, all bars were examined for cracks under a 50 X stereo binocular microscope, and the dimensions of each bar was measured using micrometers having a resolution of 0.01 mm (<0.001 in). Any bars found to not meet any of the outlined specifications were discarded. A total of seven to nine of these types of bend bars per material composition were tested.
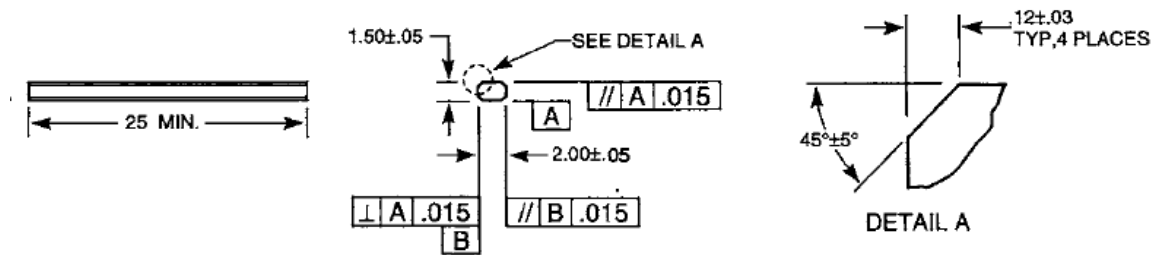

Figure 3-4: ASTM Standard C 1211-02 (2008) Type A four-point bend specimen bar.

Flexure strength four-point bend tests were completed at crosshead a crosshead speed of 0.20 mm/min, which corresponds to an approximate strain rate of about $4.5E^{-4}$

s^{-1}. The apparent time to fracture was measured to be about 40 s. All testing was done in air at ambient temperatures, and the flexure strength, σ_{fb}, was computed from the load data using Equation 2-12.

3.3.2.3. Elastic Modulus

The elastic modulus of the fully sintered ceramic samples was measured using the static measurement technique, in which a single strain gage (EA-06-015DJ-120/LE; Vishay Intertechnology Incorporated, Malvern, Pennsylvania) having a gage factor of 2.07 ± 0.041 and a grid resistance of 120 ± 0.72 Ω was attached to the center of the tensile face of a flexure strength four-point bed bend bars. The gage was attached in a direction that was parallel to the length of the bar by first cleaning it with acetone and then applying the first of a two-part epoxy to the back of the gage itself. Once the centered-location of the gage and its parallelism with the length of the bar was verified, a small drop of the second part of the epoxy was applied and the gage was then gently placed on top it. Light pressure was then applied for about 2 minutes in order to ensure that the gage made a tight bond.

Once the gage was attached to the bend bar, its two leads were attached to a strain indicator (Vishay 3800 Wide Range Strain Indicator; Vishay Intertechnology Incorporated, Malvern, Pennsylvania). The gage factor was set to 2.05, which was within limits given by the gage manufacturer. Before the actual bend bar test was conducted, the gage reading was balanced to zero using the balance knob on the indicator apparatus.

A total of two of these bend bars with strain gages attached were tested. The resultant stress and strain data were plotted, and the slope of the corresponding linear best-fit line was evaluated and set equal to the elastic modulus.

CHAPTER 4: DATA ANALYSIS

The following sections present the data that was obtained during this investigation, and includes summaries of the statistical methods that were used for analytical purposes, as well as reviews of the results from the powder processing, material characterization, and mechanical properties methodologies.

Please note that it has become standard practice to present much of the data associated with ceramic materials in the International System of Units and, therefore, the bulk of the data presented henceforth will be as well. However, English units will still sometimes be provided along side their respective metric counterpart in order to maintain consistency with the previous sections of this document.

4.1. STATISTICAL ANALYSIS

A statistical analysis was preformed on all numerical data in order to summarize and describe the data collections. In this way, a fair comparison could be conducted between each of the different sets of data for each material composition. The statistical methods that were used for this investigation included the average, standard deviation, coefficient of variation, standard error of the mean, and a confidence interval for the mean for each respective data set, and are outlined below.

107

4.1.1. AVERAGE AND STANDARD DEVIATION

The average value, $\bar{x}$, for a data set containing n values was calculated by dividing the total sum of the data set by the number of samples within that set, as seen in Equation 4-1.

$$\bar{x} = \frac{1}{n} \sum_{i=1}^{n} x_i \qquad \textbf{(4-1)}$$

The standard deviation, $\sigma_{\bar{x}}$, was calculated by summing the square of the differences between each data point and its set respective average and then multiplying it by the reciprocal of the number of data points within the set subtracted by 1, as seen in Equation 4-2. With this in mind, the larger the standard deviation value for a given data set, the larger variability within that set.

$$\sigma_{\bar{x}} = \sqrt{\frac{1}{n-1} \sum_{i=1}^{n} \left(x_i - \bar{x} \right)^2} \qquad \textbf{(4-2)}$$

The $n-1$ factor in Equation 4-2 is used because each respective data set only represents a portion of the overall population. In other words, this term is used because the data that was observed from each ceramic composition was not conducted on every portion of every fully sintered specimen. If the later statement had been the case, in other words if

every segment of every specimen had been analyzed, then the factor would simply be n, rather than $n-1$, because the entire population would have been represented.

4.1.2. COEFFICIENT OF VARIATION

The coefficient of variation, C_v, is a normalized percentage measure of the amount of variation within a given data set. This is a useful statistic because it allows for the determination of the size of variation relative to the size of the observed values, regardless of their units of measure. This unit independence allows for multiple sets of data for differing properties to be compared and also allows for the standard deviation of a data set to be put into context when compared to its respective average. The coefficient of variation is calculated by dividing the standard deviation by the mean and multiplying by 100%, as seen in Equation 4-3.

$$C_v = 100 \frac{\sigma_{\bar{x}}}{\bar{x}} \tag{4-3}$$

As seen in Equation 4-3, the smaller the coefficient of variation value, the more consistent the data is within a set.

4.1.3. STANDARD ERROR OF THE MEAN

The standard error of the mean, $SE_{\bar{x}}$, is a measure of the standard deviation of the average of the sample data when compared to the average of the total population. The

109

standard error of the mean is calculated by dividing the standard deviation by the total number of data points within the set, as seen in Equation 4-4.

$$SE_{\bar{x}} = \frac{\sigma_{\bar{x}}}{\sqrt{n}}$$ **(4-4)**

Even though the standard error of the mean and the standard deviation of a given data set are related, they represent two different types of information. The standard deviation is a measure of the distribution within individual data points around the average of a data set, while the standard error of the mean represents how precise the estimate of the average for the set truly is. With this in mind, the standard error of the mean is a useful statistic because it details how well a given average for a data set represents the average of the overall population in which the data set was drawn.

4.1.4. CONFIDENCE INTERVAL FOR THE MEAN

The confidence interval for the mean, *CI*, is the range of values that is likely to enclose the true value of the average for a given data set for some given desired precision. In other words, the confidence interval is a range of values for a given average of a data set that is constructed so that the range has a specified probability of including the true average value of the set. This statistic is important because it provides a range of values that is likely to contain the overall average of the population.

The confidence interval for the mean can be calculated by summing the average value for a data set to the product of the standard error of the mean and a confidence

110

level, z. A given confidence level, say 95%, means that the intervals obtained using numerous data sets taken from the same population on numerous occasions will bracket the true average of the entire population in a percentage amount that is equivalent to that level, or the true average value of the population will fall within a certain range 95% of the time for multiple separate data sets. For a 95% confidence level the value of z is equivalent to 1.96, as seen in Equation 4-5.

$$CI_{95} = \bar{x} \pm 1.96 SE_{\bar{x}} \qquad \textbf{(4-5)}$$

As seen in Equation 4-5, the confidence interval of the mean decreases as the variation between the individual points within a data set decreases.

4.2. POWDER PROCESSING

The resultant data from the powder processing methodology that was followed in order to manufacture the boron carbide-based ceramic specimens from the various starting powder constituents is outlined in the following sections. Information regarding the analysis of the raw ceramic powders as well as the blended powders is presented. An overview of the results from the sintering techniques that were used is also reviewed.

4.2.1. RAW CERAMIC POWDERS

A total of three different types of raw ceramic powders were used for this research, including boron carbide (Grade HS; H.C. Starck, Berlin, Germany), alpha

111

silicon carbide (Grade GC #30000; Fujimi Corporation, Kiyosu, Japan), and titanium diboride (Grade HCT-30; GE Advanced Ceramics, Cleveland, Ohio). An overview of the manufacturer supplied average particle sizes for the three starting powders may be seen below in Table 4-1.

Table 4-1: Manufacturer supplied particle size distributions for the B_4C, SiC, and TiB_2 powders.

Material	Particle Size
Boron Carbide	90 % of particles $\leq$ 3.41 μm
	50 % of particles $\leq$ 0.89 μm
	25 % of particles $\leq$ 0.24 μm
Silicon Carbide	95 % of particles $\leq$ 0.58 μm
	50 % of particles $\leq$ 0.29 μm
	25 % of particles $\leq$ 0.20 μm
Titanium Diboride	90 % of particles $\leq$ 30.5 μm
	50 % of particles $\leq$ 16.4 μm
	25 % of particles $\leq$ 11.2 μm

Scanning electron microscopy (SEM) imaging was conducted on the three powders in order to visually verify these supplied size distributions and to observe the morphology of the powders. The resulting images for the B_4C powder may be seen below in Figure 4-1, while Figure 4-2 represents the α-SiC powder, and Figure 4-3 corresponds to the TiB_2 powder.
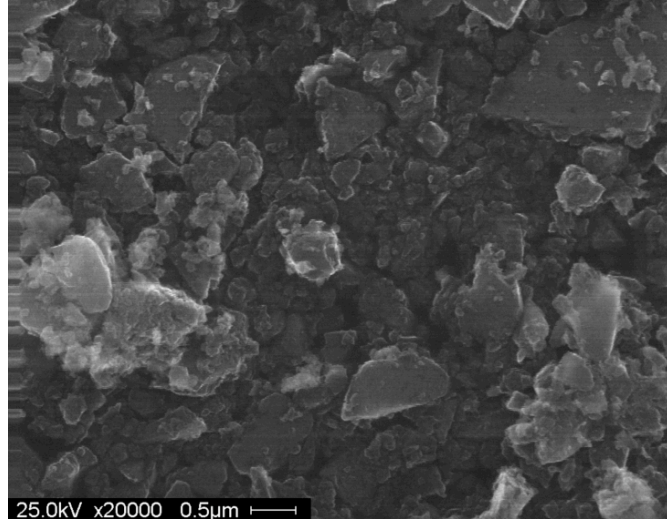
112

Figure 4-1: SEM image of as-received B$_4$C powder (Grade HS; H.C. Starck).
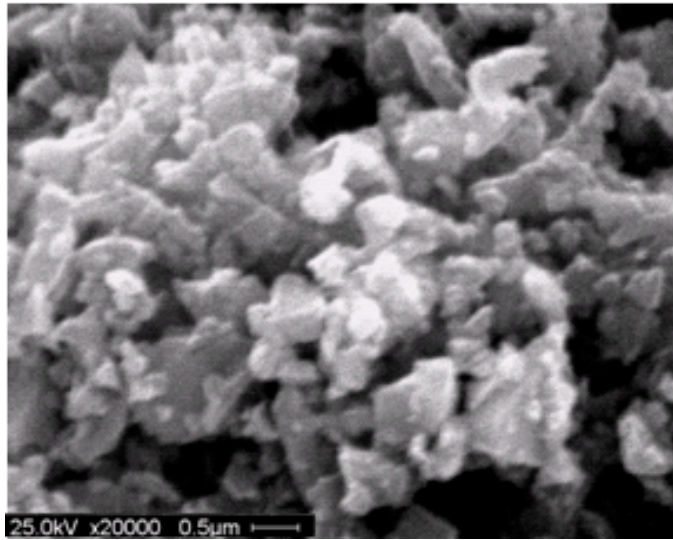

Figure 4-2: SEM image of as-received α-SiC powder (Grade GC #30000; Fujimi Corporation).
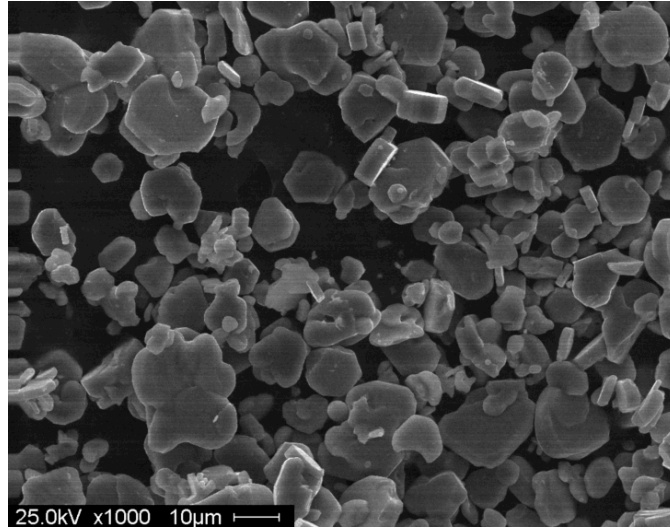
113

Figure 4-3: SEM image of as-received TiB_2 powder (Grade HCT-30; GE Advanced Ceramics).

As seen in these figures, there is a fairly large distribution of particle sizes present within the starting powders that, for the most part, corresponds to the supplied particle size distributions given in Table 4-1. The morphology of the powder particles, however, appears to be much more evenly distributed. The form seems to be fairly blocky with a few rectangular particles being scattered throughout. The edges of the powder particles seem to be somewhat smooth while the corners of the particles are rather jagged. There are, however, some small indentations along the length of the particles, but these appear to be small when compared to the overall size of the particles themselves. The texture of all of the particles seems to be relatively smooth.

4.2.2. POWDER BLENDING

As before, SEM imaging was conducted on the four composite powder mixtures, and the resultant images for B_4C + 10 vol% α-SiC are presented in Figure 4-4 and Figure

www.manaraa.com

4-5, while the images for B$_4$C + 20 vol% α-SiC are presented in Figure 4-6 and Figure 4-7. Likewise, the resultant images for B$_4$C + 10 vol% TiB$_2$ are presented in Figure 4-8 and Figure 4-9, while the images for B$_4$C + 20 vol% TiB$_2$ are presented in Figure 4-10 and Figure 4-11.

As seen in these images, the overall size distribution of the ball-milled composite powders is greatly reduced, which can be directly attributed to the milling process. The ZrO$_2$ tumbling media that were contained along with the powder constituents within the rotating cylinders produced a grinding action by impacting the particles on their surfaces, which caused shearing when a given powder particle was seized between two surfaces that were moving at different velocities. Shear and tensile stresses were produced by the in-line compressive loads that were caused by the tumbling of the heavier milling media onto the much lighter powder particles, while attrition was produced by the frictional stresses associated with the sliding and rubbing of powder particles between the hard surfaces of the ZrO$_2$ media.

This size reduction is most prevalent in the powders containing TiB$_2$ that are seen in Figure 4-9 through Figure 4-11. In these figures, the TiB$_2$ particles appear as larger, block-like shapes that are spread fairly homogeneously throughout the smaller B$_4$C particles. Even though the size relation between the B$_4$C and TiB$_2$ is still fairly significant, the overall size of the TiB$_2$ constituents has been considerably reduced, which can be easily seen when a comparison is made of the aforementioned images and the image of the pure TiB$_2$ powder.
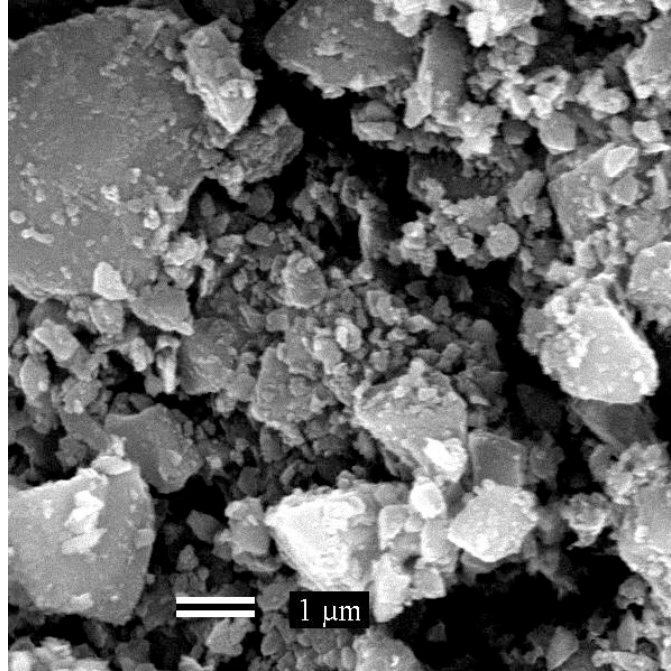
Figure 4-4: SEM image of the ball-milled B$_4$C + 10 vol% α-SiC powder (1 μm scale).
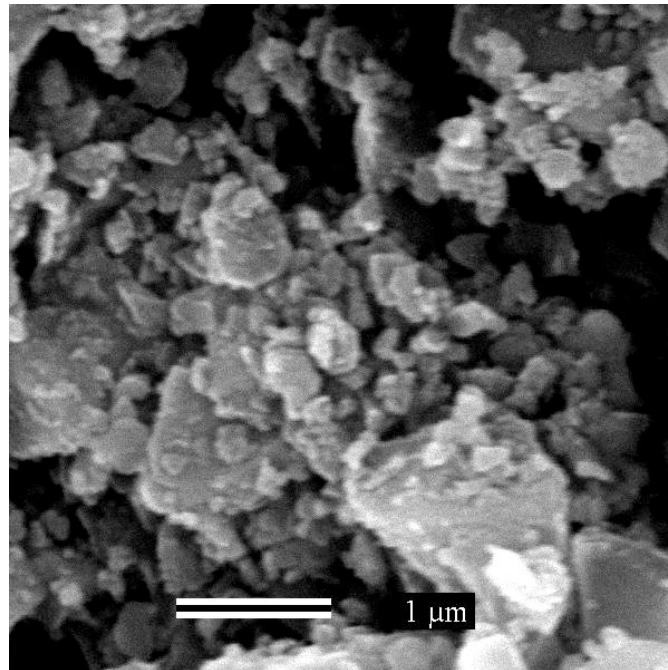
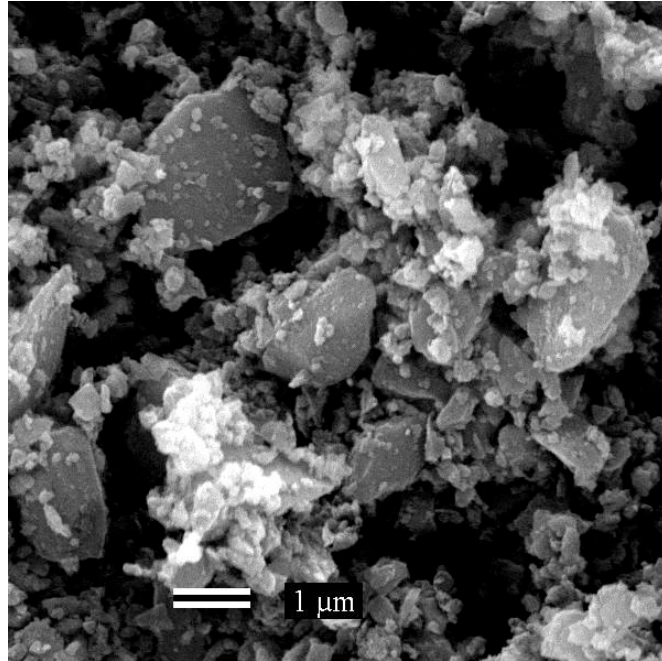**Figure 4-5:** SEM image of the ball-milled B$_4$C + 10 vol% α-SiC powder (1/2 μm scale).

116

Figure 4-6: SEM image of the ball-milled B$_4$C + 20 vol% α-SiC powder (1 μm scale).

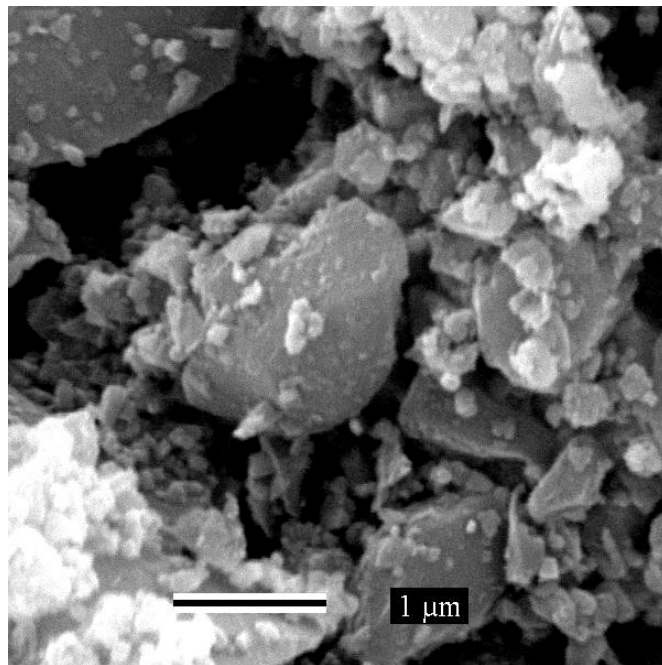**Figure 4-7:** SEM image of the ball-milled B$_4$C + 20 vol% α-SiC powder (1/2 μm scale).

117
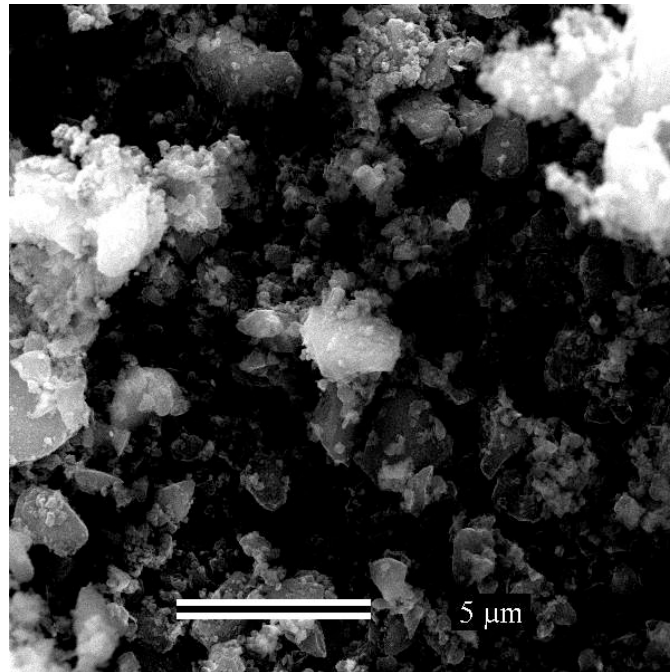
Figure 4-8: SEM image of the ball-milled B_4C + 10 vol% TiB_2 powder (5 μm scale).
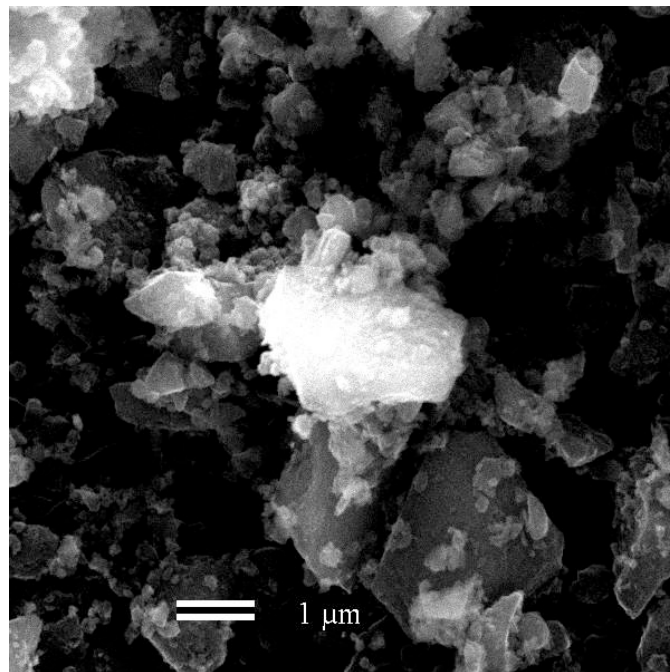
Figure 4-9: SEM image of the ball-milled B_4C + 10 vol% TiB_2 powder (1 μm scale).

118

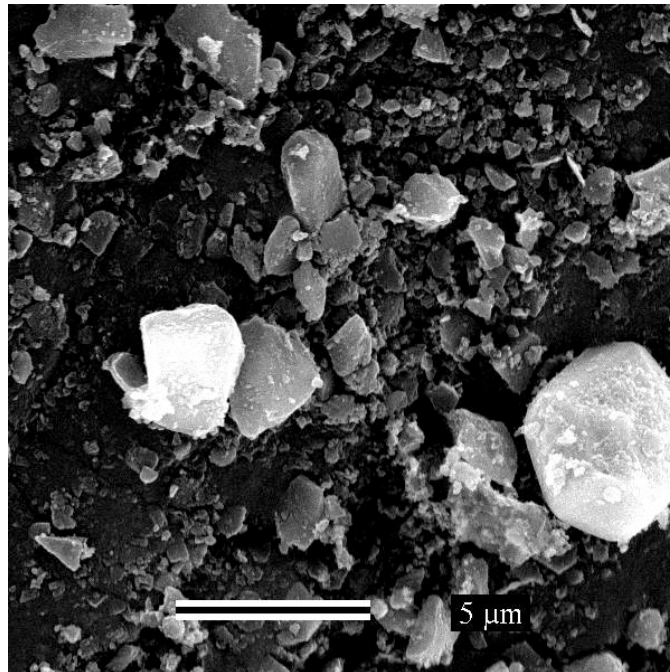**Figure 4-10**: SEM image of the ball-milled B_4C + 20 vol% TiB_2 powder (5 μm scale).
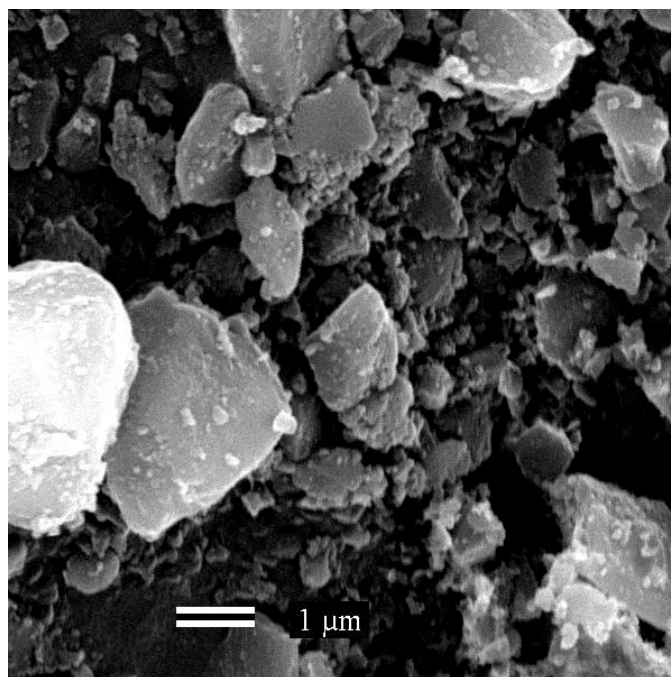

Figure 4-11: SEM image of the ball-milled B_4C + 20 vol% TiB_2 powder (1 μm scale).

119

The distribution of the sizes present within all of the blended powders appears to be similar to that of the starting powders, but the absolute size of the powders is greatly decreased. The morphology of the powder particles likewise appears to be similar to that of the starting constituents.

4.2.3. SINTERING

A total of five specimens were sintered using the $P^2C^®$ method for each of the five different B_4C-based compositions. The maximum sintering temperature and time at that temperature that were required to produce fully dense specimens varied somewhat for the different compositions, and this data may be seen below in Table 4-2. Because fully dense samples were the main goal of the powder processing methodology, the maximum consolidation temperatures and the times at these temperatures were optimized for each composition in order to ensure maximum density of the specimens.

The small observed temperature differences between the given compositions were because of the varying constituents within the powder compacts, which plays a major role on the overall melting point of the composition. A higher inherent melting point of a material results in a higher required maximum sintering temperature. This is because sintering involves the heating of a powder compact to between about 70% and 90% of its absolute melting point in order to get high diffusion rates along the powder boundaries. With this in mind, the melting point of pure boron carbide is 2350 °C, while SiC is 2730 °C, and TiB_2 is about 3225 °C. Therefore, it is of no surprise the composition containing the most TiB_2 required the highest maximum sintering temperature and time, and that

120

almost all of the composite ceramics required higher maximum sintering temperatures in order to achieve maximum density.

Table 4-2: Optimum sintering temperature and time for the B_4C-based compositions.

Composition	Maximum Sintering Temperature [°C]	Time at Temperature [min]
B_4C	1750	10
B_4C + 10 vol% α-SiC	1750	10
B_4C + 20 vol% α-SiC	1800	15
B_4C + 10 vol% TiB_2	1800	15
B_4C + 20 vol% TiB_2	1850	20

4.3. MATERIAL CHARACTERIZATION

The information that was obtained form the steps taken to characterize each of the sintered, fully dense ceramic specimens is listed in the sections below, and includes data pertaining to the density and porosity measurements, phase analysis on pre- and post-sintered ceramic powders, and microstructural characterization.

4.3.1. DENSITY AND POROSITY

The densities of the fully sintered compacts were measured using Archimedes method through the use of Equation 3-1. Percent relative densities were found using the calculated theoretical densities of each composition, which was based on the amount and type of the respective particulate additions. Likewise, the total porosity present in each of the sintered samples was found using the calculated relative density data along with

121

Equation 3-2. A summary of the average values for each of the sintered specimens per composition may be seen below in Table 4-3.

Table 4-3: Resultant relative densities and porosity calculations for the B_4C-based compositions.

Composition	Theoretical Density [g/cm^3]	Average Calculated Density [g/cm^3]	Average Percent Density [%]	Average Porosity [%] [min]
B_4C	2.52	2.51	99.44%	0.56%
B_4C + 10 vol% α-SiC	2.59	2.58	99.50%	0.50%
B_4C + 20 vol% α-SiC	2.66	2.64	99.32%	0.68%
B_4C + 10 vol% TiB_2	2.72	2.70	99.12%	0.88%
B_4C + 20 vol% TiB_2	2.92	2.90	99.45%	0.55%

As seen in this table, the ceramic specimens were sintered to full density, meaning the calculated density was at least 99% of the theoretical value. With this in mind, the average porosity in each specimen was kept to a minimum because porosity is directly related to the specimen density.

A statistical analysis was performed on the calculated density values that were measured for each of the sintered specimens, and the results may be seen below in Table 4-4. The porosity was not analyzed because it is dependent upon the calculated density values and an ensuing statistical analysis would simply result in repeated data. Because discontinuities within a given ceramic specimen, such as porosity, promote macroscopic cracking and thus contribute to the brittleness of the material, only fully dense sintered samples (≥99% theoretical) were chosen for this research. Therefore, the statistical data

122

of the density values is very precise because of the selective nature that was undertaken in choosing ceramic samples upon which to conduct testing. This fact can be justified by the small values for the standard deviation and the resulting coefficient of variation values.

Table 4-4: Statistical analysis of density measurements.

Composition	n	$\bar{x}$	$\acute{o}_{\bar{x}}$	C_v
B_4C	5	2.506	0.005	0.22%
B_4C + 10 vol% α-SiC	5	2.576	0.005	0.20%
B_4C + 20 vol% α-SiC	5	2.640	0.007	0.27%
B_4C + 10 vol% TiB_2	5	2.695	0.005	0.17%
B_4C + 20 vol% TiB_2	5	2.902	0.008	0.29%

4.3.2. PHASE IDENTIFICATION

Powder x-ray diffraction (XRD) analysis was conducted on the raw ceramic powders and on the pre- and post-sintered ceramic compositions in order to quantitatively identify the chemical compounds that were present.

4.3.2.1. Raw Ceramic Powder

The resulting plots of the arbitrary, unit-less intensity values versus the corresponding diffraction angle may be seen in Figure 4-12 for the pure B_4C powder, Figure 4-13 for the α-SiC powder, and Figure 4-14 for the TiB_2 powder. As seen in Figure 4-12, nearly all of the peaks that are present in the XRD patterns correspond to boron carbide. However, a small intensity, somewhat broad peak centered at about 31

123

degrees corresponds to carbon instead of B$_4$C. This excess carbon is more than likely caused by free graphite, which is a by-product of the powder synthesis process used to manufacture the material. According to the manufacturer material data, as much as 1 to 2 wt% of free graphite can be present within a given powder sample, which more than likely corresponds to this small peak in the XRD pattern.

The peaks in the XRD pattern for the α-SiC powder that is seen in Figure 4-13 corresponds well to the pattern of pure 6H-SiC. Therefore, it was assumed that the alpha SiC powder that was used for this research was of the 6H polytype. Likewise, the XRD pattern did not show much excess carbon or any other types of contaminates.

The XRD pattern of the TiB$_2$ powder, which is seen in Figure 4-14, follows that of pure TiB$_2$ extremely well. No contaminates or free carbon were detected within the resultant XRD pattern.
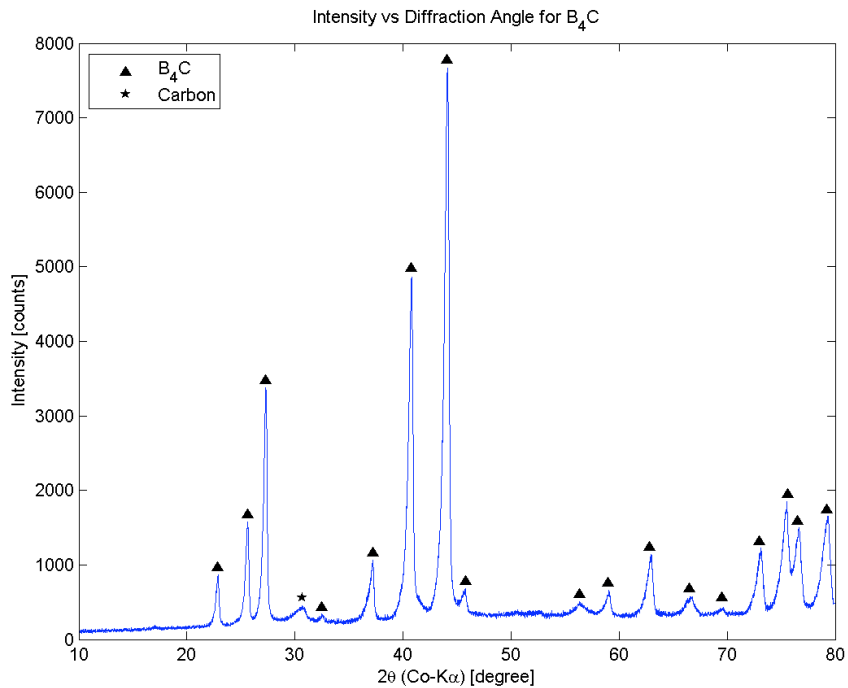

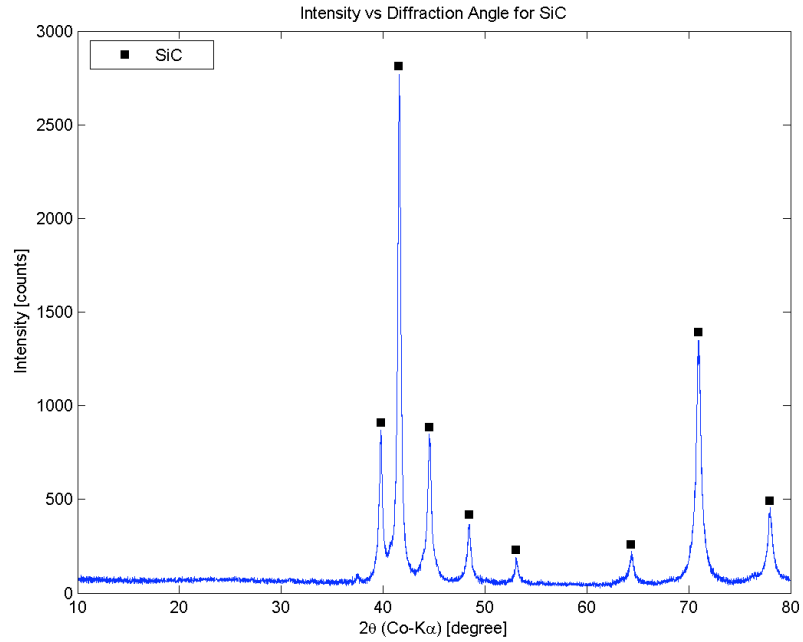**Figure 4-12:** XRD pattern for the pure B$_4$C powder.

124

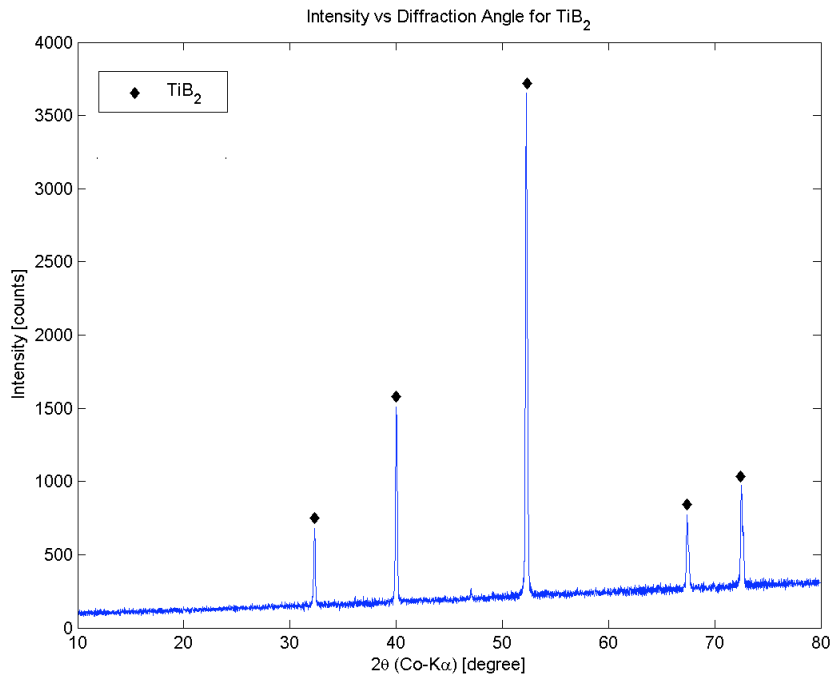**Figure 4-13:** XRD pattern for the pure α-SiC powder.

Figure 4-14: XRD pattern for the pure TiB₂ powder.

125

4.3.2.2. Blended Powder

XRD analysis was also conducted on the sintered, fully dense pure B_4C ceramic as well as on the four fully dense composites. In order to conduct a phase analysis, the results from the powder XRD diffraction patterns of the fully dense samples were compared to the patterns of the ball-milled, pre-sintered powders. Figure 4-15 represents a comparison of the diffraction patterns for the pure B_4C ceramic, while the patterns for B_4C + 10 vol% α-SiC and B_4C + 20 vol% α-SiC materials are presented in Figure 4-16. Likewise, the XRD patterns for the B_4C + 10 vol% TiB_2 and B_4C + 20 vol% TiB_2 materials are presented in Figure 4-17.
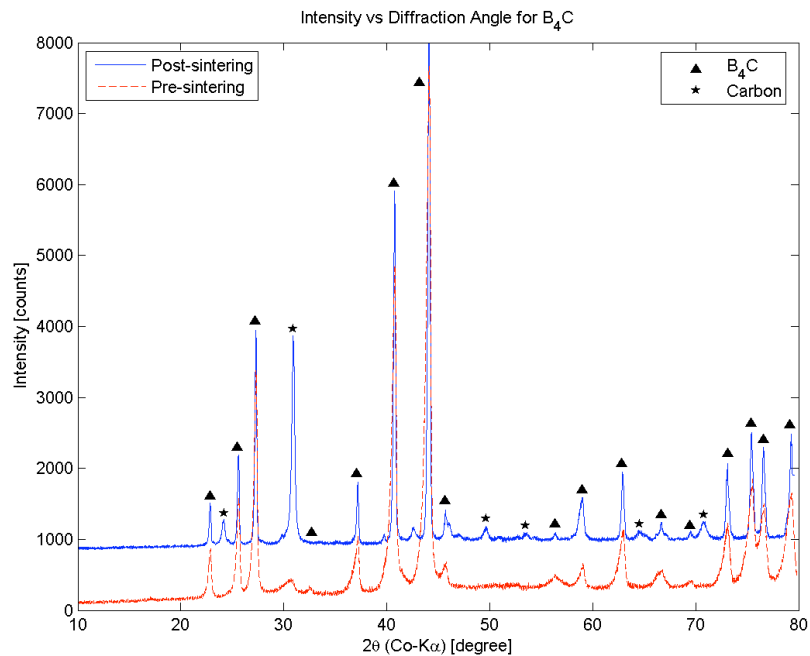

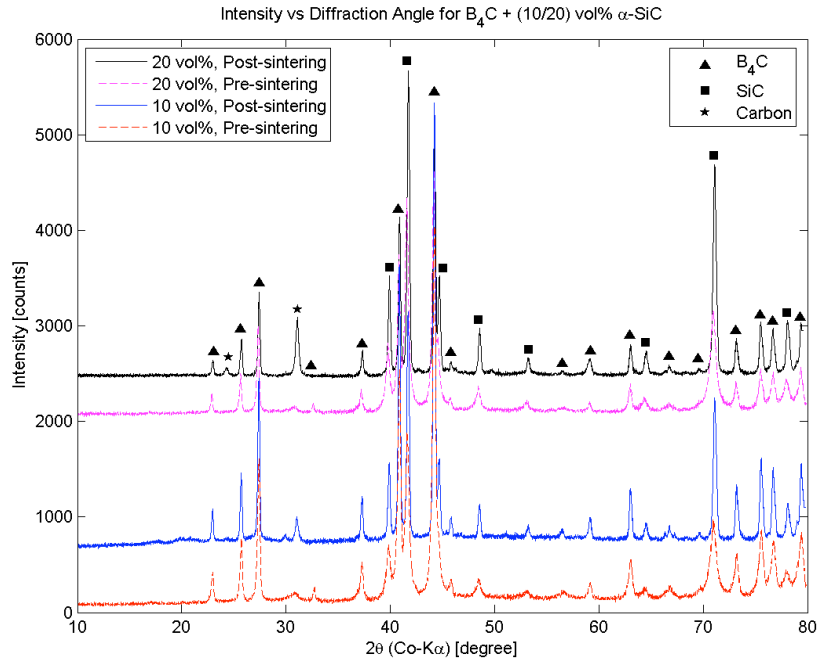**Figure 4-15:** XRD pattern of pre- and post-sintered B_4C powder.

126

Figure 4-16: XRD pattern of pre- and post-B_4C + (10/20) vol% α-SiC powder.
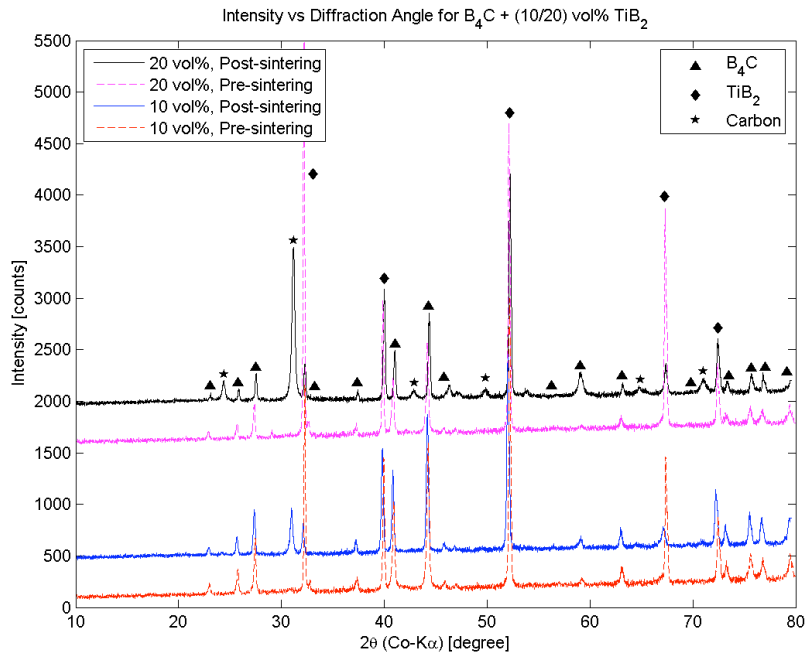

Figure 4-17: XRD pattern of pre- and post-B_4C + (10/20) vol% TiB_2 powder.

127

As seen in these figures, nearly all of the peaks for the post-sintered samples correspond well to the peaks that are present in the pre-sintered powder. Therefore, it is verified that no new phases were created throughout the powder processing steps and the constituents had very little, or no, chemical interactions with the boron carbide matrix.

Small traces of carbon, however, were identified in the XRD pattern of some, but not all, of the sintered samples. These peaks were almost entirely related to 2H-graphite, and were not present in the blended, unstinered powder. The most logical explanation for these carbon inclusions is that some amount of graphite foil remained on the fully dense, sintered sample before it was ground into powder. This idea is sensible because graphite foil was used to encompass the unsintered powder compact within the graphite die during the sintering process. Carbon, or graphite, diffusion could have also taken place during sintering, which would likewise account for peaks associated with carbon being represented in the XRD pattern of the sintered specimen. If carbon diffusion was the only source of the carbon peaks, however, graphite would more than likely be present in the XRD patterns of all the sintered samples, and not just a few. The corn starch that was used as a base layer for some of the sintered powder XRD samples was also considered to be a potential explanation for these peaks, but an XRD analysis of the pure substance showed that it does not in any way correspond to the peaks present in the patterns of the B_4C ceramic compositions.

It should also be noted that no zirconium- or polyethylene-related peaks were identified in the XRD patterns of the ball-milled powders. This is important because ZrO_2 milling media were used in polyethylene bottles during the blending process, and a lack of peaks associated with these materials signifies that no major amounts of

128

impurities were introduced to the powders during the milling process. The lack of peaks, however, does not signify that no contaminates were introduced simply because the resolution of the XRD machine that was used cannot identify compounds in relatively small amounts.

4.3.3. MICROSTRUCTURE AND FRACTOGRAPHY

Scanning electron microscopy (SEM) imaging was conducted on the fracture surfaces of selected Chevron-notched four-point bend specimens for each fully dense composition in order to determine the microstructure and the modes of fracture. The resulting images for the pure B_4C ceramic may be seen in Figure 4-18 and Figure 4-19. Likewise, the images for B_4C + 10 vol% α-SiC are presented in Figure 4-20 and Figure 4-21, while B_4C + 20 vol% α-SiC is in Figure 4-22 and Figure 4-23; the images for B_4C + 10 vol% TiB_2 are in Figure 4-24 and Figure 4-25, and B_4C + 20 vol% TiB_2 are presented in Figure 4-26 and Figure 4-27.

129
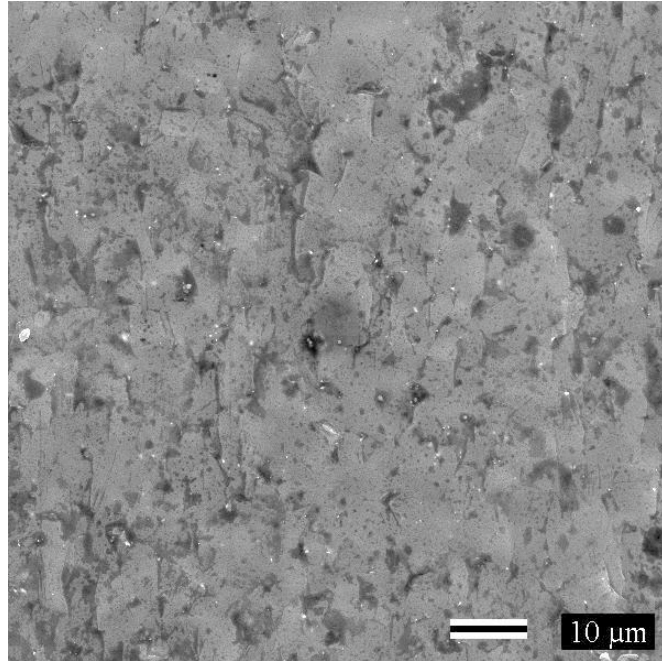
Figure 4-18: Fractured surface of B$_4$C (10 μm scale).
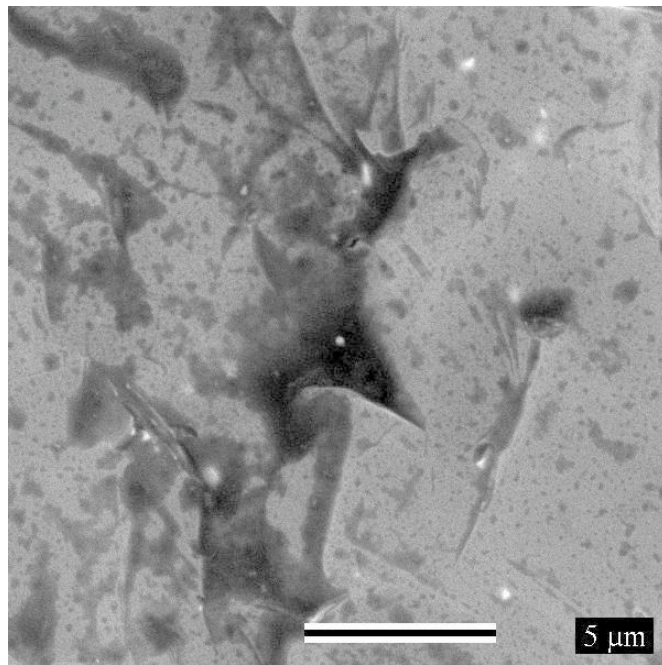
Figure 4-19: Fractured surface of B$_4$C (5 μm scale).

130
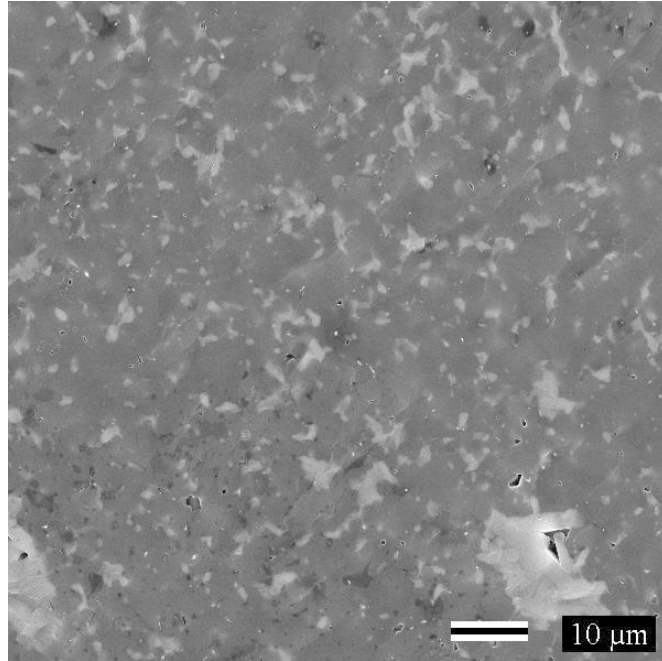
Figure 4-20: Fractured surface of B_4C + 10 vol% SiC (10 μm scale).
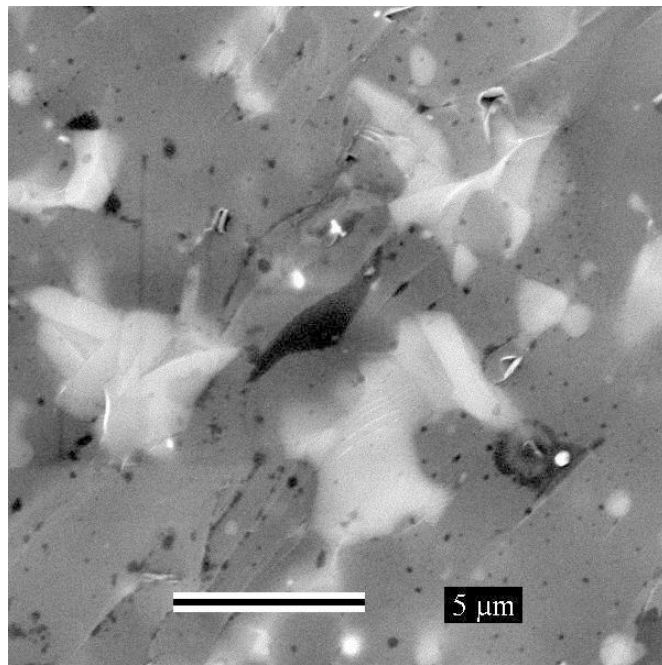
Figure 4-21: Fractured surface of B_4C + 10 vol% SiC (5 μm scale).

131
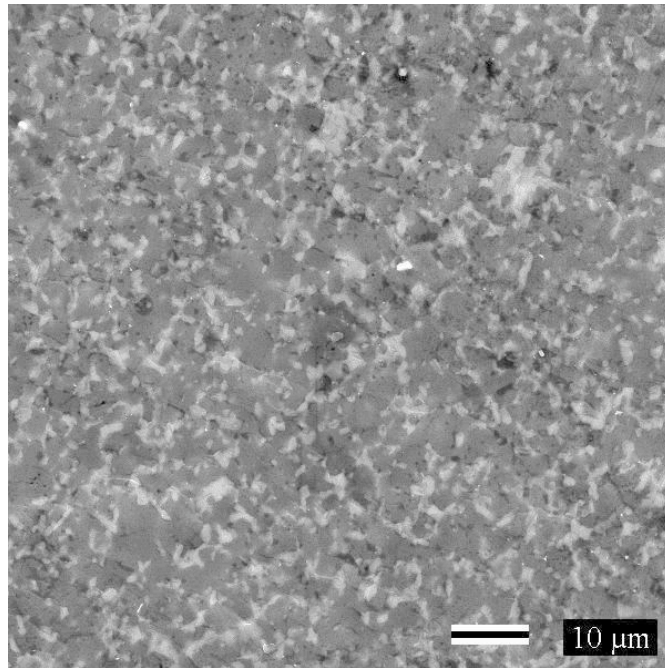
Figure 4-22: Fractured surface of B$_4$C + 20 vol% SiC (10 μm scale).

Figure 4-23: Fractured surface of B$_4$C + 20 vol% SiC (5 μm scale).

132
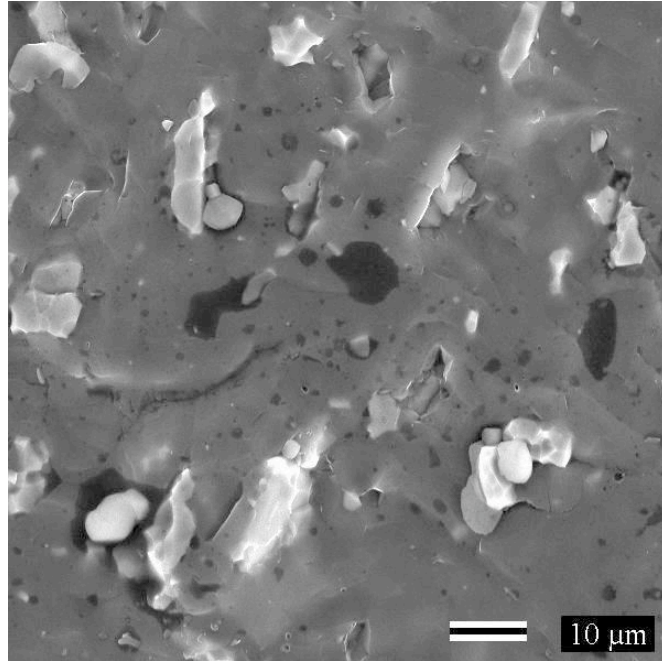
Figure 4-24: Fractured surface of B$_4$C + 10 vol% TiB$_2$ (10 μm scale).
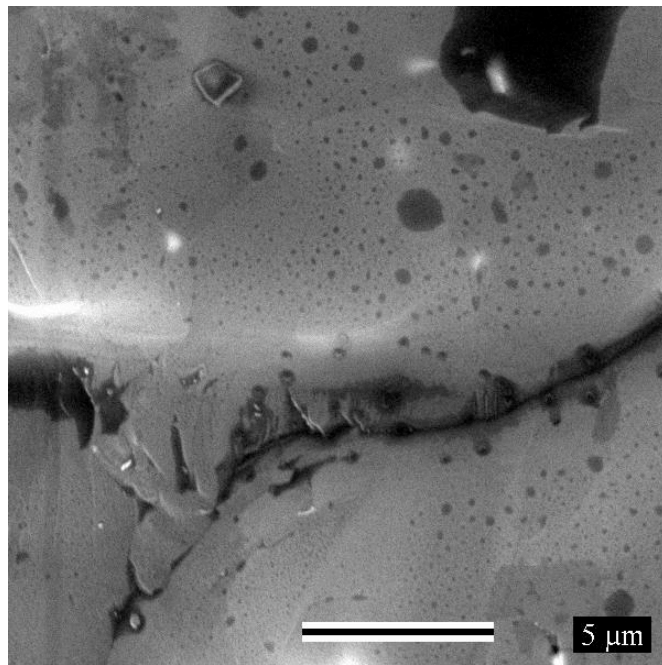
Figure 4-25: Fractured surface of B$_4$C + 10 vol% TiB$_2$ (5 μm scale).

133

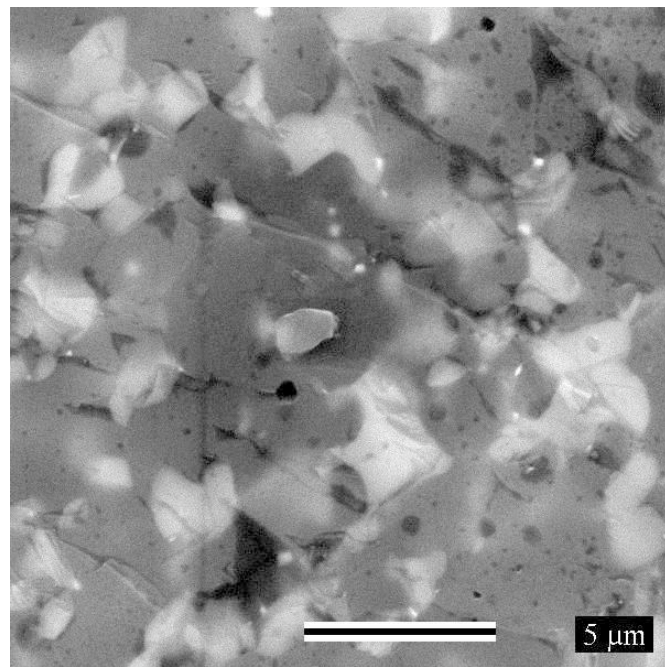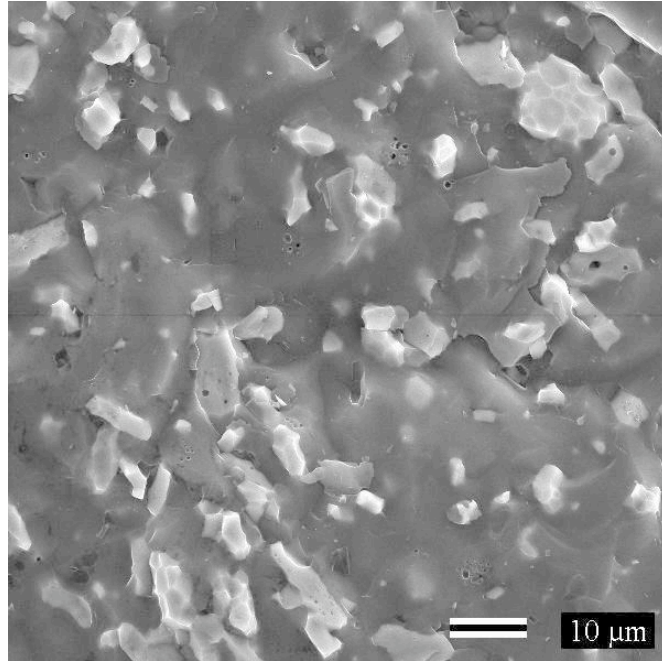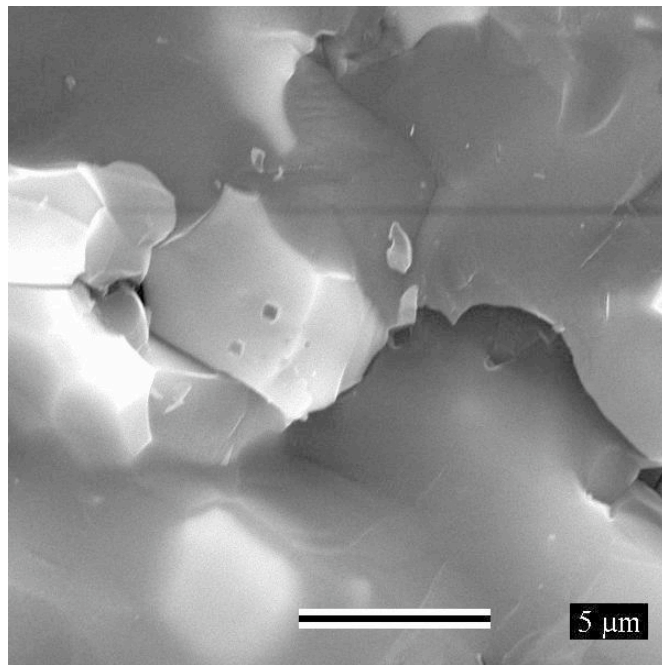**Figure 4-26:** Fractured surface of B_4C + 20 vol% TiB_2 (10 μm scale).

Figure 4-27: Fractured surface of B_4C + 20 vol% TiB_2 (5 μm scale).

134

For all of the above images, the dark areas represent the boron carbide matrix and the lighter areas represent the given particulate reinforcements. The grain-size of each ceramic composition was determined by using a modified version of the line intercept method, in which the total length of a line that was arbitrarily placed along the width of the SEM image was related to the total number of grain boundaries that were intersected as well as the magnification level that was used, as seen in Equation 3-3. The resultant grain-size calculations had a very large scatter, which was mostly attributed to that fact that a fine grain structure image could not be obtained from either the fractured surface or the lapped specimens for each composition. Therefore, these results could only be used to make broad conclusions of the microstructure. With this in mind, the grain-size of the fractured surfaces presented in these aforementioned figures can be characterized as very fine, with average grain-sizes being less than 5 μm for the pure B_4C and all of the SiC compositions, and less than 10 μm for the TiB_2 compositions. These observations are further verified by the SEM images of the starting ceramic powders.

The images of the fractured surfaces were also used to determine the modes of fracture present within each ceramic composition. Fractured surfaces are often described as to whether a crack passes through or between grains, which is known as transgranular and intergranular, respectively.

In transgranular fracture, the fracture travels through the grain of the material and changes direction because of the lattice orientations within each grain. This type of fracture is present in the TiB_2 ceramic compositions, as evident by the images of the fractured surface being fairly smooth looking and having few sharp edges. The SEM images of Figure 4-24 through Figure 4-27 show that the crack followed the edges of the

135

lattices until a TiB_2 grain was reached, at which point the crack ripped through the grain and continued on through the matrix.

Likewise, transgranular fracture was also present in the fractured surfaces of the pure B_4C ceramic, which may be seen in Figure 4-18 and Figure 4-19.

Transgranular fracture also occurred in the SiC ceramic compositions, however some intergranular fracture was also observed. Intergranular fracture involves a propagating crack that travels along the grain boundaries of the material, and not through the actual grains. This type of fracture is generally seen in images that have are jagged looking and have slightly bumpy edges. Likewise, straight edges of the grain and shiny surface may be seen in Figure 4-20 through Figure 4-23.

4.4. MECHANICAL PROPERTIES

The resultant data from the mechanical property testing that was conducted on each of the sintered, fully dense boron carbide-based ceramic materials is outlined in the following sections. Information regarding the microhardness hardness values that were measured using Vickers microhardness indentations, the fracture toughness values using Chevron-notched four-point bend testing, the flexure strength measurements using four-point bend testing, and the calculated static elastic modulus using are presented.

4.4.1. VICKERS MICROHARDNESS

Vickers microhardness values were measured using a commercially available microindenter on scrap pieces of material that were left over from the machining of the four-point bend specimens. Indentations were completed at a loading of 1000 kg_f for a

15 s dwell time. The resulting microhardness values, HV_{1000}, for each of the compositions were calculated using Equation 2-8 from Section 2.4.1.2.

The following figures represent plots of the Vickers microhardness as a function of the given trial number. The resultant data for the pure B$_4$C specimens may be seen in Figure 4-28, while B$_4$C + 10 vol% SiC may be seen in Figure 4-29, B$_4$C + 20 vol% SiC in Figure 4-30, B$_4$C + 10 vol% TiB$_2$ in Figure 4-31, and B$_4$C + 20 vol% TiB$_2$ in Figure 4-32.
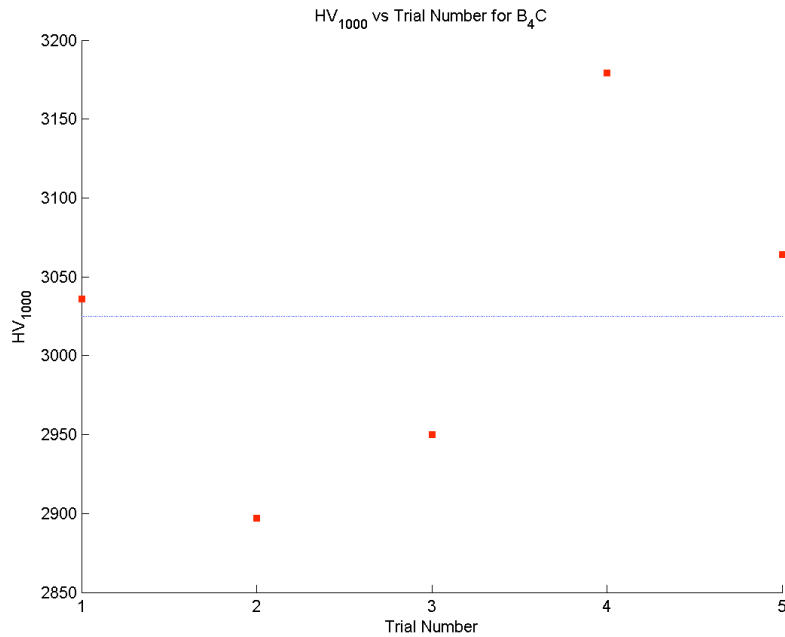
Figure 4-28: Vickers microhardness vs trial number for fully dense B$_4$C.

Figure 4-29: Vickers microhardness vs trial number for fully dense B$_4$C + 10 vol% SiC.

Figure 4-30: Vickers microhardness vs trial number for fully dense B$_4$C + 20 vol% SiC.

138

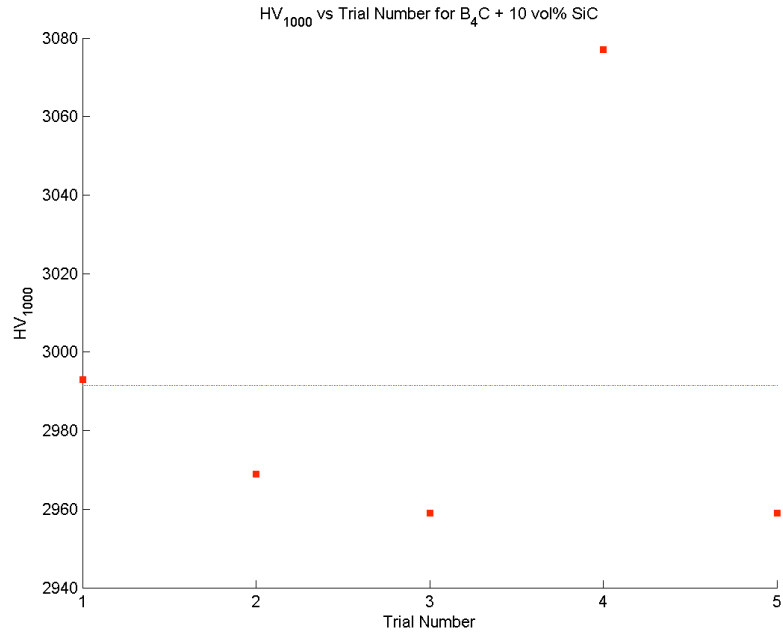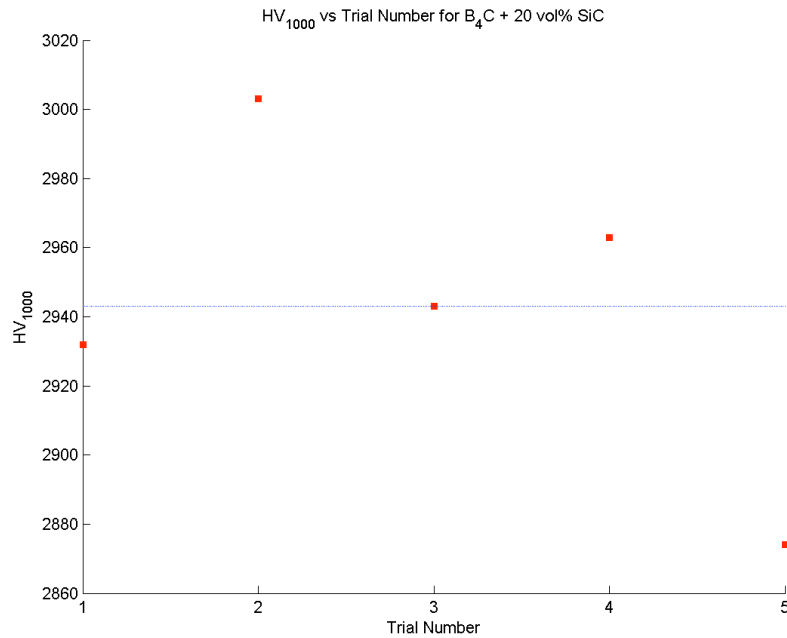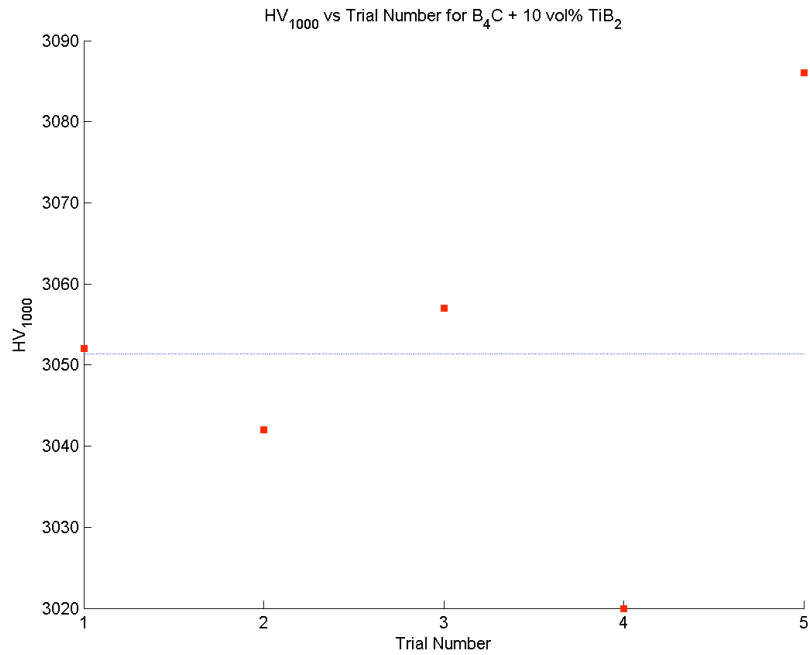**Figure 4-31:** Vickers microhardness vs trial number for fully dense $B_4C + 10$ vol% TiB_2.
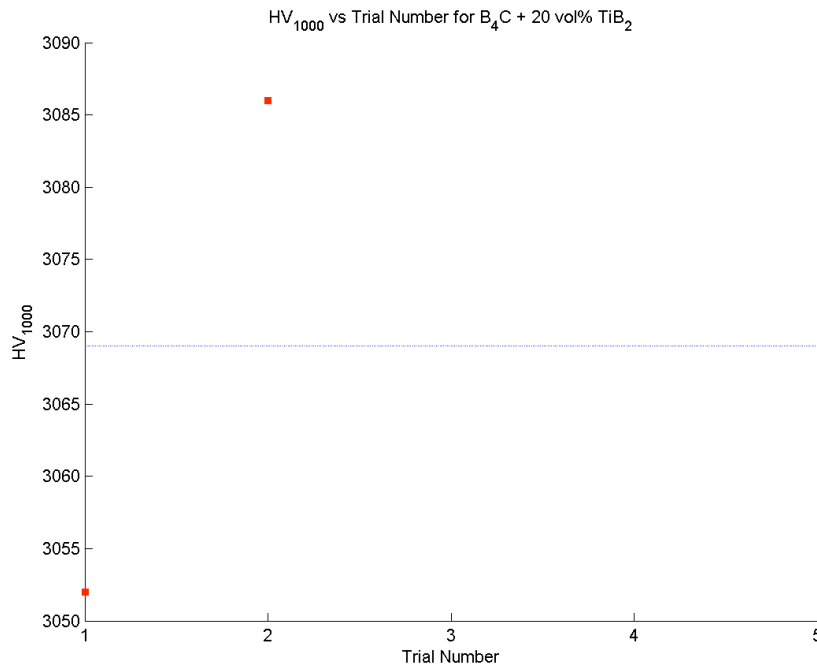
Figure 4-32: Vickers microhardness vs trial number for fully dense $B_4C + 20$ vol% TiB_2.

139

As seen in these figures, the plots of the Vickers microhardness values yield a somewhat sporadic, non-linear relationship. This correlation can be expected based upon the manner in which the data was collected. As mentioned in Section 3.3.1, the area for which microhardness indentations were performed upon was purposefully chosen in a somewhat random manner in order to ensure that the resultant microhardness data would represent an average for the entire bulk material. The data would be somewhat skewed if only a small, finite area of the entire sample was chosen to conduct testing upon. In order to determine just how sporadic these microhardness values really were, a statistical analysis was performed on the resultant data for each composition and the results of this analysis may be seen below in Table 4-5.

Table 4-5: Statistical analysis of Vickers microhardness calculations.

Composition	n	$\bar{x}$	$\acute{o}_{\bar{x}}$	C_v	$SE_{\bar{x}}$	CI
B_4C	5	3052	109	3.6	48.7	95.4
B_4C + 10 vol% α-SiC	5	2991	50	1.7	22.3	43.7
B_4C + 20 vol% α-SiC	5	2943	47	1.6	21.1	41.3
B_4C + 10 vol% TiB_2	5	3051	24	0.8	10.7	21.0
B_4C + 20 vol% TiB_2	2	3069	24	0.8	17.0	33.3

As seen in this table, even though the variations in the magnitudes of the calculated microhardness values from trial to trial for a given composition is quite large, the overall relative scatter present in the data sets are fairly low. This concept is verified by the fact that all of the coefficients of variation values are relatively small, with the largest value being 3.6 for the pure B_4C samples. The relative closeness of the data is

140

also evident in the relatively small standard deviation and standard error of the mean values. The largest calculated 95% confidence interval was found to be almost ±95.4 for the pure B_4C samples, which translates to ±3.1% when compared to the average value, and represents the range of values that is likely to enclose the true value of the average for the total given population of the pure B_4C specimens.

The microhardness of a material is an important mechanical property because it relates how much the material will inelasticly deform when a surface load is applied. An increased microhardness value when compared to that of pure B_4C will result in a material being more resistant to indentation at a given load, which will signify that the material will be able to plastically deform more so than the monolithic ceramic. Therefore, the greater the microhardness of the ceramic, the greater resistance it has to deformation.

4.4.2. FRACTURE TOUGHNESS

Fracture toughness values were measured using Chevron-notched four-point bend specimens. Bend bars were tested at a crosshead speed of 0.20 mm/min on a fixture that had an outer span of 19 mm and an inner span of 10 mm. The resulting facture toughness values, K_{Ic}, for each of the compositions were calculated using Equation 2-10 and Equation 2-11 from Section 2.4.2.2.

The following figures represent plots of the apparent applied load to the bend bar specimen versus the resultant crosshead displacement. The resultant data that was obtained for the pure B_4C specimens may be seen in Figure 4-33, while the plot for B_4C

+ 10 vol% SiC may be seen in Figure 4-34, B_4C + 20 vol% SiC Figure 4-35, B_4C + 10

vol% TiB_2 in Figure 4-36, and the plot of B_4C + 20 vol% TiB_2 in Figure 4-37.
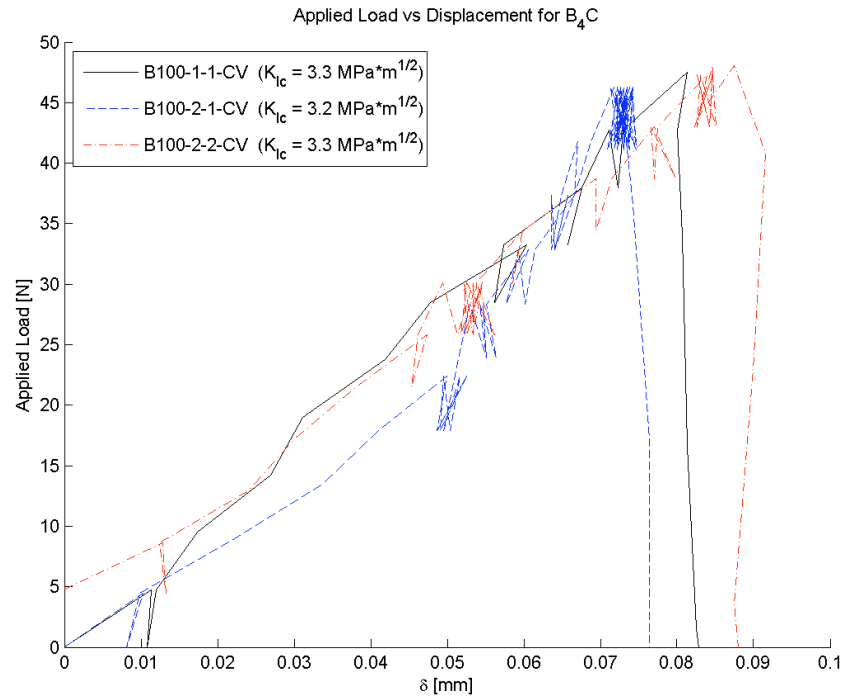
Figure 4-33: Applied load vs displacement for fully dense B_4C.

Figure 4-34: Applied load vs displacement for fully dense B$_4$C + 10 vol% SiC.

Figure 4-35: Applied load vs displacement for fully dense B$_4$C + 20 vol% SiC.

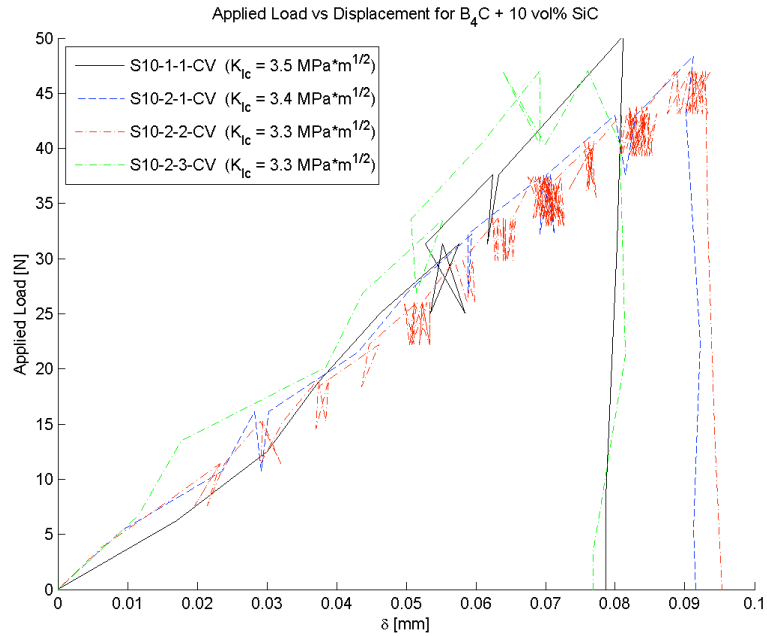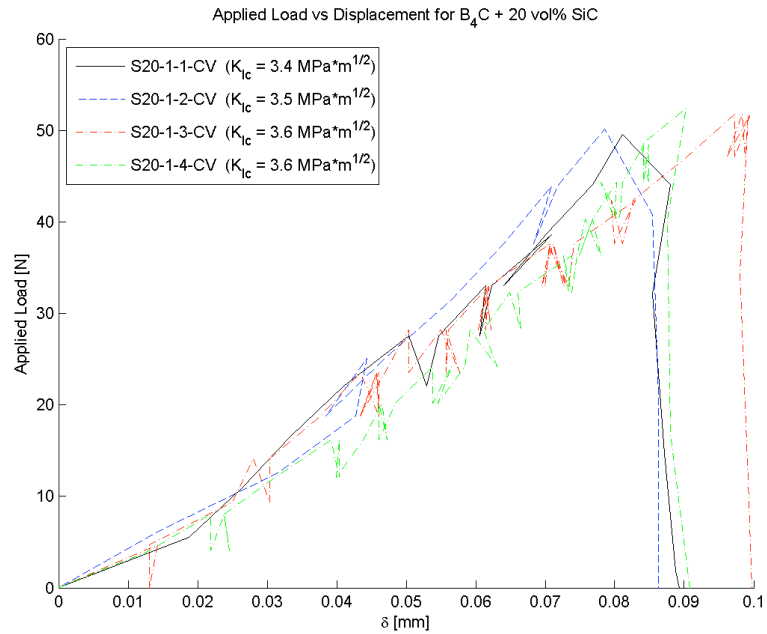143
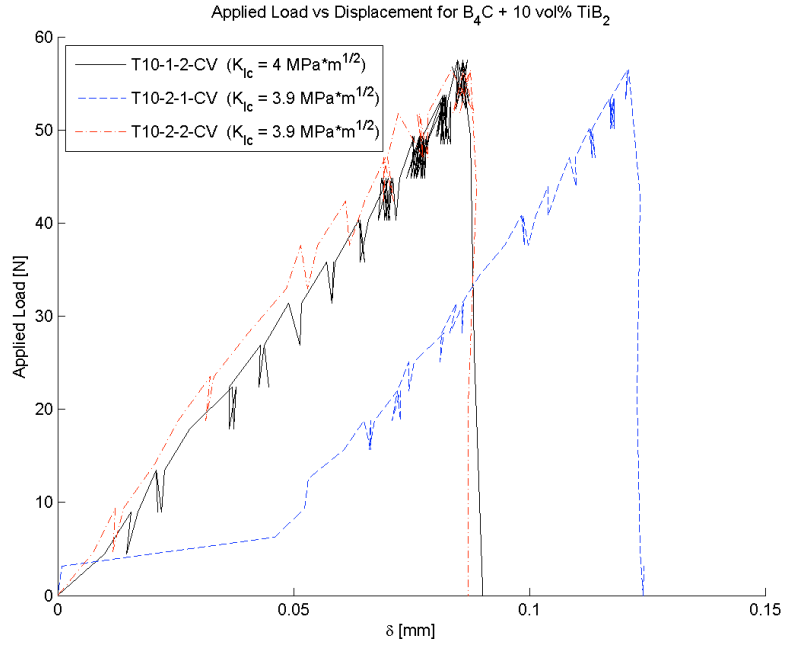
Figure 4-36: Applied load vs displacement for fully dense B_4C + 10 vol% TiB_2.
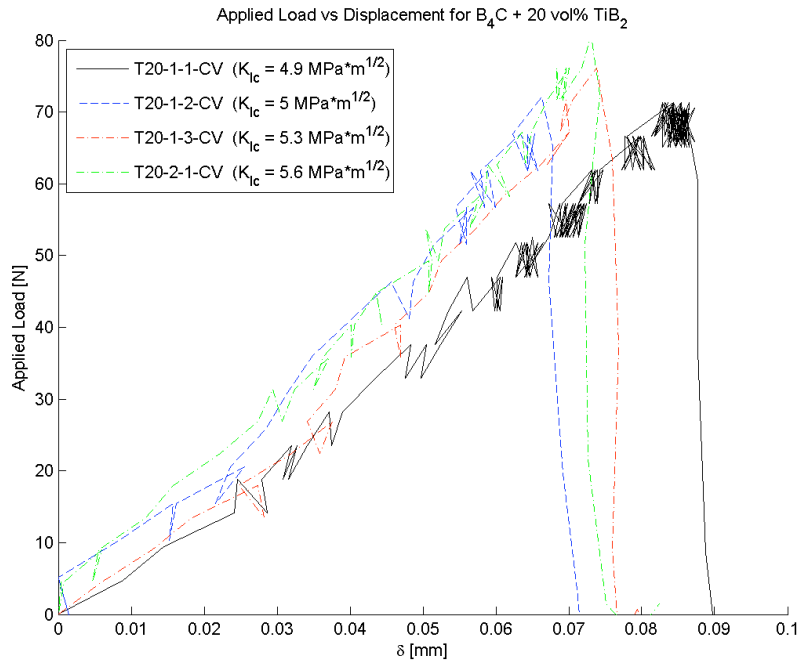
Figure 4-37: Applied load vs displacement for fully dense B_4C + 20 vol% TiB_2.

144

As seen in these figures, the plots of the applied load versus the crosshead displacement produce a somewhat jagged, fairly linear relationship up until a certain point. It is at this point that the bend bar specimen breaks and the apparent load that is read by the testing machine drops below zero, and thus becomes a non-factor. The force at which the bend bar fails, known as the breaking force, is used along with Equation 2-10 and Equation 2-11 from Section 2.4.2.2 in order to calculate the facture toughness.

The jagged, somewhat linear relationship seen in every bend bar specimen is more than likely attributed to small amounts of compliance present in either the testing fixture of the bend bar specimens themselves. The testing fixture could have compliance because of the slight differences in the hardness values of the fixture material and the bend bar specimens. However, because the fixture was manufactured out of silicon carbide, which has a hardness value that is somewhat similar to that of boron carbide, it was assumed that compliance stemming from this hardness mismatches was relatively minimal. Therefore, it was assumed that any compliance stemming from the test fixture was more than likely attributed to the positioning of the bend bar specimen within the fixture. Because each bend bar was loaded individually, slight differences in the exact positioning of the fixture-specimen setup undoubtedly occurred, no matter how carefully they were loaded. These slight differences could account for the fact that not all of the compliance that is inherent to each individual curve is consistent with one another.

The jaggedness of the load-displacement curves may also be attributed to compliance within the actual bend bars themselves. It is possible that as the bend test progresses and the applied load is increased, the resultant bending that the bar undergoes does not happen in a smooth manner because obstacles, such as the presence of multiple

145

grains or particulates, obstruct the bending path. Experiments could not be conducted in order to attempt to model the overall compliance within the testing system, however, because the amount that is present within each individual bend bar specimen is not remotely constant.

Even though the load-displacement curves are somewhat jagged and vary from specimen to specimen, the breaking force of the specimens for each composition remains fairly close to one another. In order to determine just how close these values really are, a statistical analysis was performed on the calculated fracture toughness values, and the results of this analysis may be seen below in Table 4-6.

Table 4-6: Statistical analysis of the fracture toughness calculations.

Composition	n	$\bar{x}$	$\acute{o}_{\bar{x}}$	C_v	$SE_{\bar{x}}$	CI
B_4C	3	3.28	0.062	1.876	0.036	0.070
B_4C + 10 vol% α-SiC	4	3.34	0.104	3.126	0.052	0.102
B_4C + 20 vol% α-SiC	4	3.54	0.092	2.586	0.046	0.090
B_4C + 10 vol% TiB_2	3	3.94	0.042	0.063	0.024	0.047
B_4C + 20 vol% TiB_2	4	5.21	0.296	5.691	0.015	0.290

As seen in this table, the fracture toughness of a given specimen for each of the five compositions remains fairly constant, as evident by all of the coefficients of variation values being less than 6.00. The C_v values dictate the overall magnitude of variation relative to the size of the observed values, and as such, some compositions were found to have data that were extremely close to one another. The relative closeness of the data is also evident in the relatively small standard deviation and standard error of the mean

146

values. The largest calculated 95% confidence interval was found to be almost ± 0.290 for the 20 vol% TiB_2 specimens, which translates to ±5.6% when compared to the average value, and represents the range of values that is likely to enclose the true value of the average for a given population. The fracture toughness is greatly influenced by the size and severity of flaws existing within the ceramic samples, which is directly related to the amount of porosity inherent to the sintered material. Because only fully dense sintered samples (≥99% theoretical) were chosen for this research, the level of porosity was kept to a minimum and, therefore, the statistical data of this mechanical property is very precise.

The fracture toughness of a material is important because it allows for an understanding of the extent to which these flaws govern the overall toughness of the material. If the applied load to a given ceramic is too great, these inherently present flaws may suddenly grow and cause the material to fail in a brittle manner. Therefore, if the fracture toughness of a material is increased, then the material will be able to withstand a higher stress before a preexisting flaw is propagated and, thusly, the brittleness of the ceramic will be decreased. Materials with high fracture toughness values when compared to that of pure B_4C will be able to absorb more energy from an approaching crack than the monolithic ceramic because they are better able to resist crack propagation under an applied load.

4.4.3. FLEXURE STRENGTH

Flexure strength values were measured using four-point bend specimens. As with the fracture toughness, bend bars were tested at a crosshead speed of 0.20 mm/min on a

www.manaraa.com

fixture that had an outer span of 19 mm and an inner span of 10 mm. The resulting flexure strength values, σ_{fb}, for each of the compositions were calculated using Equation 2-12 from Section 2.4.3.2.

The following figures represents plots of the bending stress and equivalent applied load to the given bend bar specimen versus the crosshead displacement that was measured from the testing machine. The resultant data that was obtained for the pure B_4C data may be seen in Figure 4-38, while the plot for B_4C + 10 vol% SiC may be seen in Figure 4-39, B_4C + 20 vol% SiC in Figure 4-40, B_4C + 10 vol% TiB_2 in Figure 4-41, and the plot of B_4C + 20 vol% TiB_2 in Figure 4-42.
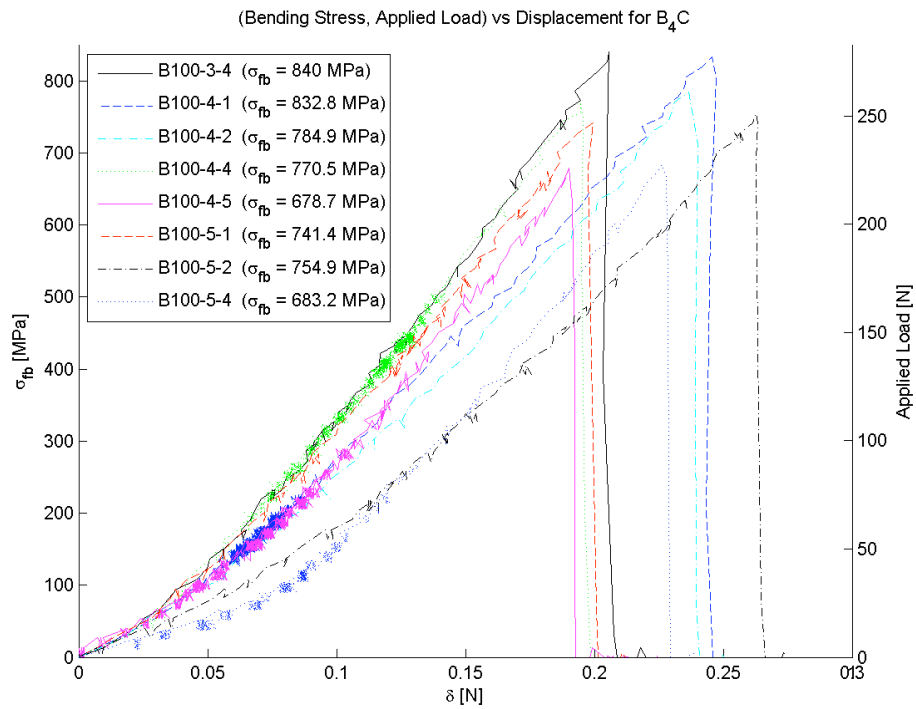
Figure 4-38: Bending stress and applied load versus displacement for fully dense B_4C.

148

Figure 4-39: Bending stress and applied load versus displacement for fully dense B_4C + 10 vol% SiC.
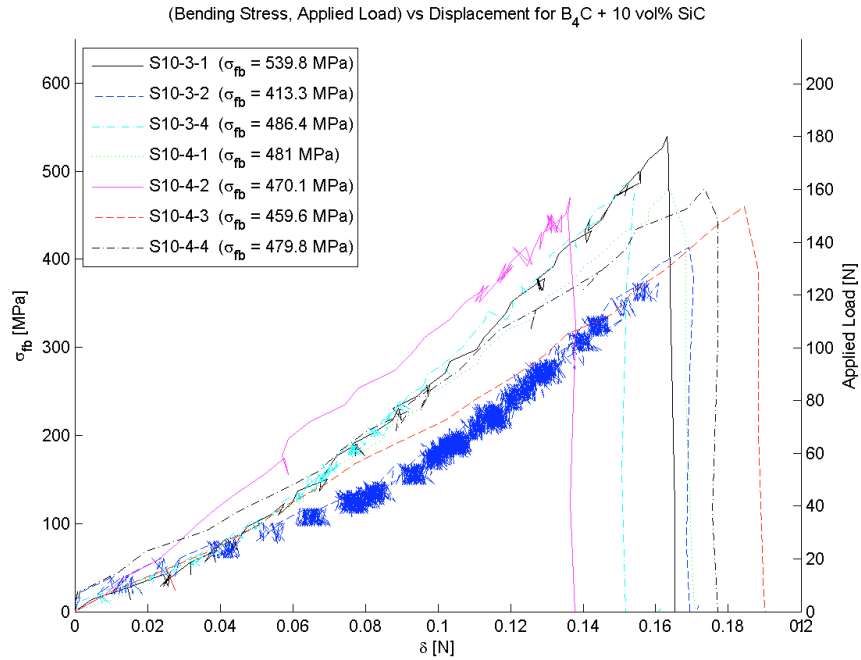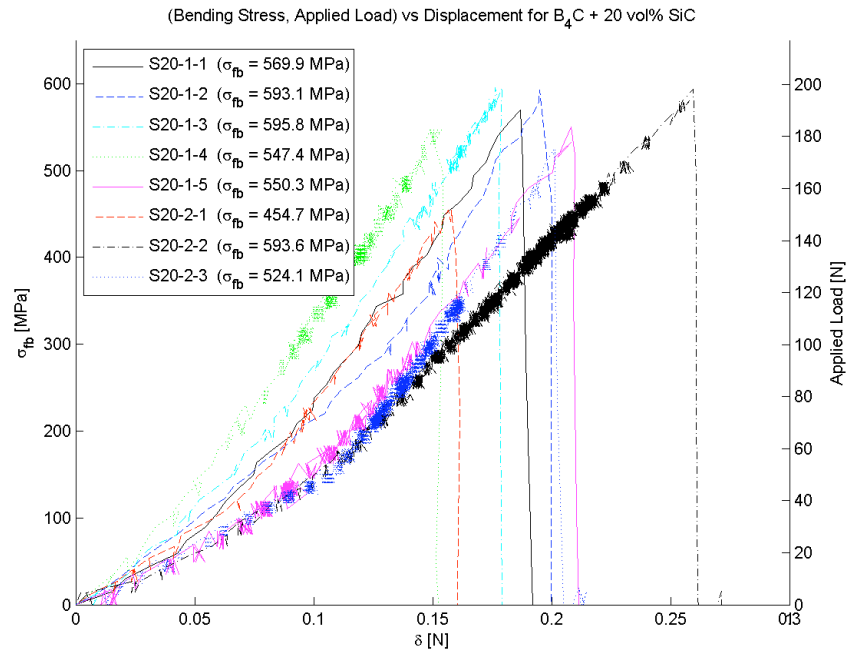

Figure 4-40: Bending stress and applied load versus displacement for fully dense B_4C + 20 vol% SiC.

149
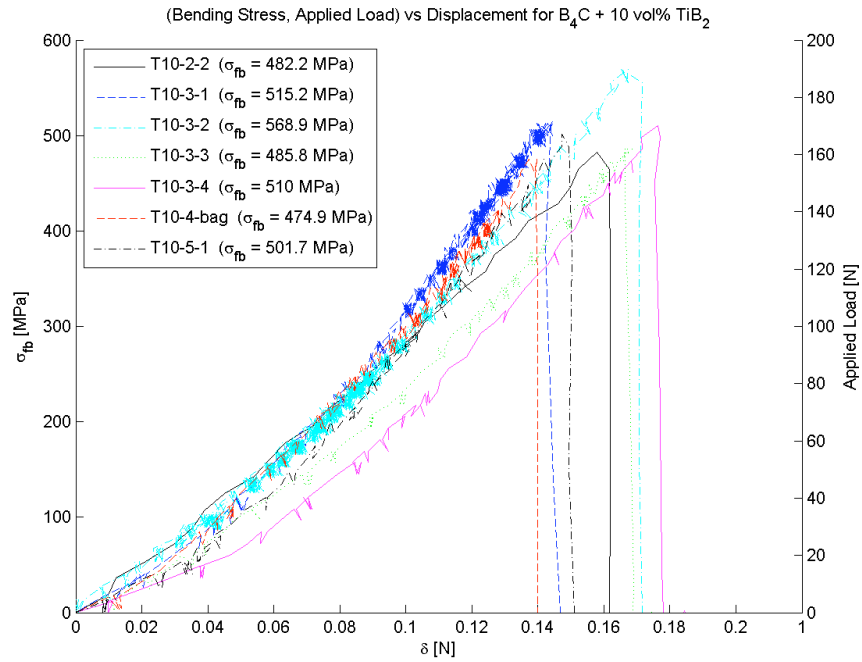
Figure 4-41: Bending stress and applied load versus displacement for fully dense B_4C + 10 vol% TiB_2.
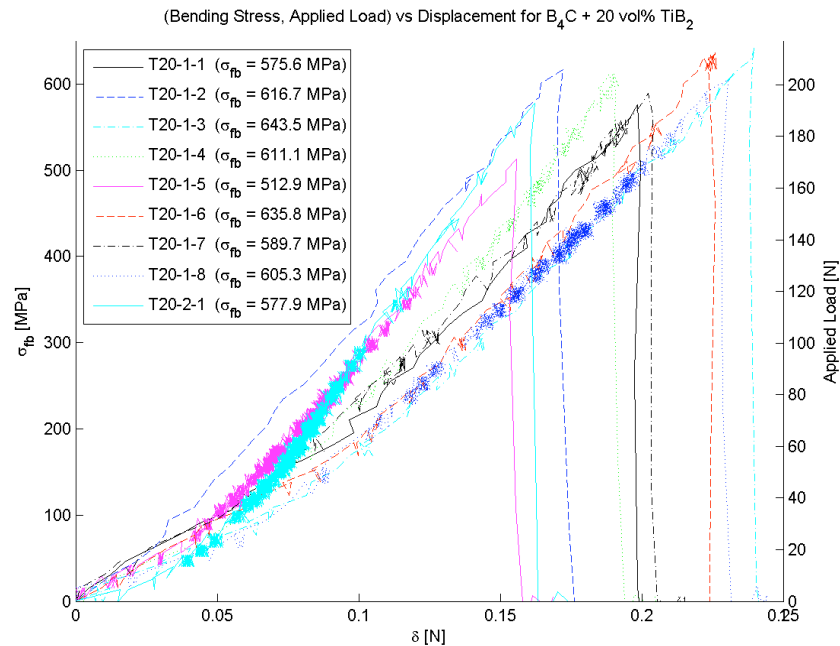
Figure 4-42: Bending stress and applied load versus displacement for fully dense B_4C + 20 vol% TiB_2.

150

As seen in these figures, the plots of the bending stress and applied load versus the crosshead displacement produce the same somewhat jagged, fairly linear relationship that was viewed in the fracture toughness plots from Section 4.4.2.

The point at which the bend bar specimen fails is represented by a sharp decrease in the apparent load. This point represents the maximum amount of energy the bend bar is able to withstand before it fractures due to tension. This breaking force is used along with Equation 2-12 in order to calculate the flexure strength.

The jagged, somewhat linear relationship present in every bend bar specimen is, again, more than likely attributed to small amounts of compliance present in either the testing fixture of the bend bar specimens themselves. Likewise, even though the flexure strength-load-displacement curves are somewhat jagged and vary from specimen to specimen, the breaking force of the specimens for each composition remains fairly close to one another. In order to determine just how close these values really are, a statistical analysis was performed on the resultant flexure strength values, and the results of this analysis may be seen below in Table 4-7.

Table 4-7: Statistical analysis of the flexure strength calculations.

Composition	n	$\bar{x}$	$\acute{o}_{\bar{x}}$	C_v	$SE_{\bar{x}}$	*CI*
B$_4$C	8	760.8	60.1	7.90	21.26	41.66
B$_4$C + 10 vol% α-SiC	7	475.7	37.5	7.89	14.19	27.81
B$_4$C + 20 vol% α-SiC	8	553.6	47.7	8.61	16.85	33.03
B$_4$C + 10 vol% TiB$_2$	7	505.5	31.7	6.27	1.97	23.47
B$_4$C + 20 vol% TiB$_2$	9	596.5	39.2	6.56	13.05	25.8

151

The flexural strength of ceramics is greatly influenced by several parameters associated with the testing procedure, such as the testing rate, testing environment, specimen size, specimen preparation, and testing fixtures. Likewise, the flexural strength is dependent on both its inherent resistance to fracture and the size and severity of flaws existing within the ceramic. Variations in these cause a natural scatter in test results for a given sample of test specimens.

The flexure strength only applies to brittle materials such as ceramics. For ductile materials, the approximate equivalent mechanical property is the ultimate strength. The flexure strength of a material is important because it is a direct measure of the tensile strength of a ceramic material.

The flexure strength of a material is important because it is a direct measure of the tensile strength of a ceramic material. An increase in the flexure strength of the ceramic translates into the material being able to withstand a higher stress, and therefore a higher load, before failing. Therefore, materials with low flexure strength values when compared to that of pure B_4C will not be able to absorb as high of a mechanical loading before failing.

4.4.4. ELASTIC MODULUS

The results from the modulus of rupture four-point bend bars with strain gages attached may be seen in the below figures. The elastic modulus, *E*, was calculated from the resultant stress and strain data that were measured during the breakage of a strain gage-attached flexure strength four-point bend bar. These sets of data were plotted against one another and the slope of the corresponding linear best-fit line was evaluated

152

and set equal to the elastic modulus. The stress versus strain plots for the resultant data that was obtained for the pure B_4C data may be seen in Figure 4-43, while the plot for B_4C + 10 vol% SiC may be seen in Figure 4-44, B_4C + 20 vol% SiC in Figure 4-45, B_4C + 10 vol% TiB_2 in Figure 4-46, and the plot of B_4C + 20 vol% TiB_2 in Figure 4-47.
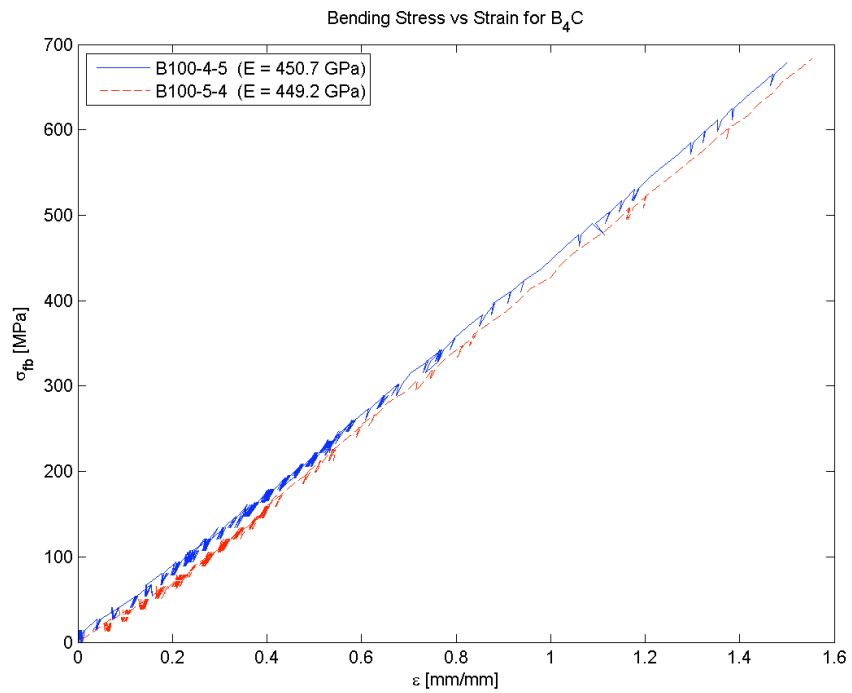
Figure 4-43: Stress vs strain curve for fully dense B_4C.
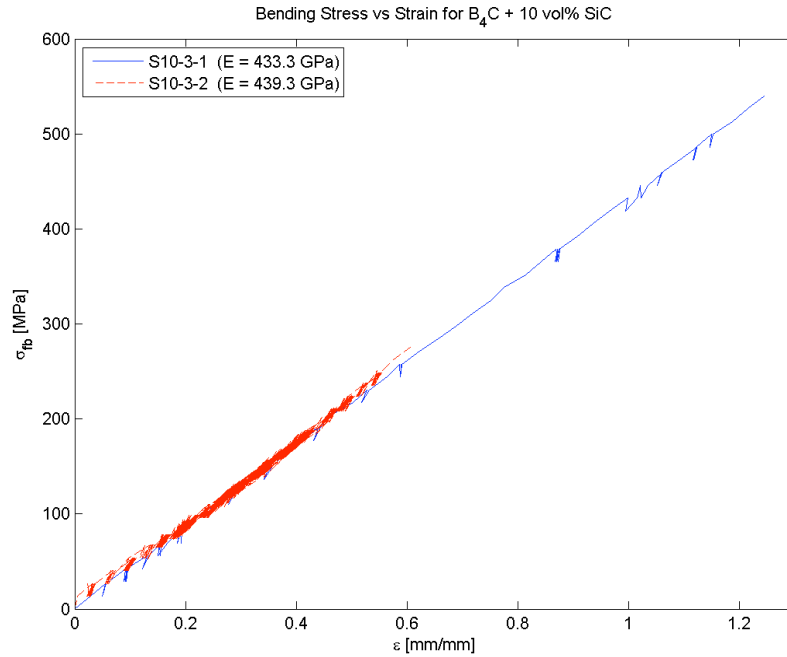
Figure 4-44: Stress vs strain curve for fully dense B$_4$C + 10 vol% SiC.
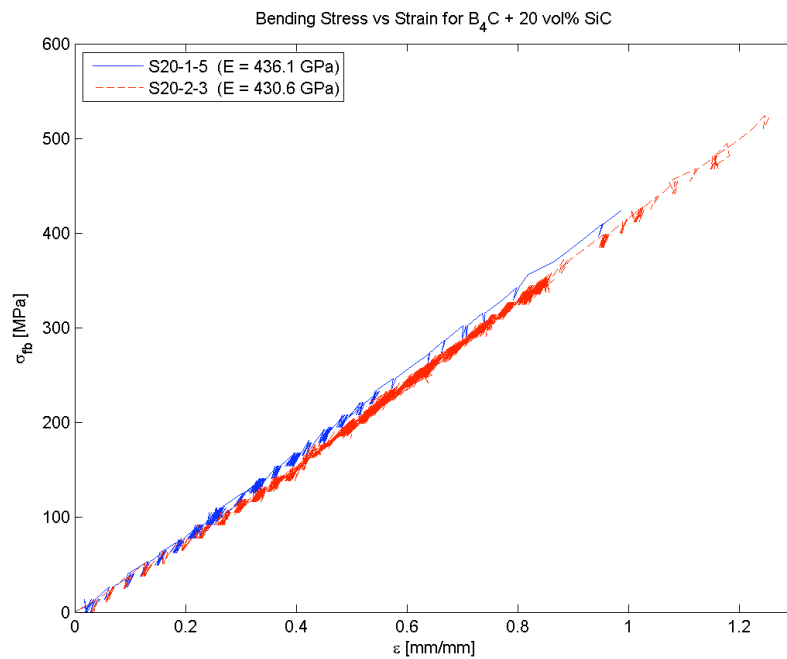
Figure 4-45: Stress vs strain curve for fully dense B$_4$C + 20 vol% SiC.

154
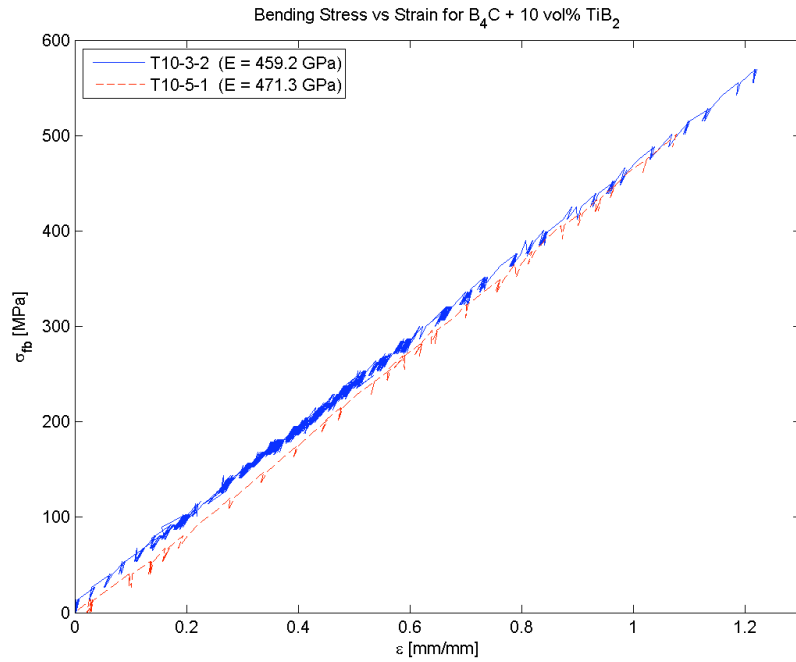
Figure 4-46: Stress vs strain curve for fully dense $B_4C + 10$ vol% TiB_2.
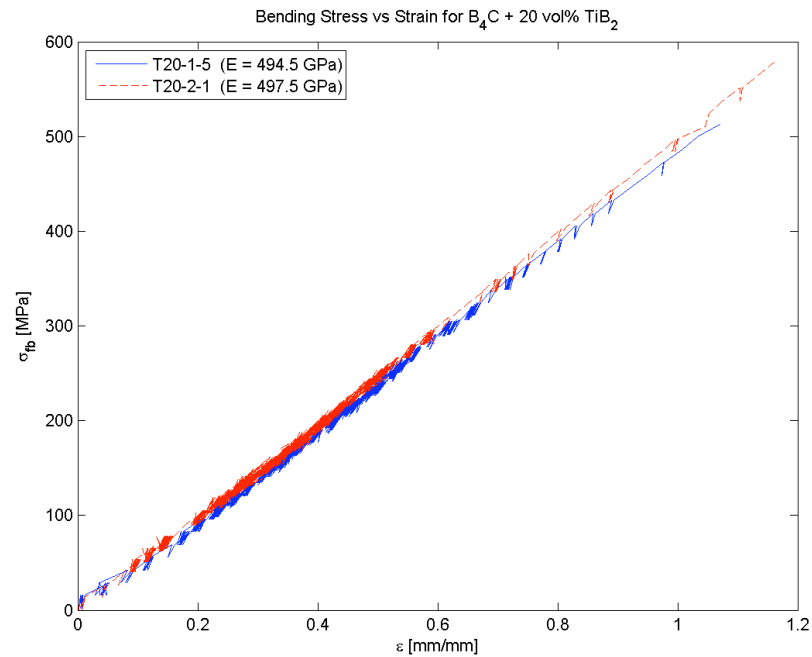
Figure 4-47: Stress vs strain curve for fully dense $B_4C + 20$ vol% TiB_2.

155

As seen in these figures, the plots of the stress versus strain produce a linear relationship. As mentioned in Section 2.4.4, the static method for determining the elastic modulus of a ceramic material is completed by numerically quantifying this linear relationship. The tightness of the two sets of linear data points within each of these figures suggests that the resulting relationships are relatively close to one another, which implies that the elastic modulus values are also relatively close. In order to determine just how close these values really are, a statistical analysis was performed on the calculated linear regression models that were created for each composition. The results of this analysis may be seen below in Table 4-8.

Table 4-8: Statistical analysis of elastic modulus calculations.

Composition	n	$\overline{\mathrm{x}}$	$\acute{o}_{\overline{x}}$	C_v	$SE_{\overline{x}}$	*CI*
B_4C	2	450.0	1.05	0.23	0.74	1.45
B_4C + 10 vol% α-SiC	2	436.3	4.26	0.98	3.01	5.90
B_4C + 20 vol% α-SiC	2	433.4	3.93	0.91	2.78	5.44
B_4C + 10 vol% TiB_2	2	465.3	8.62	1.85	6.10	11.95
B_4C + 20 vol% TiB_2	2	496.0	2.13	0.43	1.51	2.95

As seen in this table, the elastic modulus of a given specimen for each of the five compositions remains fairly constant, as evident by all of the coefficients of variation values being less than 2. The C_v values dictate the overall magnitude of variation relative to the size of the observed values. The relative closeness of the data is also evident in the relatively small standard deviation and standard error of the mean values. The largest calculated 95% confidence interval was found to be almost ±12 for the 10 vol% TiB_2

156

specimens, which translates to ±2.6% when compared to the average value, and represents the range of values that is likely to enclose the true value of the average for a given population. The elastic modulus is greatly influenced by the size and severity of flaws existing within the ceramic samples, which is directly related to the amount of porosity inherent to the sintered material. Because only fully dense sintered samples (≥99% theoretical) were chosen for this research, the level of porosity was kept to a minimum and, therefore, the statistical data of this mechanical property is very precise.

The elastic modulus of a material is an important mechanical property because it is a direct measure of the resistance of the material to relative atomic separation, which is inherently known as its stiffness. Elastic properties of a material are a measure of the force required to displace atoms relative to one another. Therefore, an increase in the elastic modulus translates into a greater force that is required to move the atoms from their equilibrium position within a given ceramic body. Therefore, materials with high elastic modulus values when compared to that of pure B_4C will be stiffer than the monolithic ceramic because they are better able to resist changes in dimension under an applied load.

4.4.4.1. Voigt-Reuss Model

A theoretical model containing upper- and lower-bounds was created in order to test the accuracy and validity of the elastic modulus measurements for each of the ceramic compositions. This model, termed the Voigt-Reuss Model, predicts these bounds by relating the elastic moduli of the individual constituents within the material to their respective volumetric ratios. The theoretical bounds were found by assuming the

157

composite material consists of layers that are either parallel or perpendicular to an applied uniaxial stress. The Voigt-Reuss model also assumes that the strain in each of the constituent is the same and that the composite ceramic material is completely isotropic.

The Voigt-Reuss model uses stress and strain averaging techniques to predict the upper- and lower-bounds for the constitutive relationships. The upper bound, E_U, can be calculated using Equation 4-6, where E_1 is the elastic modulus of the main phase, E_2 is the elastic modulus of the secondary phase, and V_2 is the volume fraction of the secondary phase. In this bound, most of the applied stress is carried by the high modulus phase.

$$E_U = V_2 E_2 + (1 - V_2)E_1 \qquad \textbf{(4-6)}$$

With this in mind, the lower bound, E_L, can be calculated using Equation 4-7. In this bound, it is assumed that the stress in each phase remains the same.

$$\frac{1}{E_L} = \frac{V_2}{E_2} + \frac{(1 - V_2)}{E_1} \qquad \textbf{(4-7)}$$

In order for these two values to represent the most accurate bounds, any statistical variation that was given for the assumed theoretical values of the elastic modulus of the constituent materials was equated to be the most extreme for each individual bound, which means that any given error was added to the given average value for the upper bound and subtracted for the lower.

158

The numerical results from the theoretical model that were obtained using the mechanical property data from Table 2-1, Table 2-2, and Table 2-3 for pure B_4C, SiC, and TiB_2, respectively, and may be seen below in Table 4-9. As seen in this table, fairly wide bounds of 8.0 GPa, 10.1 GPa, 12.1 GPa, 14.3 GPa, and 20.3 GPa exist for the B_4C, B_4C + 10 vol% SiC, B_4C + 20 vol% SiC, B_4C + 10 vol% TiB_2, and B_4C + 20 vol% TiB_2 data, respectively.

Table 4-9: Expected bounds for the elastic modulus values based on the Voigt-Reuss model.

Composition	Lower Bound [GPa]	Upper Bound [GPa]
B_4C	446.0	454.0
B_4C + 10 vol% α-SiC	441.2	451.4
B_4C + 20 vol% α-SiC	436.6	448.7
B_4C + 10 vol% TiB_2	453.7	467.9
B_4C + 20 vol% TiB_2	461.6	481.9

When the calculated elastic modulus values are compared to those predicted by the Voigt-Reuss model seen in the above table, it is found that only the pure B_4C ceramic completely lies within the predicted model. The SiC and TiB_2 composites all fall slightly outside of the bounds, which is more than likely attributed to not having mechanical data on the exact SiC and TiB_2 powders that were used for this investigation. Therefore, the elastic modulus values used to predict the modulus values of the composites were not as accurate as they could have been had more accurate data on each of the constituents been provided.

159

CHAPTER 5: CONCLUSIONS

This chapter summarizes the resultant data and ties together all of the mechanical properties that were measured in this investigation.

5.1. EFFECT OF SiC ON B_4C

Through the careful examination of the aforementioned data, it is found that SiC increases the overall strength of B_4C slightly. The hardness of the SiC materials decreased slightly, which is not surprising considering that SiC is a slightly softer material than B_4C. However, this decrease is not overly statistically significant because of the relatively large error associated with the measured hardness values of the pure B_4C ceramic. The fracture toughness of composites containing SiC increased slightly when compared to that of monolithic B_4C. This increase was because of the crack deflection toughening mechanism, which was evident in the fractography of the fractured surfaces of the Chevron-notched four-point bend bars seen in Figure 4-20 through Figure 4-23. Divots and protrusions are seen in the fractured surfaces in these figures, which clearly represents that the crack was forced to go around the SiC particles as it propagated through the bend bar. Once the bar was loaded until failure, the SiC particles theoretically remained intact on each side of the fractured bend bar. However, because the crack was forced to go around the mechanical bonds that held each SiC particulate in

place, some remained on each side of the fractured bend bar, which is explains why there are both divots and protrusions seen in the SEM images of the fractured surfaces. Therefore, the evidence revealed by these images verifies that SiC particulate inclusions toughen monolithic B_4C by mechanically bonding to the matrix and forcing an approaching crack to deflect around each of these particles.

Because of the starting powder size, multiple small cracktip-particulate interactions were able to exist, but the effect of each interaction was small. This caused the path of the crack to change directions in order to go around the SiC particulates, which resulted in a slightly longer path length. Therefore, more energy was able to be absorbed by the material. Likewise, energy was required to physically break the mechanical bond holding the SiC within the B_4C matrix.

A decrease in the flexure strength of the material was observed. However, when the flexure strength of the monolithic B_4C ceramic is compared to data presented in the literature, as seen in Table 2-1, it is easily seen that the calculated flexure strength values for this research are over 50% larger than any other reported value. Although the exact cause of this significant increase is not quite fully understood, it is more than likely attributed to the fine grain structure that resulted from the $P^2C^{®}$ process.

Likewise, a decrease in the elastic modulus was found in the SiC-reinforced composites. The elastic modulus decrease was to be expected based on the Voigt-Reuss model that was created. The elastic modulus values, however, were slightly out of the predicted bounds, which is more than likely attributed to not having mechanical data on the exact SiC powder that was used for this investigation.

161

In conclusion, SiC successfully increased the strength (toughness) of B_4C through crack deflection, as seen in the summary of mechanical properties in Figure 5-1. Even though a decrease in the flexure strength of the material was observed, it is a decent tradeoff because of the slight increase in fracture toughness that was observed.
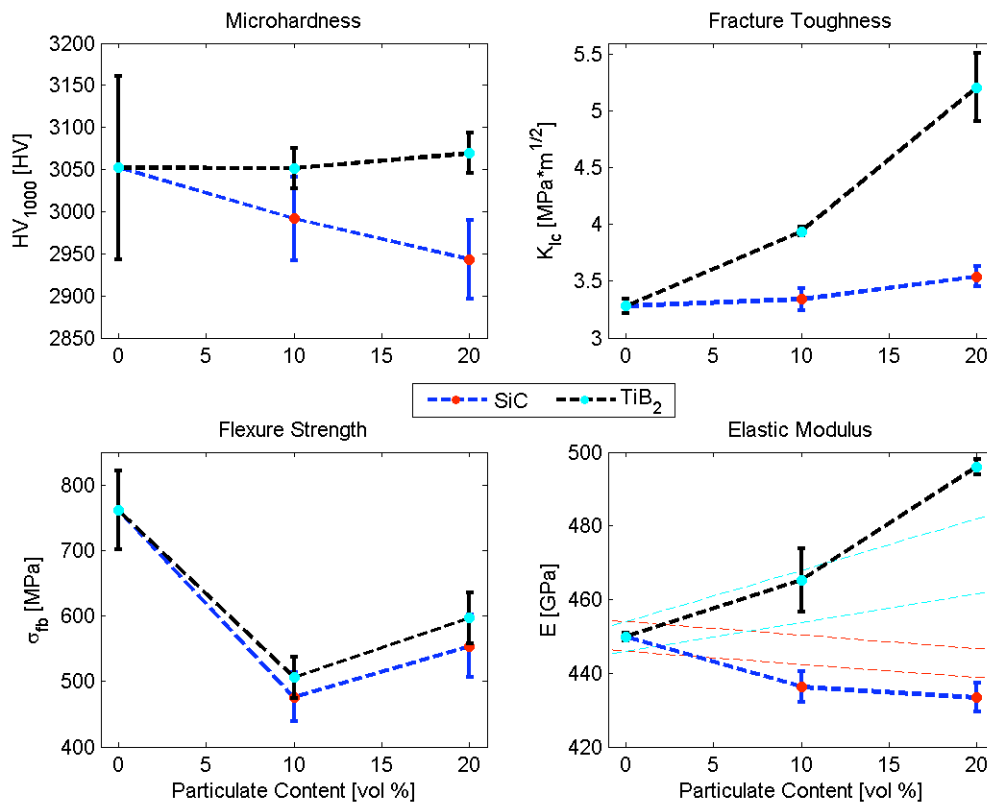

Figure 5-1: Summary of the effects of varying volume-percentage particulate inclusions of SiC and TiB_2.

5.2. EFFECT OF TiB_2 ON B_4C

As with the SiC composite materials, the overall strength of B_4C was increased through the use of TiB_2 reinforcing particles. The hardness of these composite materials

increased slightly, which is more than likely attributed to the fact that TiB_2 is stiffer than pure B_4C. However, the increase is not statistically significant because of the relatively large error associated with the measured hardness values of the pure B_4C ceramic. Significant improvements in the fracture toughness of these composites were observed when compared to that of monolithic B_4C. This increase was because of the ultra-tough particulate reinforced toughening mechanism, which was evident in the fractography of the fractured surfaces of the Chevron-notched four-point bend bars seen in Figure 4-24 through Figure 4-27. Clear cleavage planes are seen in these figures, which are represented by smooth, almost glassy looking fracture surfaces. These planes represent the fact that the crack was forced to physically break apart the chemically bonded TiB_2 particles as it propagated through the bend bar. Once the bar was loaded until failure, the TiB_2 particles theoretically remained lodged within the fractured surfaces of each portion of the bend bar. However, because the crack was forced to rip the chemically bonded particulates apart, a portion of each particle remained on each side of the fractured bar. This explains why there are cleavage planes seen in the SEM images of the fractured surfaces. Therefore, the evidence revealed by these images verifies that TiB_2 particulate inclusions toughen monolithic B_4C by chemically bonding to the matrix and forcing an approaching crack to tear through each of these particles.

Because of the starting powder size, a smaller number of cracktip-particulate interactions were able to exist when compared to the SiC composites, but the amount of energy absorbed by each particle was significantly higher. Rather than the crack bending or fully deflecting around the path of the TiB_2 particles, it simply broke through it. This

163

caused a tremendous amount of energy to be dissipated through the broken particle, and, therefore, more energy was able to be absorbed by the material.

As with the SiC composites, a decrease in the flexure strength of the material was also observed. Again, when the flexure strength of the monolithic B_4C ceramic is compared to data presented in the literature, this decrease is not all relatively severe.

An increase in the elastic modulus was found in the TiB_2-reinforced composites, which was expected based on the Voigt-Reuss model that was created. The elastic modulus values, however, were slightly out of the predicted bounds, which is more than likely attributed to not having mechanical data on the exact type of TiB_2 that was used for this investigation.

In conclusion, TiB_2 successfully increased the strength (toughness) of B_4C through the ultra-tough, ultra-small particulate reinforcement toughening mechanism, as seen in the summary of mechanical properties in Figure 5-1. A crack followed the edges of the lattices in the material until a TiB_2 particle was reached, at which point the crack ripped through the grain and continued through the ceramic. This ripping effect allowed for the material to absorb much more energy then the SiC composites or the pure B_4C ceramic. Even though a decrease in the flexure strength of the material was observed, it is a decent tradeoff because of the slight increase in fracture toughness that was observed.

When the mechanical property data that was obtained from this research is compared to that seen in the literature, as outlined in Chapter 1 of this manuscript, it is found that the $P^2C^®$ processing method allowed for a significantly tougher material than the one created by Yamada.[10] The flexure strength of the material for this research was

164

slightly lower than that created by Yamada. The significant increase in the fracture toughness is more than likely attributed to the $P^2C^{®}$ processing method.

Likewise, the TiB_2 reinforced material made for this research is slightly harder than that made by Tuffe.[11] The fracture toughness and flexure strength of the material by Tuffe, however, was slightly higher than that of this research. However, this increase was attributed to the fact that 50 wt% particulate additions of TiB_2 were used.

Therefore, it is assumed that the composite with 20 vol% TiB_2 allowed for the largest gain in strength (toughness) because this composite had the most TiB_2 particles within the ceramic material, and resulted in the largest number of ultra small, ultra tough particulate-cracktip interactions.

165

CHAPTER 6: RECOMMENDATIONS FOR FUTURE WORK

In order to have a complete understanding of the B_4C-SiC and B_4C-TiB_2 systems that were investigated for this research, further testing and investigation must be completed. The following sections represent these suggestions and provide brief descriptions as to why the respective types of further testing would be worthwhile.

6.1. VARYING AMOUNTS OF PARTICULATE INCLUSIONS

Two different amounts of particulate inclusion, 10 and 20 volume-percentage of the overall ceramic material, were used for this research. Even though these ranges represent a fairly broad spectrum of the respective systems, more amounts of inclusions should be studied in order to have a full understanding of their effect on B_4C. Time and, more importantly, budgetary constraints, however, limited this investigation to the two aforementioned volume additions. Therefore, it is recommended that testing be conducted on volume additions of 15, 25 and 30 vol% in order to determine if the inclusion materials follow any type of law of diminishing returns, in that more particulate additions ultimately result in decreased mechanical properties.

166

6.2. ELEVATED TEMPERATURE TESTING

Mechanical testing at elevated temperature should also be conducted in order to fully evaluate the effect of SiC and TiB_2 on the B_4C matrix. The temperature relationship of ceramics is based upon the vibration of atoms. As the testing temperature increases, the atoms in the material vibrate with greater frequency and amplitude. This increased vibration allows the atoms under stress to slip to new places in the material, which means that they are able to break bonds and form new ones with other atoms in the material. The slippage of atoms is seen on the outside of the material as plastic deformation, which is a common feature of ductile fracture.

When temperature decreases however, the exact opposite is true. Atom vibration decreases, and the atoms do not want to slip to new locations within the material. As such, the atoms break their bonds and do not form new ones when the stress on the material becomes high enough, which promotes brittle fracture.

Therefore, it is evident that the testing temperature determines the amount of brittle or ductile fracture that can occur within a material, which therefore directly determines the effectiveness of the two separate particulate inclusions.

Also, both SiC and TiB_2 hold their mechanical strengths at relatively high temperatures, so it would therefore be worthwhile to see if these high-temperature strength properties carry over.

167

6.3. VARYING STARTING POWDER SIZES

As mentioned in Section 2.3.3, the starting powder size of ceramic samples greatly influences the overall microstructure, and thus mechanical properties, of the sintered specimen. With this concept in mind, nano-sized SiC particulates were used for this research and resulted in the toughening of B_4C through the crack deflection toughening mechanism. Because of this small-sized starting powder, multiple cracktip-particulate interactions occurred, but the extent to which the resultant crack was deflected was very small. This concept is based on the simple nature of the nano-sized SiC starting powder. In order to have a full understanding of the amount crack deflection toughens SiC-reinforced B_4C ultimately has, mechanical testing on micron-sized particulate inclusions must be considered. Micron-sized SiC particles would allow for fewer cracktip-particulate interactions to occur, but the extent at which they occur would increase because of the larger particle size.

A similar principle can be attributed to the TiB_2 ceramic samples, in that the micron-sized TiB_2 powder used for this research resulted in fewer cracktip-particulate interactions as compared to a smaller starting powder size. These interactions, however, were quite significant in that the amount of energy that was dissipated by the breaking of the reinforcing particles was quite large. In order to have a full understanding of the amount of toughening TiB_2 exhibits on B_4C, mechanical testing of sub-micron-sized TiB_2 particulate inclusions must be considered. Smaller TiB_2 particle would allow for more cracktip-particulate interactions, but the amount of energy that is consumed by each particle would be decreased.

168

LIST OF REFERENCES

1. D. Emin, "Structure and Single-Phase Regime of Boron Carbides," *Physical Review B*, **38** [9] 6041-55 (1988).

2. H. O. Pierson, *Handbook of Refractory Carbides and Nitrides: Properties, Characteristics, Processing and Applications*, Noyes Publications, Norwich, NY, 1996.

3. F. Thevenot, "Boron Carbide- A Comprehensive Review," *Journal of the European Ceramic Society*, **6** [4] 205-25 (1990).

4. T. Dalibor, G. Pensi, N. Nordell, A. Schoner, W. J. Choyke, *Abstracts on International Conference on SiC, III-V Nitrides and Related Materials*, pg 55-6, Stockholm, Sweden, 1997.

5. R. G. Munro, "Material Properties of Titanium Diboride," *Journal of Research of the National Institute of Standards and Technology*, **150** [5] 709-20 (2000).

6. P. T. B. Shaffer, *Plenum Press Handbook of High Temperature Materials*, pg 107, Plenum Press, New York, 1964.

7. D. Ghosh, G. Subhash, T. S. Sudarshan, R. Radhakrishnan, "Dynamic Indentation Response of Fine-Grained Boron Carbide," *Journal of the American Ceramic Society*, **90** [6] 1850-7 (2007).

8. R. W. Rice, "Effects of Environment and Temperature on Ceramic Tensile Strength-Grain Size Relations," *Journal of Materials Science*, **32** [12] 3071-87 (1997).

9. D. H. Riu, R. Choi, H. E. Kim, E. S. Kang, "*Oxidation Behaviour and Strength of B_4C-30 wt% SiC Composite Materials*," *Journal of Materials Science* **30** [15] 3897-902 (1995).

10. S. Yamada, K. Hirao, Y. Yamauchi, S. Kanzaki, "High Strength B_4C-TiB_2 Composites Fabricated by Reaction Hot-Pressing," *Journal of the European Ceramic Society*, **23** [7] 1123-30 (2003).

169

11. S. Tuffe, J. Dubois, G. Fantozzi, G. Barbier, "Densification, Microstructure and Mechanical Properties of TiB_2-B_4C Based Composites," *International Journal of Refractory Metals and Hard Materials,* **14** [5] 305-10 (1996).

12. J. P. Schaffer, A. Saxena, T. H. Sanders, S. D. Antolovich, S. B. Warner, *Science and Design of Engineering Materials,* 2nd Edition, McGraw-Hill, New York, NY, 2000.

13. W. D. Kingerly, H. K. Bowen, D. R. Uhlmann, *Introduction to Ceramics,* 2nd Edition, John Wiley & Sons, New York, NY, 1976.

14. N. Rahaman, *Ceramic Processing and Sintering,* 2nd Edition, Marcel Dekker, New York, NY, 2003.

15. J. S. Reed, *Principles of Ceramics Processing,* 2nd Edition, John Wiley & Sons, New York, NY, 1995.

16. W. D. Callister, *Materials Science and Engineering: An Introduction,* John Wiley & Sons, New York, NY, 2007.

17. D. W. Richerson, *Modern Ceramic Engineering,* Marcel Dekker, New York, NY, 1992.

18. W. Barsoum, *Fundamentals of Ceramics,* Institute of Physics Publishing, London, England, 2003.

19. M. Bengisu, *Engineering Ceramics,* Springer-Verlag, Berlin, Germany, 2001.

20. C. Wood, D. Emin, P. E. Gray, "Thermal Conductivity of Boron Carbides," *Physical Review B,* **31** [10] 6811-4 (1985).

21. G. S. Upadhyaya, *Sintered Metallic and Ceramic Materials,* John Wiley and Sons, New York, New York, 1999.

22. Y. Ando, R. Uyeda, "Preparation of Ultrafine Particles of Refractory Metal Carbides by a Gas-Evaporation Method," *Journal of Crystal Growth,* **52** [1] 178-81 (1981).

23. D. R. Hamilton, "Interferometric Determination of Twist and Polytype in Silicon Carbide Whiskers," *Journal of Applied Physics,* **31** [1] 112-116 (1960).

24. R. F. Davis, "Proceedings of the International Conference in SiC and Related Materials," *Journal of Physics: Conference Series,* **137** [1] (1994).

25.   R. Kieffer, F. Benesovsky, E. R. Honak, "Über ein neues Verfahren zur Herstellung von Metallboriden der Übergangsmetalle, insbesondere von Titan- und Zirkonborid," *Zeitschrift für Anorganische und Allgemeine Chemie*, **268** [3] 191-200 (1952).

26.   C. Agte, K. Moers, "Methoden zur Reindarstellung hochschmelzender Carbide, Nitride und Boride und Beschreibung Einiger Ihrer Eigenschaften," *Zeitschrift für Anorganische und Allgemeine Chemie*, **198** [1] 233-75 (1931).

27.   B. Klotz, K. Cho, R. J. Dowding, R. D. Sisson, "*Characterization of Boron Carbide Consolidated by the Plasma Pressure Compaction (P^{2}C) Method in Air*," 25th Annual Conference on Composites, Advanced Ceramics, Materials, and Structures: B: Ceramic Engineering and Science Proceedings, **22** [4] (2001).

28.   S. H. Yoo, K. M. Sethuram, T. S. Sudarshan, *Method of Bonding a Particle Material to Near Theoretical Density*, U.S. Patent 6001304, 1999.

29.   N. Frage, L. Levin, M. P. Dariel, "The Effect of the Sintering Atmosphere on the Densification of B_4C Ceramics," *Journal of Solid State Chemistry*, **177** [2] 410-4 (2004).

30.   B. Champagne, R Angers, "Mechanical Properties of Hot-Pressed B-B_4C Materials," *Journal of the American Ceramic Society*, **62** [3-4] 149-53 (1979).

31.   M. Bouchacourt, F. Thevenot, "Analytical Investigations in the B-C System," *Journal of the Less-Common Materials*, **82** 219-26 (1981).

32.   W. F. Knippenberg, "Growth Phenomena in Silicon Carbide," *Philips Research Reports*, **18** [3] 161-274 (1963).

33.   J. A. Powell, P. Pirouz, W. J. Choyke, "Growth and Characterization of Silicon Carbide Polytypes for Electronic Applications," *Semiconductor Interfaces, Microstructures, and Devices: Properties and Applications*, pg. 257-93, Institute of Physics Publishing, Bristol, United Kingdom, 1993.

34.   A. R. Verma, P. Krishna, *Polymorphism and Polytypism in Crystals*, John Wiley and Sons, New York, NY, 1966.

35.   P. G. Neudeck, "SiC Technology," *The VLSl Handbook*, pg 6.1-6.24, CRC Press and IEEE Press, Boca Raton, Florida, 1998.

36.   R. G. Munro, "Material Properties of a Sintered α-SiC," *Journal of Physical and Chemical Reference Data*, **26** [5] 1195-1203 (1997).

37.   R. W. Olesinski, G. J. Abbaschian, "The C-Si (Carbon-Silicon) System," *Bulletin of Alloy Phase Diagrams*, **5** [5] 486-9 (1984).

38.   H. J. Seifert, F. Aldinger, "Phase Equilibria in the Si-B-C-N System," *Structure and Bonding: High Performance Non-Oxide Ceramics I*, pg 1-58, Springer, Berlin, Germany, 2002.

39.   R. G. Munro, "Material Properties of Titanium Diboride," *Journal of Research of the National Institute of Standards and Technology*, **150** [5] 709-20 (2000).

40.   W. Wang, Z. Fu, H. Wang, R. Yuan, "Influence of Hot-Pressing Sintering Temperature and Time on Microstructure and Mechanical Properties of TiB_2 Ceramics," *Journal of the European Ceramic Society*, **22** 1045-9 (2002).

41.   B. Lonnberg, "Thermal Expansion Studies on the Group IV-VII Transition Metal Diborides," *Journal of the Less-Common Materials*, **141** 145-56 (1988).

42.   B. Post, F. W. Glaser, "Borides of Some Transition Metals," *Journal of Chemical Physics*, **20** 1050-1 (1952).

43.   J. L. Murray, P. K. Liao, K. E. Spear, "The B-Ti (Boron-Titanium) System," *Bulletin of Alloy Phase Diagrams*, **7** [6] 550-5 (1986).

44.   M. Dietrich, T. Fett, *Ceramics: Mechanical Properties, Failure Behavior, Materials Selection*, Springer-Verlag, New York, NY, 1999.

45.   N. E. Dowling, *Mechanical Behavior of Materials*, 3rd Edition, Prentice Hall, Upper Saddle River, NJ, 2007.

46.   D. J. Green, *An Introduction to the Mechanical Properties of Ceramics*, Cambridge University Press, Cambridge, England, 1998.

47.   "Standard Test Method for Vickers Indentation Hardness of Advanced Ceramics," *ASTM Standard C 1327-03*, ASTM International, West Conshohocken, PA.

48.   J. M. Gere, *Mechanics of Materials*, 5th Edition, Brooks/Cole, Pacific Grove, CA, 2001.

49.   R. L. Norton, *Machine Design: An Integrated Approach*, 3rd Edition, Prentice Hall, Upper Saddle River, NJ, 2005.

50.   "Standard Test Methods for Determination of Fracture Toughness of Advanced Ceramics at Ambient Temperature," *ASTM Standard C 1421-01b (2007)*, ASTM International, West Conshohocken, PA.

51. "Standard Test Method for Flexural Strength of Advanced Ceramics at Ambient Temperature," *ASTM Standard C 1161-02c (2008)*, ASTM International, West Conshohocken, PA.

52. S. P. Dodd, G. A. Saunders, B. James, "Temperature and Pressure Dependences of the Elastic Properties of Ceramic Boron Carbide (B_4C)," *Journal of Materials Science,* **37** [13] 2731-6 (2002).

53. S. D. Conzone, W. R Blumenthal, J. R. Varner, "Fracture Toughness of TiB_2 and B_4C Using the Single-Edge Precracked Beam, Indentation Strength, Chevron Notched Beam, and Indentation Strength Methods," *Journal of the American Ceramic Society,* **78** [8] 2187-92 (1995).

54. T. L. Anderson, *Fracture Mechanics: Fundamentals and Applications,* 3rd Edition, CRC Press, Boca Raton, FL, 2005.

BIBLIOGRAPHY

1. A. Umberto, Z. Munir, Y. Kodera, T. Imai, M. Ohyanagi, "Influence of Synthesis of Synthesis Temperature on the Defect Structure of Boron Carbide: Experimental and Modeling Studies," *Journal of the American Ceramic Society,* **88** [6] 1382-7 (2005).

2. D. Ge, V. Domnich, T. Juliano, E. A. Stach, Y. Gogotsi, "Structural Damage in Boron Carbide Under Contact Loading," *Acta Materialia,* **52** [13] 3921-7 (2004).

3. D. Hull, *Fractography: Observing, Measuring and Interpreting Fracture Surface Topography,* Cambridge University Press, Cambridge, England, 1999.

4. D. Schiff, R. D'Agostino, *Practical Engineering Statistics,* John Wiley & Sons, New York, NY, 1995.

5. S. C. Chapra, R. P. Canale, *Numerical Methods for Engineers,* McGraw Hill, New York, NY, 2002.

6. X. Kuang, G. Carotenuto, L. Nicolais, "A Review of Ceramic Sintering and Suggestions on Reducing Sintering Temperatures," *Advanced Performance Materials,* **4** [3] 257-74 (1997).